

Università degli Studi di Napoli Federico II

Dipartimento di Ingegneria Chimica, dei Materiali e della Produzione
Industriale

CFD modelling and simulation of dense granular flow in a rotating drum

Angelica Maria Giovanna Arseni

Supervisors: Prof. P.L. Maffettone and Prof. F. Greco

This dissertation is submitted for the degree of

Doctor of Philosophy

06 May 2020

... a handful of poppy-seed moves easily just as a draught of water; for the several round particles are not checked one by the other, and when struck, it will roll downhill just like water.

Lucretius – De rerum natura

Abstract

Granular materials are ubiquitous in everyday life, in nature as well as in industry; therefore the prediction of granular fluid dynamics is of great interest in both physics and engineering research. A common complex granular flow is that occurring in rotating drums, which are widely employed as mixers, separators, dryers, reactors and granulators in different industrial processes.

Numerical simulations can provide a useful tool to understand the physics underlying the dynamics of these materials. In most of the works available in the literature, the commonly adopted numerical approach to study granular materials is the Discrete Element Method (DEM), where the material is modelled as an assembly of rigid particles, and the interactions among particles are explicitly considered. Although DEM has the advantage to describe the discrete nature of the flow, a relatively limited number of particles can be managed. This drawback becomes important for large-scale flow modelling, as for the case of an industrial drum, containing billions of particles; a continuum approach, where the solid phase is treated as a continuum, is possibly more suitable.

In this work, we present 3D Finite Volume (FV) simulations of dense granular flow of non-cohesive beads inside a rotating cylinder, adopting the visco-plastic Jop-Forterre-Pouliquen constitutive model [78, 79] for the granular medium stress tensor.

We investigated in our simulations different flow conditions, by changing the cylinder aspect ratio and the drum angular velocity. Moreover, the material parameters and the

particle dimensions, appearing in the constitutive equation, are systematically varied, to understand their effects on the main features of flow in the cylinder.

The results obtained from our simulations are also compared with several experimental results available in the literature for the mono-disperse and bi-disperse case. We reproduce the flow configurations sequence in rotating drums, ranging from rolling to centrifuging [111], in good agreement with experimental results [146]. We capture some distinctive features of granular flow in a rotating drum, such as a Bagnold profile [10] followed by an exponential tail for velocity throughout the depth of granular bed [87, 73], the existence of axial components of the surface velocity, and the difference of the flow field near the lateral wall and at the symmetry plane [129]. Moreover, we investigated the segregation patterns of bi-disperse mixture varying the filling degree of the rotating drum [113].

This validation opens up the feasibility of characterising a wide variety of regimes by changing both physical and geometric parameters, with the possibility of discovering new dynamical regimes, and of calculating several flow quantities difficult to be accessed through experiments.

Table of contents

List of figures	ix
List of tables	xii
Nomenclature	xiii
1 Introduction	1
1.1 Work motivation	3
2 Mono-disperse granular flow	7
2.1 Literature review	7
2.1.1 Experimental literature	7
2.1.2 Numerical literature	15
2.1.3 Towards a dense granular rheology	19
2.2 Governing equations	30
2.3 Numerical method	34
2.4 Results	37
3 Mixing of bi-disperse granular material	56
3.1 Literature review	56
3.1.1 Experimental literature	57
3.1.2 Numerical literature	64

Table of contents

3.2	Governing equations	70
3.3	Results	73
3.3.1	Mixing of particles of two different colour	73
3.3.2	2D Density segregation	76
3.3.3	3D Density segregation	79
4	Conclusions and future perspectives	84
	References	88

List of figures

1.1	Examples of granular materials	1
1.2	Classification of particulate matter depending on particle size	2
1.3	Solid, liquid and gas behaviours	4
2.1	Flow configurations in a rotating drum	8
2.2	Flowing layer and plug region	9
2.3	Experiments on velocity profile inside the granular bed	10
2.4	Rotating cylinder sketch	11
2.5	The stream-wise surface velocity as a function of the axial position	13
2.6	Magnitude of axial flow	14
2.7	Asymmetric/Symmetric stream-wise velocity	14
2.8	CFD Kinetic-theory-based results for flow velocity inside the granular bed	16
2.9	CFD Kinetic-theory-based results for drum flow configurations	17
2.10	Standard configurations of granular flows	20
2.11	Physical meaning of I	21
2.12	Friction coefficient and volume fraction as a function of the inertial number	23
2.13	Diagram of the granular flow regimes depending on I	24
2.14	Region of steady uniform flows on inclined planes	25
2.15	Minimum and maximum angles of continuous flow on inclined planes	25

2.16	Free-surface velocity and depth profiles on a heap for experiments and continuous simulations	28
2.17	Sketch of the problem geometry	33
2.18	Adopted mesh (“A”)	39
2.19	Predicted flow configurations: rolling, cascading and centrifuging	40
2.20	Predicted cataracting regime	42
2.21	Time series of surface angle by means simulations	45
2.22	Adopted mesh (“C”)	47
2.23	Predicted shape of free-surface and stream-wise velocity in the rolling regime	48
2.24	Simulated velocity profile inside the granular bed	50
2.25	Bagnold velocity profile in the flowing layer and exponential decay in the rigidly rotating part	51
2.26	Predicted and experimental stream-wise velocity profile along the axial direction varying the aspect ratio	53
2.27	Density plot of the axial velocity on the free surface and velocity vector map parametric in the aspect ratio	54
3.1	Dynamic of a greater bead intruder	58
3.2	Segregation patterns for particles differing only in size	58
3.3	Segregation patterns when buoyancy and percolation mechanisms act in the same direction	60
3.4	Segregation patterns when buoyancy and percolation oppose each other	60
3.5	Segregation patterns depending on drum speed	61
3.6	Segregation patterns for avalanching regime at different filling degrees for experiments and simulations	62
3.7	Dependence of the mixing efficiency on the filling degree	62

3.8 Axial segregation patterns of a ternary mixture differing in size over time for experiments	64
3.9 DEM mixing patterns at different time instants	67
3.10 DEM radial density segregation results	67
3.11 DEM radial segregation results for particles differing in size and density	67
3.12 Experimental and simulative results for different filling degree over time	69
3.13 Axial and radial segregation by Eulerian continuum approach	69
3.14 Initial configuration for mixing simulations	74
3.15 Comparison between our predictions and experiments [113] about segre- gation patterns	75
3.16 Segregation patterns after 6 revolutions for our simulations	75
3.17 Initial configuration for mixing simulations	77
3.18 2D CFD Density segregation for rolling regime	78
3.19 2D CFD Density segregation for cascading regime	79
3.20 3D CFD Density segregation for cascading regime	80
3.21 3D CFD Density segregation for cascading regime	81
3.22 3D Cores formation	82

List of tables

2.1	Parameters used in our simulations and experiments of comparison for the mono-disperse case	38
3.1	Parameters used in our simulations for the bi-disperse case	73

Nomenclature

Roman Symbols

Co Courant number

\mathbf{D} Rate of deformation tensor

d_p Particle diameter

f Filling degree

Fr Froude number $Fr = \frac{\Omega^2 R}{g}$

g Gravitational acceleration

h Flowing layer depth

\mathbf{I} Identity matrix

$II_{\mathbf{D}}$ Second invariant of \mathbf{D}

$II_{\boldsymbol{\tau}}$ Second invariant of $\boldsymbol{\tau}$

I Inertial number $I = \frac{II_{\mathbf{D}} d_p}{\sqrt{p/\rho_p}}$

I_0 Fitting parameter in $\mu(I)$ rheology, $I_0 = 0.3$

p Pressure

R	Cylinder radius
r	Radial coordinate
\mathbf{u}	Velocity vector
u	Velocity magnitude
$\nabla \mathbf{u}$	Velocity gradient

Greek Symbols

α	Volume fraction of granular phase in the monodisperse case
α_i	Volume fraction of granular phase “ i ”, $i \in \{1, 2\}$ in the bidisperse case
$\dot{\gamma}$	Shear rate
μ	Friction coefficient
μ_2	Limiting value of μ at high inertial number I
μ_s	Limiting value of μ at low inertial number I
Ω	Rotational velocity
ϕ	Packing factor of the grains
ρ	Density
ρ_{gp}	Granular phase density
ρ_p	Particle density
$\boldsymbol{\sigma}$	Total stress
$\boldsymbol{\tau}$	Shear stress

Acronyms / Abbreviations

AR	Aspect ratio
MPM	Material Point Method
SPH	Smoothed Particle Hydrodynamics
CFD	Computational Fluid Dynamics
DEM	Discrete Element Method
FEM	Finite Element Method
FVM	Finite Volume Method
JFP	Jop-Forterre-Pouliquen model
MCEP	Mohr–Coulomb Elasto-Plastic model
MRI	Magnetic Resonance Imaging
PEPT	Positron Emission Particle Tracking

Chapter 1

Introduction



Fig. 1.1 Examples of granular materials.

Granular materials are ubiquitous in our daily lives; flour, sugar, sand, cement are things without which the life would be very different (fig. 1.1). It has been estimated that more than 50% of sales in the world involve commodities produced using granular materials at some stage, which makes granular media the second most used type of

material in industry after water [5]. Major industries dealing with granular materials are food, pharmaceutical, petrochemical, polymer, and glass industries.

On the other hand, granular matter is very common in natural phenomena; soil is made of solid particles so, the knowledge of the physics underlying granular flow is very important to prevent the consequences of natural hazards, such as avalanches, landslides, sand dunes, pyroclastic flows. The behaviour of soil is becoming more and more interesting because of the solar system exploration; for example, knowing Mars soil mechanical properties is essential for the correct landing of a probe.

Despite this significant interest, a theoretical framework which describes the variety of complex behaviours of the granular materials is still missing and so, these materials still challenge engineers and fascinate researchers.

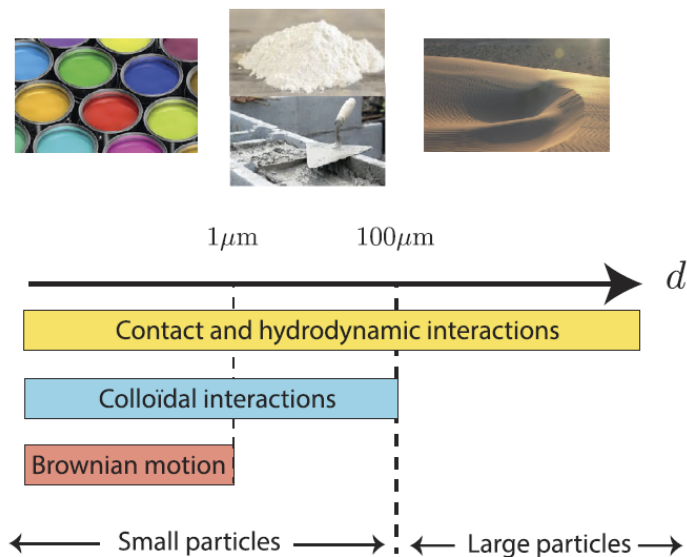


Fig. 1.2 Classification of particulate matter depending on particle size; colloids $d < 1\mu\text{m}$, powder $d < 100\mu\text{m}$ and granular material [5].

We shall consider granular material as a large conglomerate of macroscopic, discrete, rigid particles.

The behaviour of granular medium depends on the grain size (see fig. 1.2). When particles are larger than $100\mu\text{m}$, the dominant forces are due to direct mechanical

contacts involving normal compression and tangential frictional forces, and when the grains are immersed in a liquid, to hydrodynamics interactions induced by the motion of the interstitial fluid. For particles with $d < 100 \mu\text{m}$ (powder), humidity effects, air (or solvent) drag, and colloidal forces interfere, such as van der Waals and electrostatic interactions. If $d < 1 \mu\text{m}$, thermal agitation of the solvent becomes significant, and Brownian motion comes into play [55].

In this thesis we take into consideration dry particles with a diameter above $100 \mu\text{m}$.

1.1 Work motivation

Granular material can imitate different states of aggregation of the matter depending on the rate of deformation; at low velocity of deformation granular matter behaves like a solid, with very long frictional contacts between particles, increasing the velocity of deformation the grains flow like a liquid, at even greater rate the material acts like a gas with rapid binary contacts (see fig. 1.3). In the limit of low and high velocity of deformation granular behaviour is successfully described by solid-like soil mechanics and gas-like kinetic theory, respectively. Theory for the “liquid-regime” is at an early, though very promising, stage of development.

Due to the absence of a unified theory, problems for mixing, flow, transportation, and storage are often encountered, which are solved by engineers using empirical techniques.

The commonly adopted approach in most of the works available in the literature is based on the Discrete Element Method (DEM), where the material is modelled as an assembly of rigid particles, and interactions among particles are explicitly considered. DEM accounts for the discrete nature of the flowing material, but a relatively limited number of particles can be effectively managed [26]. To our knowledge, the largest system treated so far, in the discharge flow from a silo, is about 10^7 particles [128].

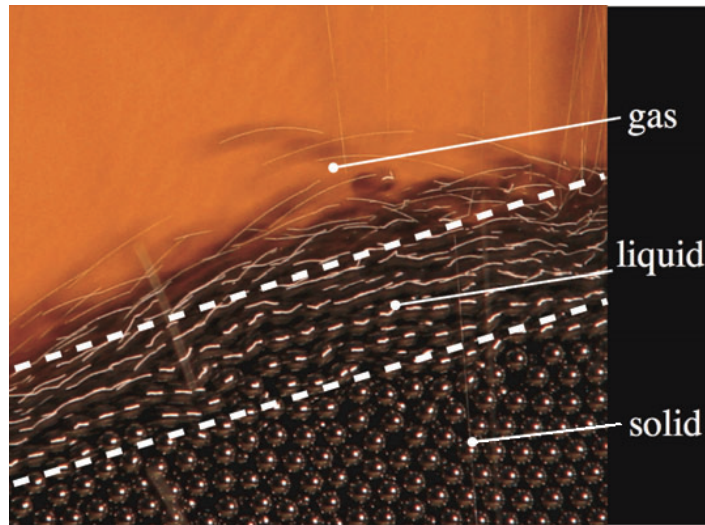


Fig. 1.3 Different behaviours of granular material depending on the velocity of deformation; solid, liquid and gas [54].

On the other hand, just to give an example, a small industrial cylindrical mixer, with a radius $R = 1.5$ m equal to length W , half-filled with $200\ \mu\text{m}$ spherical particles (typical sizes in practical applications as for pharmaceutical granulators) contains about 10^{12} particles, presently out of reach for DEM computations. Practical flow conditions may be even more extreme in full-scale rotating drums employed in industrial applications.

From a different perspective, a continuum approach, where the granular phase is treated as a continuum, should be suitable for large-scale flow modelling. Indeed, the description of liquid-like granular flows has been a long-standing challenge of process engineering as well as of geophysical science. Such continuum approach is very attractive, if applicable, as it could manage real scale systems, e.g., natural avalanches or large industrial devices.

A constitutive law reproducing the entire complexity of the granular flow behaviour in the liquid range is still elusive. Our aim here is to prove that a description of complex flows in large scale applications is in fact possible, with a suitable constitutive fully 3D equation for the rheology of the continuous granular phase.

Jop et al. [78, 79] proposed a constitutive equation for the granular liquid regime, capable of describing the two principal features of a granular liquid, i.e. a yield criterion and a complex dependence of the viscosity on rate of deformation and pressure. The Jop-Forterre-Pouliquen (JFP) model has already been tested on simple geometries and flow conditions, showing remarkable agreement with experiments [12, 52, 88, 153, 71].

In this thesis, we present 3D Finite Volume (FV) simulations of dense granular flow inside a rotating cylinder, adopting the continuum visco-plastic JFP constitutive model [79] for the granular medium.

A common complex granular flow of great interest in both physics and engineering research is that occurring in rotating drums, usually employed as mixers, separators, dryers, reactors, and granulators in different industrial processes. Despite the common use of these devices, granular behaviour therein is not completely understood, also in view of the complex dependence on several operating conditions. This is a fully 3D problem, with the additional complexity of the presence of an evolving free surface separating the (assumed) continuous solid phase from the gas phase.

We are going to present dense particulate flows of monodisperse beads in a rotating drum in a first section, then we will analyze the mixing dynamic of bidisperse particles in a second part. Each section of the thesis will be dealt with the analysis of literature review, material and methods, and results.

Chapter 2

Mono-disperse granular flow

2.1 Literature review

2.1.1 Experimental literature

“The rotating drum is particularly associated with the study of dense granular flows” [149].

Mellmann [111] identified various flow configurations of granular media in rotating drums, depending on cylinder filling degree f , wall friction and *Froude number* (Fr), which is the ratio of inertia to gravity $Fr = D\Omega^2/g$ (fig. 2.1). According to Mellmann’s classification there are three main regimes:

- *Slipping*; when angular velocity, wall friction and filling degree are very low, no granular flow occurs. Depending on whether $f <$ or > 0.1 , *sliding* or *surging* sub-regime takes places. In the first one the material is constantly sliding from the wall, the granular bed does not move for an inertial observer. In the latter there is a bulk motion, because wall friction suffices to “grip” the material, and to generate a periodic alternation between adherence and sliding from the wall.

2.1 Literature review

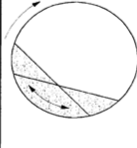
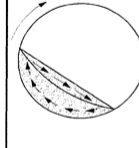
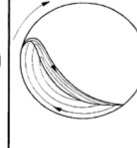
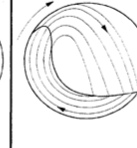
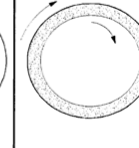
Basic form	Slipping motion		Cascading ("tumbling") motion			Cataracting motion	
Subtype	Sliding	Surging	Slumping	Rolling	Cascading	Cataracting	Centrifuging
Schematic							
Physical process	Slipping		Mixing			Crushing	Centrifuging
Froude number Fr [-]	$0 < Fr < 10^{-4}$		$10^{-5} < Fr < 10^{-3}$	$10^{-4} < Fr < 10^{-2}$	$10^{-3} < Fr < 10^{-1}$	$0.1 < Fr < 1$	$Fr \geq 1$
Filling degree f [-]	$f < 0.1$	$f > 0.1$	$f < 0.1$	$f > 0.1$		$f > 0.2$	
Wall friction coeff. μ_w [-]	$\mu_w < \mu_{w,c}$	$\mu_w \geq \mu_{w,c}$	$\mu_w > \mu_{w,c}$			$\mu_w > \mu_{w,c}$	
Application	no use		Rotary kilns and reactors; rotary dryers and coolers; mixing drums			Ball mills	no use

Fig. 2.1 Flow configurations in a rotating drum [111].

- *Cascading/Tumbling*; at intermediate values of Fr a “liquid-like” flow starts. Progressively increasing rotational speed, the *slumping* sub-motion can be observed, where cascades in the top of the bed periodically occur and decrease the free-surface angle from a maximum value to a minimum, afterward, the bed rigid rotation restores the higher angle, and the cycle repeats. Hence, in the slumping regime, the almost flat free surface periodically oscillates between two limiting angles.

Increasing further the velocity there are the *rolling* and the *cascading* sub-regimes, characterized by a continuous cascade. The only difference between rolling and cascading motions is the shape of free-surface, flat and S-shaped respectively. As we can read from the last row of the figure 2.1, this “liquid” regime is the most often encountered in applications, since it enhances mixing.

- *Cataracting*; if the gravitational acceleration becomes comparable to inertia, the particles are massively flung into the drum free space occupied by the gas and

the *cataracting* sub-regime occurs. At even greater Fr there is the *centrifuging*, where a uniform layer of grains covers the internal walls.

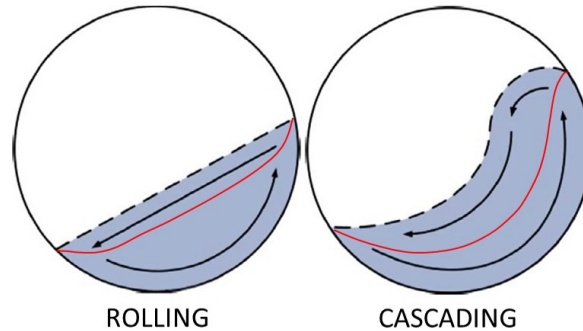


Fig. 2.2 *Flowing layer*, the “cascading zone” in the upper part of the bed, and the *plug region*, which follows the rigid rotation of the cylinder, divided by a red curve, in rolling and cascading regime, on left and right, respectively.

In rolling and cascading regimes can be distinguished a uniform particle layer called *flowing layer*, continuously flowing in the upper part of the bed, while the beads in the bulk essentially follow the rigid rotation of the cylinder, the so-called *plug region*, as it can be seen by fig. 2.2.

Most of the quantities available for granular flow in rotating cylinders are accessed by naked eyes. These experiments are conducted looking through transparent walls, but it is well known that there is a strong influence of the lateral wall on the flow [44, 106, 78, 129, 28, 127]; hence this is the worst condition for experiments. Since grains are opaque, the interior of the flow cannot be investigated with optical methods, but there are three other approaches: *Magnetic Resonance Imaging* (MRI) [168], *Positron Emission Particle Tracking* (PEPT) [124] and *X-ray imaging*. The first two allow the tracking of the single particle trajectory. Those are very complex experiments and their space and time resolutions are quite low. The disadvantages of these last techniques are the complexity, the lower space and time resolution with respect to the naked eye. *X-ray imaging* capture highly accurate trajectory fields, but the medical

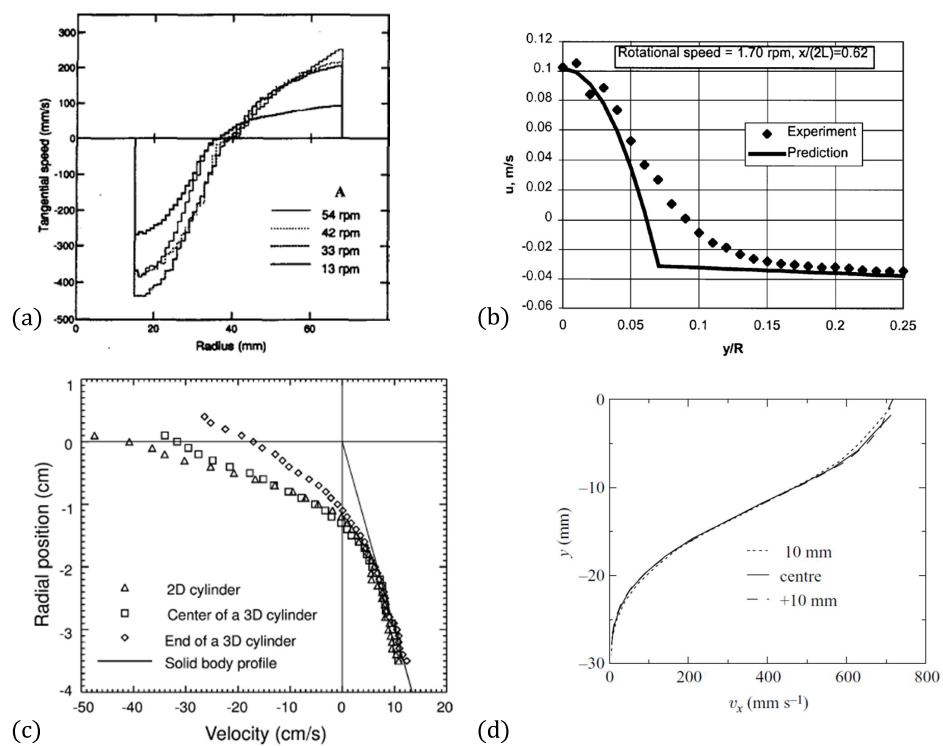


Fig. 2.3 Experiments on velocity profile inside the granular bed: Parker et al. [123] (a), Ding et al. [38] (b), Maneval et al. [106] (c), and Orpe and Khakhar [119].

protocols for continuous exposure narrow it down to very low density particles; thus data are insufficient for computing key rheological parameters like the volume fraction distribution [62].

Different authors studied the velocity profile inside the granular bed.

In fig. 2.4 there is a sketch of the rotating cylinder where the “end walls” and the “centre” can be distinguished.

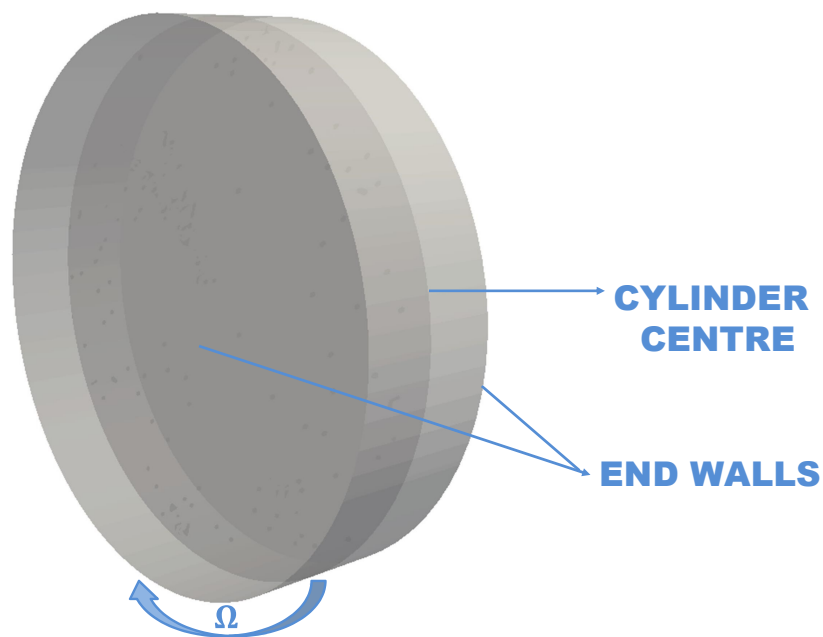


Fig. 2.4 Rotating cylinder sketch; the centre is the symmetry plane of the cylinder, the end walls are the two vertical cylinder walls.

Parker et al. [123] performed the first positron emission particle tracking of spherical particle motion in rotating drums and reported a non-linear velocity profiles in the flowing layer and the distributions of angular velocity in the fixed bed (fig. 2.3.a).

Ding et al. [38] investigated the velocity of glass beads in the rolling flow regime with a low filling degree, still with PEPT. The authors fit the velocity profile inside the bed with a second order polynomial (fig. 2.3.b).

Maneval et al. [106] and Sanfratello et al. [141] both found a velocity profile at cylinder centre and wall described by:

$$u(r) = \begin{cases} -u_{top} \left(1 - \frac{r}{h}\right)^2 + \Omega_{eff}r, & r < h \\ \Omega_{eff}r, & h < r < R \end{cases} \quad (2.1)$$

Where u_{top} is the maximum velocity at the top of the free surface, h is the depth of the flowing layer, and Ω_{eff} is the effective rotation rate determined from data. Ω_{eff} would be the rotation rate of the cylinder if there were no slippage.

Maneval et al. [106] reported a higher velocity at the centre with respect to that at the wall (fig. 2.3.c).

Unlike the authors that are just mentioned, Orpe and Khakhar [119] found a linear mean-velocity profile over most of the layer depth in all cases, with an exponential decay near the base of the flowing layer and a flattened region near the free surface, for a quasi-2D cylinder (fig. 2.3.d). This exponential tail is due to a solid-like regime that is characterised by dense quasi-static flow in which the deformations are very slow and the particles interact by frictional contact [140].

Yamane et al. [168] and Dury et al. [44] focused their attention on the differences between the dynamic angles at the centre and the wall by varying velocity. They both reported a dynamic angle 5° higher on the wall than at the centre of the cylinder independently from drum speed.

Félix et al. [48] reported a monotonically increasing scaling of the dynamic angle and the flow depth with the rotational velocity. The angle is also found to increase with decreasing width. It has to be noticed that the authors did not consider the width of the cylinder as an important parameter, so they simply reported its value, without controlling it thoroughly.

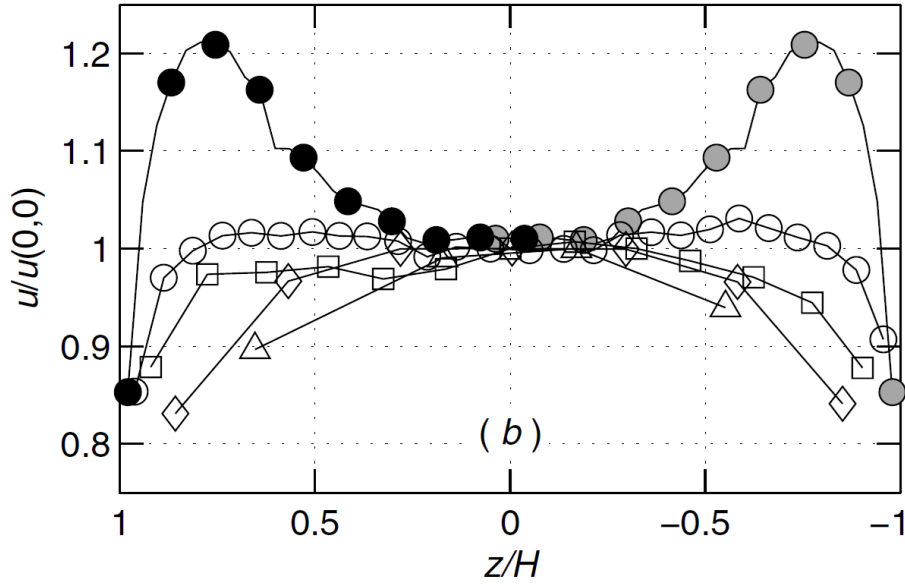


Fig. 2.5 The stream-wise surface velocity as a function of the axial position $\Delta L/D = 0.06$, $\diamond L/D = 0.14$, $\square L/D = 0.26$, $\circ L/D = 0.52$, $\bullet L/D = 1.03$, D and L are cylinder diameter and length respectively [129].

Pohlman et al. [129] investigated the free surface velocity of 3D cylinders changing the drum width. They reported the stream-wise surface velocity as a function of the axial position. They observed a velocity close to the wall 20% higher than that at the centre when $W/D > 1$, even though the particles on the wall were slower due to friction (fig. 2.5). The same authors presented contour and density maps of the axial flow. The free-surface velocity is directed toward the centre in the upper part of the free surface and toward the end walls in its lower part, in fact the magnitude of the axial velocity is bigger in the cylinder corners (fig. 2.6).

Alexander et al. [2] studied the stream-wise velocity profile in a rotating drum. They found a dependence on the rotational speed and on the ratio of particle size and cylinder diameter. The effect of rotational velocity on symmetry/asymmetry of the stream-wise velocity profile is shown in fig. 2.7. The same authors reported new non-dimensional scaling criteria using a simplified model in agreement with both the magnitude and the shape of the velocity profiles.

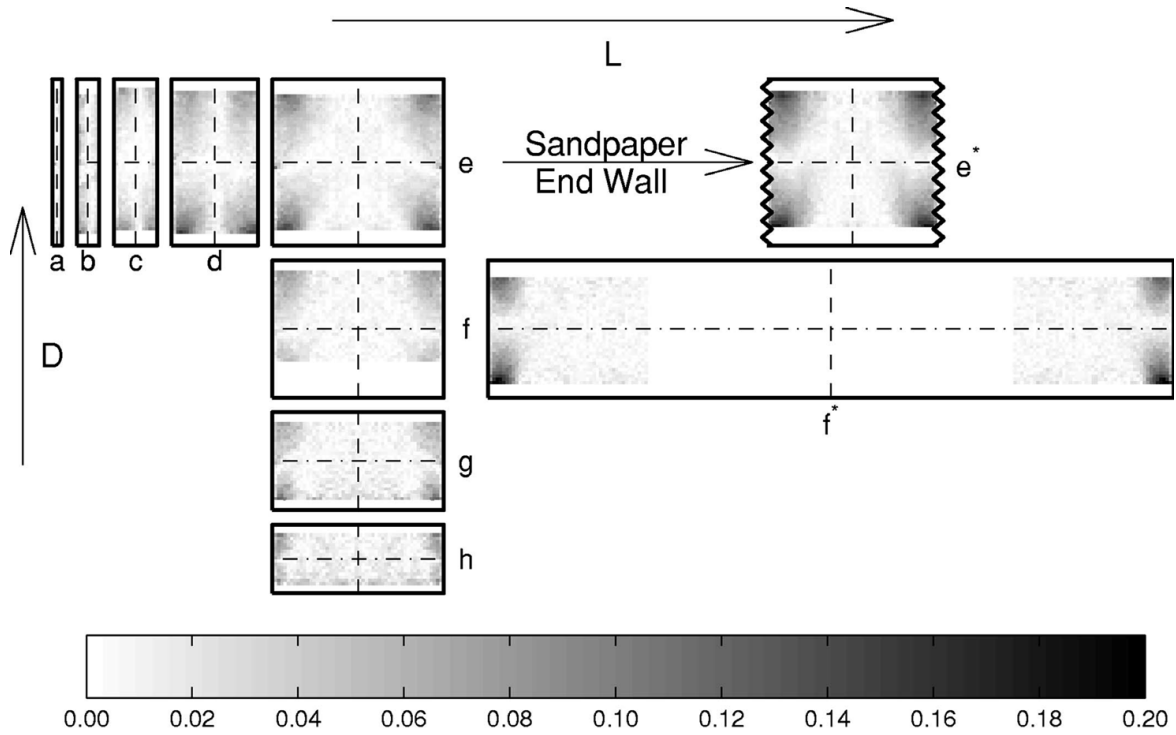


Fig. 2.6 Ratio of the magnitude of axial flow with respect to the stream-wise flow for 1 mm particles, D and L are cylinder diameter and length respectively [129].

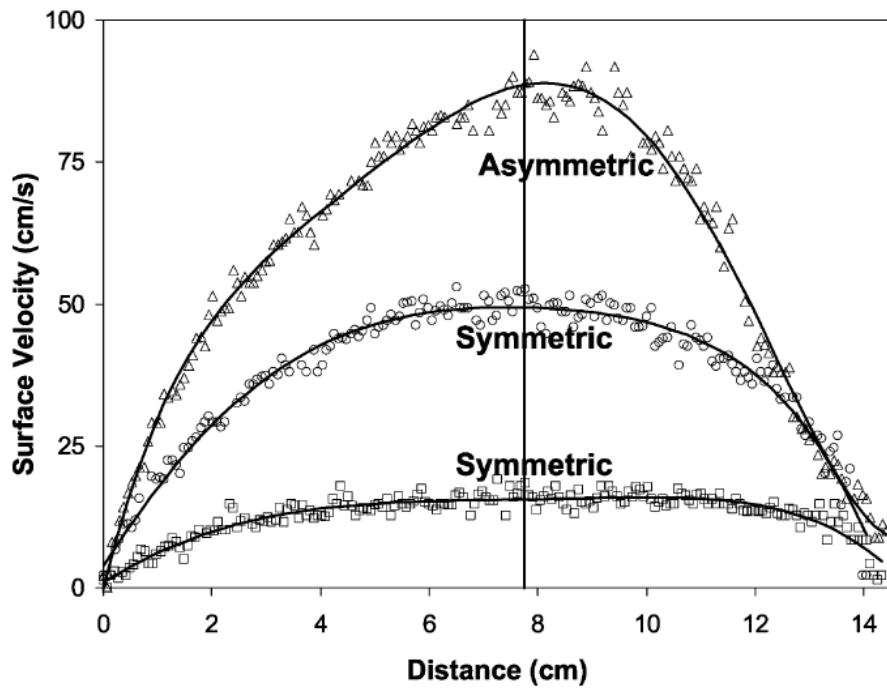


Fig. 2.7 Stream-wise velocity; asymmetric \triangle 52.1RPM, symmetric \circ 26.1RPM, and symmetric with a constant velocity region \square 4.3RRM, by Alexander et al. [2].

2.1.2 Numerical literature

CFD simulations

As mentioned above, a continuum approach, where the granular phase is treated as a continuum, should be suitable for large-scale flow modelling in order to manage real scale systems.

Attempts have been done to describe granular flow are focused on extending the existing theory for diluted assembly of collisional sphere, the so called kinetic theory Goldhirsch [61], to dense frictional spheres Haff [64], Campbell [24], Jenkins and Berzi [74], Berzi [18].

Some authors solved the Eulerian-Eulerian formulation of the balance equations coupled with the kinetic theory for dense granular materials inside rotating drums [65, 92, 162, 89, 35, 146, 170, 34, 84, 39, 105, 16, 70].

Demagh et al. [35] modelled the dense particulate flow with the kinetic theory of granular flow and with an Eulerian formulation, reproducing rolling and cascading regimes and finding qualitative agreement with the experimental data of Ding et al. [38].

The complete analysis by Santos et al. [146] compares experimental data with numerical predictions of the Eulerian-Eulerian approach, assuming interpenetrating continua and the kinetic-theory-based constitutive equations derived by Lun [103]. Their results are obtained at various drum rotation rates, and their predictions are in general qualitative agreement with their own experiments (fig. 2.19). The major drawback of this approach is the dependence of results on the choice of adjustable parameters. As we can see from the figure, where S1, S2, S3, S4, S5, and S6 are simulations which differ for critical volume fraction, a parameter of the kinetic model adopted by Santos et al. [146], there is a strong influence of the choice of this critical value of predictions.

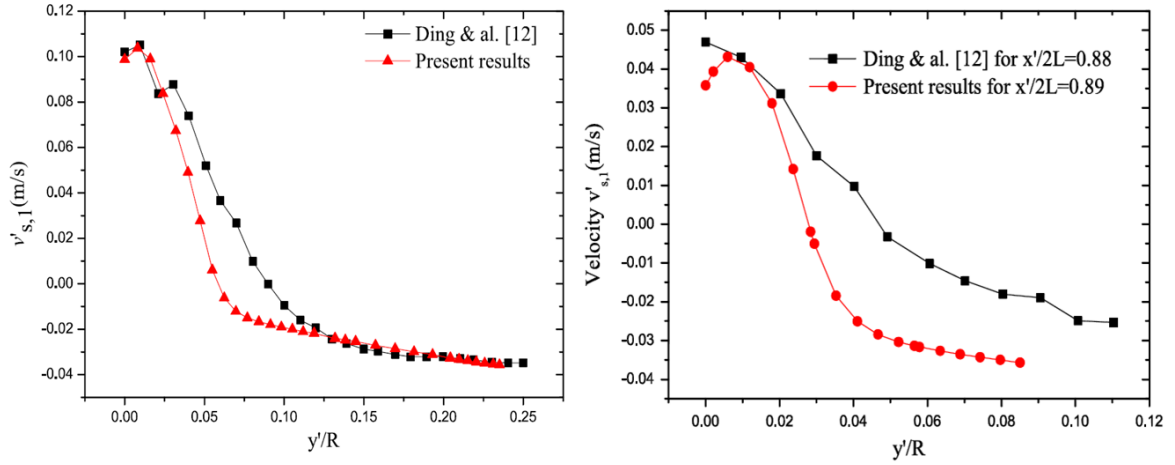


Fig. 2.8 Comparative plots of velocity inside the granular bed against dimensionless depth at two different free-surface positions for simulations [35] and experiments by Ding et al. [38].

Delele et al. [34] performed a multiphase 3D CFD model of particle and fluid flow in rotary drums with kinetic-theory-based constitutive equations by Lun [103] like Santos et al. [146]. The same authors conducted experiments for model validation. There are good agreements between numerical and experimental results on particle velocity, dynamic repose angle, active layer thickness, air velocity, and residence time measurements.

Machado et al. [105] compared their experimental and numerical results of the particle dynamic flow in a rotary drum with one flight, under different boundary conditions. They used the Euler-Euler approach with the kinetic theory of granular flow and a finite volume discretization method for simulations.

Zheng and Yu [170] presented a numerical study on the flow behaviours of granular materials in a rotating drum based on the Eulerian-formulation FEM. The granular material is treated as a continuum medium described by the *Mohr-Coulomb Elasto-Plastic* (MCEP) model. They reported qualitatively results on particle flow patterns ranging to rolling to centrifuging, obtained changing the drum speed in the simulations. The authors tried to reproduce slipping and slumping regime too, but they stated that

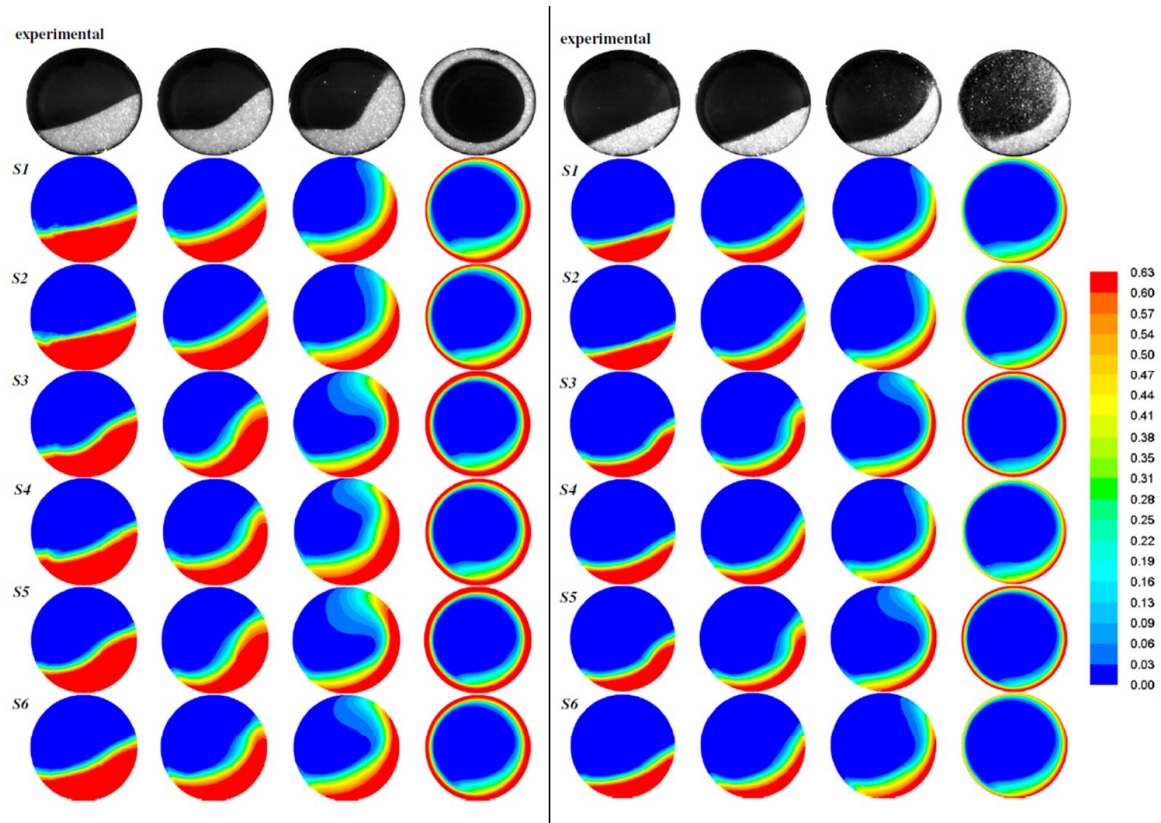


Fig. 2.9 Volume fraction of the granular solid phase for 1.09 mm glass beads. In the first row there are Santos et al. [146] experiments, S1, S2, S3, S4, S5, and S6 are simulations which differ for critical volume fraction, a parameter of the kinetic model adopted by Santos et al. [146]. Fill level of 31.40% on left and of 18.81% on right. Rotational velocities for each fill level of 1.45, 4.08, 8.91 and 16.4 rad/s.

“no evidence of slipping and slumping modes were observed in the simulations with the baseline parameters, no matter what rotational speed was used”.

Other models and numerical techniques

Kamrin [80] reformulated and combined models for granular elasticity [76] and rate-sensitive fluid-like flow [78] into one universal elasto-plastic law, capable of predicting flowing regions and stagnant zones simultaneously in any arbitrary 3D flow geometry. The model is numerically implemented in multiple geometries and results are compared to experiments and discrete simulations.

Eslamian and Khayat [46] proposed a hybrid method to simulate the dry granular flow of materials over a wide range of inertial numbers that simultaneously covers the quasi-static and dense granular flow regimes. The elastic–perfectly plastic theory based on the Drucker–Prager yield criterion is combined with the theory of dense granular flows, Smoothed Particle Hydrodynamics (SPH) [102, 59] is used as the framework for the method. The method is used to solve the 2D dry granular cliff collapse problem and to model dry granular material flow inside a rotary drum.

2D Smoothed Particle Hydrodynamic codes with the implementation of JFP model [78] were able to quantitatively match the experimental data available for the granular column collapse problem [27, 114].

Volpato et al. [161] studied flow occurring in partially filled 2D tumbler mixers of different shapes. The granular and the air flows was simulated using an Eulerian continuum approach. They proposed a suitable rheology for the granular flow. The model is based on conservation equations for mass, momentum and fluctuating kinetic energy and the rheology is described through a generalized Newtonian model whose viscosity depends on granular temperature. This approach was already used by Artoni et al. [8, 9] and Volpato et al. [160] for silos discharge.

In conclusion, it should be mentioned the Material Point Method (MPM), it was firstly developed to simulate problems of solid mechanics such as impact/contact, penetration, and perforation with history-dependent internal state variables [154, 155] and later applied to granular flows [13, 32]. MPM is a hybrid method with Eulerian–Lagrangian description. This feature allows the analysis of contact and force reaction between a soft (particle-based) body and a rigid (grid-based) surface. In literature there are different works on simulation of landslides behaviour by means of MPM [107, 41, 99, 77, 49, 47, 95, 96, 150, 97, 93, 15, 165, 94].

In particular Dunatunga and Kamrin [41] proposed a constitutive framework for the different behaviours of granular media: when dense, the material is treated as a pressure-sensitive elasto-viscoplastic solid obeying a yield criterion and a plastic flow rule given by the $\mu(I)$ -rheology; when the free volume exceeds a critical level, the material is deemed to separate and is treated as disconnected, stress-free media. By using the MPM they simulated silo flows, granular-column-collapses, and inclined chute flows.

Li et al. [91] used MPM simulations to study sloshing granular liquids.

Coetzee [31] and Chen et al. [29] investigated the soil cutting process using Material Point Method.

2.1.3 Towards a dense granular rheology

Dense granular matter can be seen as a visco-plastic material like toothpaste and ketchup. In fact, granular materials are characterized by:

1. flow threshold
2. shear-rate dependence
3. hysteretic behaviour

And there goes the question of whether a constitutive equation can describe granular liquids under stress.

Forterre and Pouliquen [54], Andreotti et al. [5], Goddard [60] and Forterre and Pouliquen [55] presented complete reviews of salient phenomenological aspects of granular flow, along with a unified mathematical synthesis of current continuum models.

Velocity, density and velocity-fluctuation profiles of the most common flow configurations, used to investigate dense granular flows, are studied in detail by the GDR MiDi [57]. These configurations can be distinguished in flows confined between walls (shear cells and silos) and free surface flows (inclined planes, heap flows and rotating drums), see fig. 2.10.

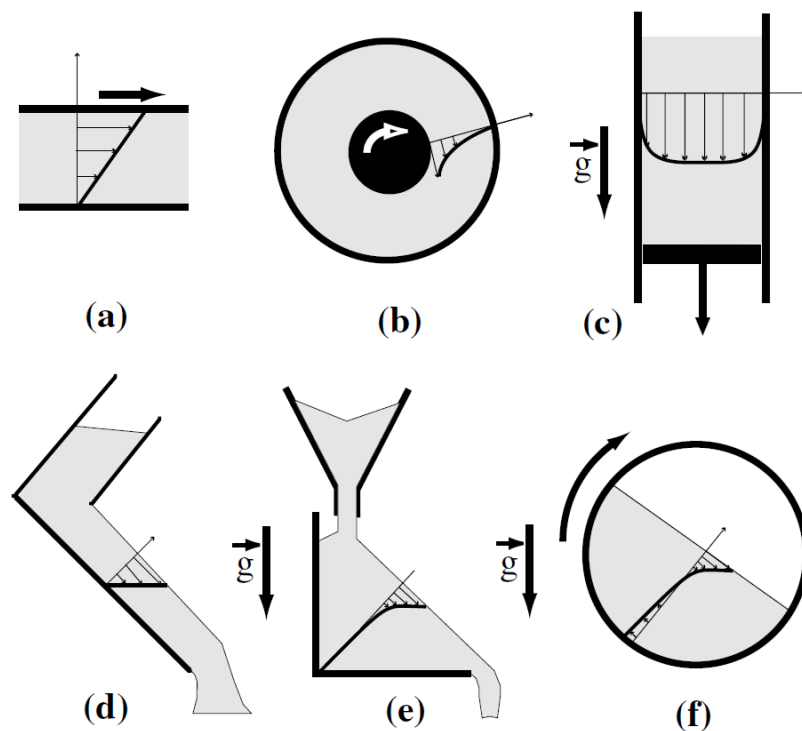


Fig. 2.10 The six configurations of granular flows: (a) plane shear, (b) annular shear, (c) vertical-chute flow, (d) inclined plane, (e) heap flow, (f) rotating drum [57].

GDR MiDi [57], da Cruz et al. [33] and Lois et al. [100] observed that, in a simple sheared configuration with rigid particles, the dimensional analysis strongly constrains

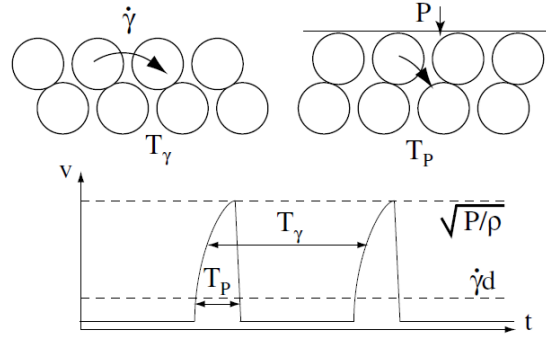


Fig. 2.11 Schematic showing the physical meaning of the typical time of deformation T_γ and the confinement timescale T_p [57].

the stress/shear rate relations. For large systems (i.e., when the walls do not come into play), the system is controlled by a single dimensionless parameter called the *inertial number*:

$$I = \frac{\dot{\gamma} d_p}{\sqrt{p/\rho_p}} \quad (2.2)$$

This parameter may be seen as the ratio of a microscopic time scale $d_p/\sqrt{p/\rho_p}$ which represents the time it takes for a particle to fall in a hole of size equal to the size particle d_p , under the pressure p and which gives the typical time scale of rearrangements, and a macroscopic time scale $1/\dot{\gamma}$ linked to the mean deformation, where $\dot{\gamma}$ is the shear rate (fig. 2.11).

For small values of I the system is quasi-static, i.e. the macroscopic deformation is lower than microscopic rearrangement, for large I the flow is rapid.

From the dimensional analysis, to switch from quasi-static to inertial regime, shear rate/pressure must increase/decrease. The shear stress is proportional to the pressure and the volume fraction is function of I :

$$\tau = \mu(I)p \quad (2.3) \quad \phi = \phi(I) \quad (2.4)$$

In the dense flow regime the volume fraction is almost constant. The dilatancy and friction laws are decoupled, which allows one to neglect the variations of $\phi(I)$ without losing the variations of the friction coefficient, which characterize the viscous nature of the material [79, 54].

Figure 2.12 .a and .b show da Cruz et al. [33] and Renouf et al. [137] $\mu(I)$ and $\phi(I)$ functions. da Cruz et al. [33] obtained this dependence by means 2D discrete numerical simulations of plane-shear at constant pressure, while Renouf et al. [137] performed 2D rotating drum simulations obtaining local friction coefficient and local I from the velocity profiles at different drum speeds. The friction coefficient μ is non-zero for $I = 0$, first increases and then saturate with increasing inertial number, and eventually decreases when reaching the kinetic gas regime. The volume fraction $\phi(I)$ decreases linearly with I .

In fig. 2.12 .b and .c $\mu(I)$ is obtained by Pouliquen [132] and GDR MiDi [57] from inclined-plane experiments measuring depth-averaged velocities at different inclinations and thickness.

Moreover, da Cruz et al. [33] determined the I interval for which the system is in the dense liquid state: $10^{-3} < I < 10^{-1}$ (see fig. 2.13).

Eq. 2.3 is obtained for plane shear configuration and, strictly speaking, using this relation for granular flow is not possible in general. But, if we can talk of local rheology, i.e. the shear stress depends only on the local shear rate and pressure, the stress is the same of plane shear.

In fig. 2.12 the curves, obtained in different flow configurations, collapse, suggesting that the inertial number I is the relevant parameter, in other words, the friction law $\mu(I)$ is independent from configuration and that granular liquids can be described in terms of local friction and dilatancy laws.

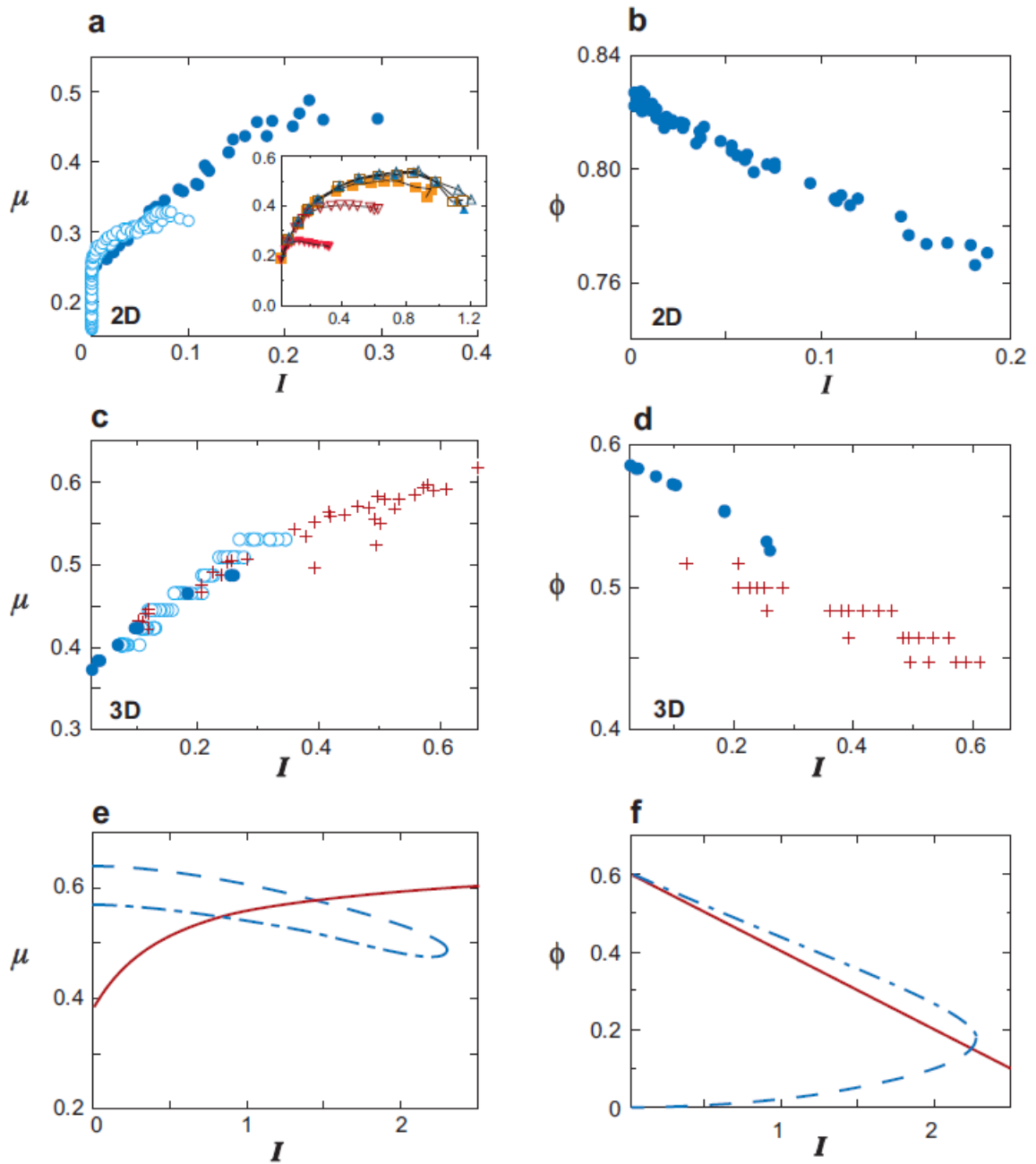


Fig. 2.12 Friction coefficient and volume fraction as a function of the inertial number [54].

(a, b): ●, 2D DEM plane-shear simulations by da Cruz et al. [33]; ○, 2D rotating drum simulations by Renouf et al. [137]. Inset in (a): Plane-shear simulation at constant volume fraction [100].

(c, d): ●, inclined-plane simulations of Baran et al. [12]; ○, inclined-plane experiments by Pouliquen [132] and GDR MiDi [57]; +, plane-shear experiments [147].

(e, f) Continuous line is the $\mu(I)$ relation 2.5, and dashed line is the prediction of kinetic theory for frictionless spheres [103].

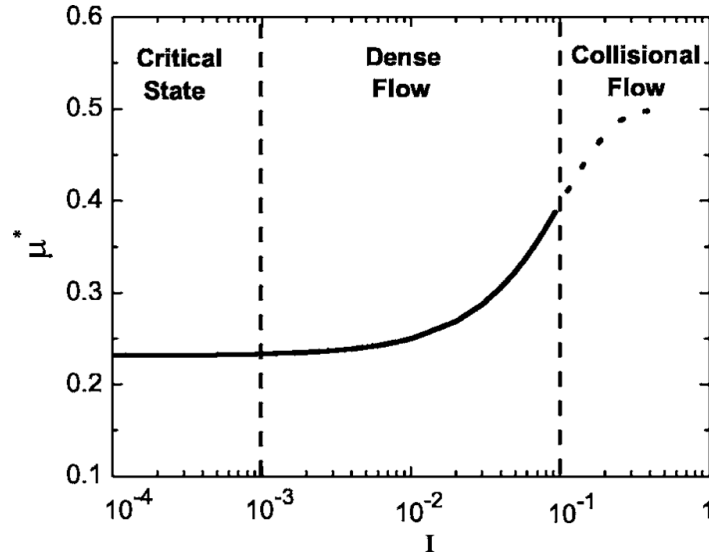


Fig. 2.13 Diagram of the granular flow regimes depending on I , for $10^{-3} < I < 10^{-1}$ the state is liquid.

Jop et al. [78] fitted $\mu(I)$ and $\phi(I)$ with the functions:

$$\mu = \mu_s + \frac{\mu_2 - \mu_s}{1 + I_0/I} \quad (2.5)$$

$$\phi(I) = \phi_{max} + (\phi_{min} - \phi_{max})I \quad (2.6)$$

In equation (2.5) μ_s , μ_2 and I_0 depend on the specific material and can be measured in simple flow configurations, I_0 is a fitting parameter, μ_s/μ_2 is linked to the minimum/maximum angle under/beyond which no continuous flow occurs fig. 2.14 (see Pouliquen [132] and Forterre and Pouliquen [53] for the detailed computation of these parameters). Pouliquen [132] reported minimum and maximum angles for some glass beads, see fig. 2.15. Equations (2.3) and (2.5) define the so-called $\mu(I)$ -rheology for granular liquids. Jop et al. [78, 79] used values for monodispersed glass beads in three dimensions: $\mu_s = \tan(21^\circ)$, $\mu_2 = \tan(33^\circ)$, $I_0 = 0.3$, see fig. 2.15.

The friction law saturates to a finite value μ_2 when I goes to infinity. Although the friction law has not been directly tested for large values of the inertial number

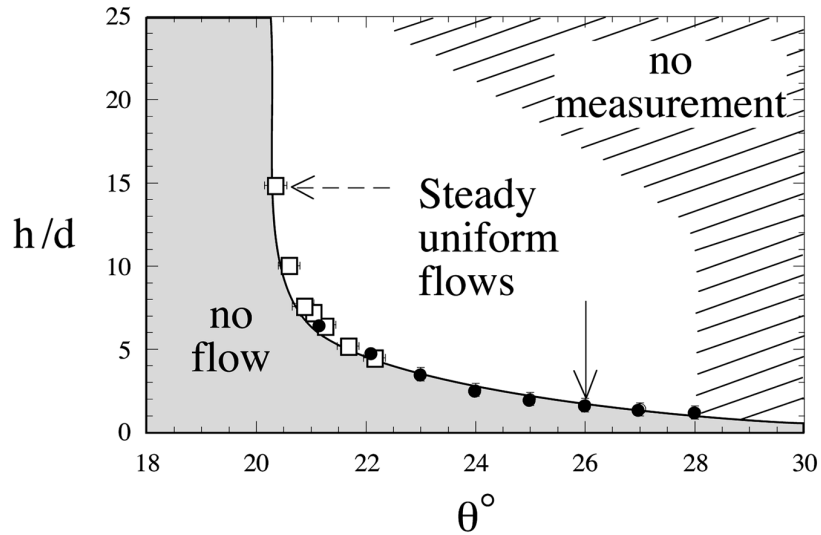


Fig. 2.14 Region where steady uniform flows are obtained; h is the granular thickness on inclined plane, d is the particle diameter and θ is the slope [132].

TABLE I. Glass beads used for the bulk material and for the rough surface for the different systems studied; corresponding parameters of fit 3.

	Bulk	Rough surface	θ_1	θ_2	L
System 1	$0.5\text{mm} \pm 0.04$	$0.5\text{mm} \pm 0.04$	20.7°	32.8°	1.96
System 2	$1.3\text{mm} \pm 0.13$	$1.3\text{mm} \pm 0.13$	21.7°	26.4°	1.23
System 3	$1.15\text{mm} \pm 0.1$	$1.3\text{mm} \pm 0.13$	22.9°	30.4°	1.50
System 4	$0.5\text{mm} \pm 0.04$	$1.3\text{mm} \pm 0.13$	20.9°	29.1°	2.9

Fig. 2.15 Minimum and maximum angles of continuous flow on inclined plane by Pouliquen [132].

I , we will see that this saturation is supported by experiments on steady granular fronts flowing down a slope, in fact at the tip of a front the shear rate goes to infinity, whereas experiments reveal that the slope (and hence the friction coefficient) is finite, so the saturation of μ to a finite value could be true [54].

This $\mu(I)$ relation has been successful in predicting two-dimensional configurations, capturing velocity profiles on inclined planes [57, 152] and important features of flows on a heap [78], without any fitting parameter once the friction law is determined independently in inclined-plane experiments.

Rotating drum flows have similarities with inclined plane flows; in fact the flow is restricted to an upper zone of the granular bed close to the free-surface; however, data are difficult to analyse, owing to the non-uniformity of the flow [137].

Renouf et al. [137] have shown in 2D simulations that the friction law $\mu(I)$ is locally satisfied along the profile.

Orpe and Khakhar [119] also reported that the variation of the friction coefficient is correctly described in their experiments.

A tensorial generalization of eq. (2.5) is needed to account this non-uniformity; Jop et al. [79] generalize the $\mu(I)$ relation assuming the constancy of the volume fraction, and hence an incompressible granular liquid phase, as follows:

$$\boldsymbol{\sigma} = -\mathbf{I}p + \boldsymbol{\tau} \tag{2.7}$$

$$\boldsymbol{\tau} = 2\eta(II_{\mathbf{D}}, p)\mathbf{D} \tag{2.8}$$

$$\eta = \mu(I)\frac{p}{II_{\mathbf{D}}} \tag{2.9}$$

where \mathbf{I} is the identity matrix, \mathbf{D} is the rate of deformation tensor (i.e. the symmetric part of the velocity gradient $\nabla\mathbf{u}$), $II_{\mathbf{D}}$ is the second invariant of \mathbf{D} (from now on called the shear rate), p is an isotropic pressure, and η the viscosity of the granular phase.

The viscosity diverges to infinity when the shear rate goes to zero. This divergence ensures that a yield criterion exists. If the shear rate goes to zero, the material flows only if the following condition is satisfied [79]:

$$II_{\tau} > \mu_s p \quad (2.10)$$

where II_{τ} is the second invariant of τ .

This is a Drucker–Prager-like criterion [40]. Under the threshold, the granular material acts like a solid, a rigid body. This property is linked to the frictional nature of stresses in granular media, which induces a flow threshold proportional to the normal stress (the Mohr–Coulomb criterion).

To test this rheology Jop et al. [79] performed experiments of granular flows on a pile. They made rough sidewalls by gluing beads on them, reproducing a no-slip boundary condition at the walls.

This tensorial rheology has been tested for free surface flows between rough walls [79], in which shear in two directions is present, and for the long wave instability of flows on inclined planes [52]. In both cases, striking quantitative agreement was obtained between predictions and experimental measurements for velocity profiles and dispersion relations.

Lagrée et al. [88] implemented the so-called $\mu(I)$ rheology in a 2D fluid-mechanics solver, simulated granular column collapses for a wide range of initial aspect ratios and compared the CFD results with both analytical solutions and 2D contact dynamics discrete simulations. Their predictions implementing the JFP model agree very well with DEM results.

Ionescu et al. [71] reformulated the JFP model in the framework of Drucker–Prager plasticity with the yield stress and viscosity depend on both the pressure and the norm of the strain rate tensor. The authors simulated with finite element method the

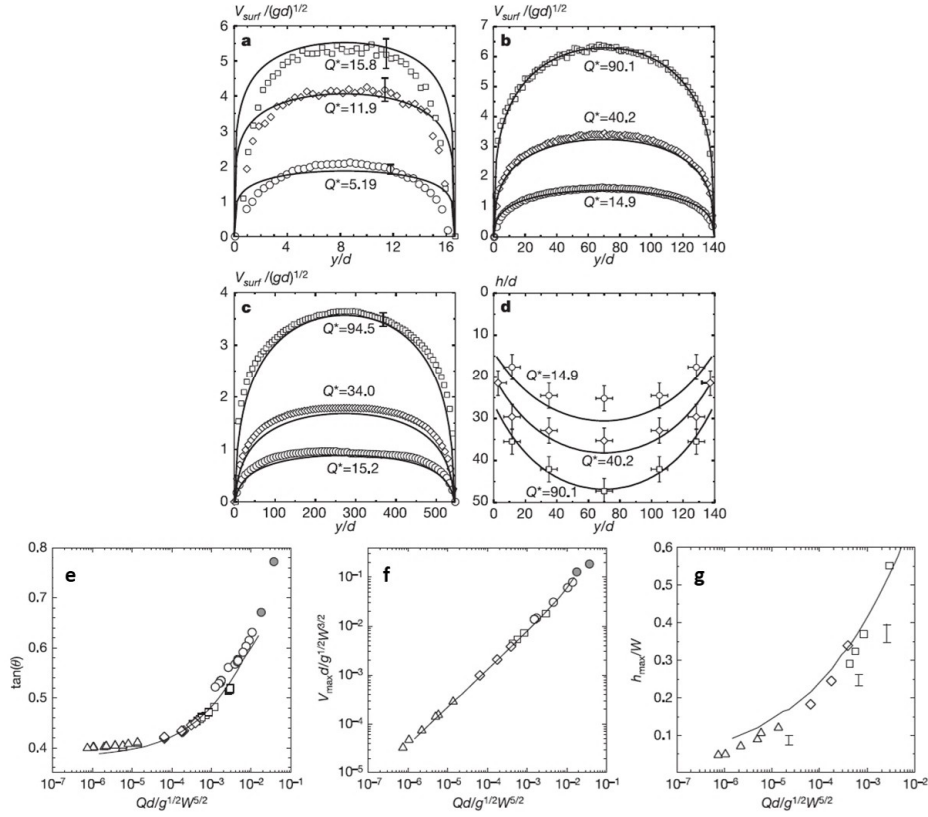


Fig. 2.16 Comparison of 3D simulations (lines) and experimental results (symbols) by Jop et al. [79].

(a, b, c); free-surface velocity profiles for different channel widths and for different flow rates.

(d); depths of the flowing layer across the channel for different flow rates.

(e, f, g); free-surface inclination, rescaled maximum free-surface velocity and maximum flowing thickness respectively, as a function of the rescaled flow rate.

granular column collapse over inclined planes, the rheological parameters are directly derived from the experiments. The computed run-out distances and slopes of the piles agree very well with experiments. They observed a slumping behaviour due to the flow/no-flow criterion and to the associated strain-independent part of the constitutive model, related to plastic effects. The same authors reported that the velocity profiles have a velocity maximum at the free surface, a Bagnold-like to linear profile and an exponential tail near the transition between the flowing layer and the crepey zone. Furthermore, the development of shear bands during the beginning of the spreading on an inclined plane was observed.

Local rheology limits

The local rheology seems to provide a theoretical framework to describe dense granular flows. Although, the link with microscopic grains properties is still lacking, and serious limitations exist [54]. Some phenomena observed are not described by the local rheology; the creeping exponential tail, at the transition zone between the flowing liquid layer and the solid granular bed, and the flow threshold are not exactly captured. Below a threshold the continuous flow stops and intermittent flow with successive transient avalanches starts [90, 78]. Indeed, the local rheology predicts a continuous steady flow even for very low angles of pile inclination [54]. Moreover, when the flow rate is very high and dilute region develops on top of the dense flow, high slopes up to 60° are reported [159, 101], while Jop et al. [78] predicted an inclination always below $\tan^{-1}(\mu_2)$. Pouliquen et al. [133] reported the non-uniformity of the stress distribution, i.e. the shear bands, but the predicted thickness of shear bands depends on the shear rate and vanishes in the quasi-static regime, unlike experimental observations. Another limit is that it does not take into account the hysteresis observed in some flow configurations [57].

Non local extension of the JFP model has been recently proposed to overcome some of these limits [134, 21, 156, 83, 22, 66, 67, 82, 68, 169].

[81] discussed a range of models (also models different from the JFP) that have been proposed to take into account non-local effects of granular flow.

2.2 Governing equations

Our aim is to capture some experimental results available in the literature for several flow conditions, which differ in terms of cylinder angular velocity Ω , filling degree f , particle diameter d_p , particle density ρ_p , cylinder diameter D , and cylinder length W . The first goal is to reproduce the entire succession of flow regimes identified by Mellmann, i.e. rolling, cascading, cataracting and centrifuging, and compare our simulations with experiments [146, 11]. The second is to predict quantitatively features of granular flow, as shape of free-surface, superficial velocity, velocity inside the bed, and axial velocity, like in experimental literature [38, 129].

In this first part of the thesis we solve numerically granular flow of monodisperse, cohesionless and dry grains inside a rotating cylinder. The remaining space, not occupied by the grains, is filled by air.

Equations for the mass balance and the momentum balance with the adoption of the JFP constitutive equation are solved with the Volume of Fluid (VoF) approach (for details about the method see Moukalled et al. [115]). The VoF approach treats the mixture of two phases as a single whole fluid with physical properties calculated as volume-weighted averages between properties of the “pure” phases. An independent variable, a phase volume fraction α , is then added to the model, representing the fraction occupied by one of the phases (the granular phase in our case), in each control volume:

$$\frac{\partial \rho}{\partial t} + \nabla \cdot (\rho \mathbf{u}) = 0 \quad (2.11)$$

$$\frac{\partial \rho \mathbf{u}}{\partial t} + \nabla \cdot (\rho \mathbf{u} \mathbf{u}) = -\nabla p + \nabla \cdot \boldsymbol{\tau} + \rho \mathbf{g} \quad (2.12)$$

where ρ , p , \mathbf{u} , and $\boldsymbol{\tau}$ are the density, pressure, velocity, and the shear stress of the single whole fluid, \mathbf{g} is the gravity, and t is the time.

The additional independent variable α requires a transport equation and the VoF approach uses a simple advection equation:

$$\frac{\partial \alpha}{\partial t} + \nabla \cdot (\alpha \mathbf{u}) = 0 \quad (2.13)$$

where α is the volume fraction of granular phase. The volume fraction ranges from 0 (air only) to 1 (granular phase only). The interface between the two phases is postulated to be at $\alpha = 0.5$.

The density and the viscosity of the overall fluid are treated as simple linear (with respect to α) averages of densities and viscosities of granular phase and air:

$$\rho = \alpha \rho_{gp} + (1 - \alpha) \rho_{air}, \quad \eta = \alpha \eta_{gp}(II_{\mathcal{D}}, p) + (1 - \alpha) \eta_{air} \quad (2.14.a, .b)$$

Both phases are assumed to be incompressible. Thus, the packing factor of the grains ($\phi = \rho_{gp}/\rho_p$) is constant, fixed to 0.6 in all our calculations as Jop et al. [78, 79] (the random close packing factor for spheres is 0.64), and the expansion of the granular phase due to the flow is neglected [79].

Notice that ϕ has not to be confused with α ; ϕ is the packing factor, that is the volume fraction occupied by the solid sphere in their 3D arrangement in the bulk; α is the volume fraction of the granular phase as fluid (i.e. with its voids filled with air). In fact, the density of granular phase is $\rho_{gp} = \rho_p \phi$.

2.2 Governing equations

It is possible to demonstrate that if the density in eq. (2.14) is a linear function of α the eq. (2.11) reduces to the usual expression for incompressible fluids:

$$\nabla \cdot \mathbf{u} = 0 \quad (2.15)$$

Doesn't matter the averaging function for η , in fact Lagr e et al. [88] used a harmonic function of α for the viscosity.

In eq. (2.12) $\boldsymbol{\tau}$ is:

$$\boldsymbol{\tau} = 2\eta\mathbf{D} \quad (2.16)$$

In eq. (2.14).b η_{gp} is given by JFP model:

$$\eta_{gp} = \left(\mu_s + \frac{\mu_2 - \mu_s}{1 + I_0/I} \right) \frac{p}{II_D} = \mu(I) \frac{p}{II_D} \quad (2.17)$$

Boundary conditions

The problem geometry has a planar symmetry that can be used to reduce the dimension of the computational domain. Only one half of the cylinder has been simulated (fig. 2.17), hence a symmetry condition has been imposed on the central symmetry plane $z = 0$:

$$\begin{cases} \mathbf{u} \cdot \mathbf{n}_z = 0 \\ \nabla \mathbf{u} \cdot \mathbf{n}_z = \mathbf{0} \end{cases} \quad (2.18)$$

and

$$\nabla \alpha \cdot \mathbf{n}_z = 0 \quad (2.19)$$

where \mathbf{n}_z is the normal to the symmetry plane (aligned with the z-axis).

On walls we choose a no-slip boundary condition that means:

$$\mathbf{u} = \boldsymbol{\Omega} \times \mathbf{r} \quad (2.20)$$

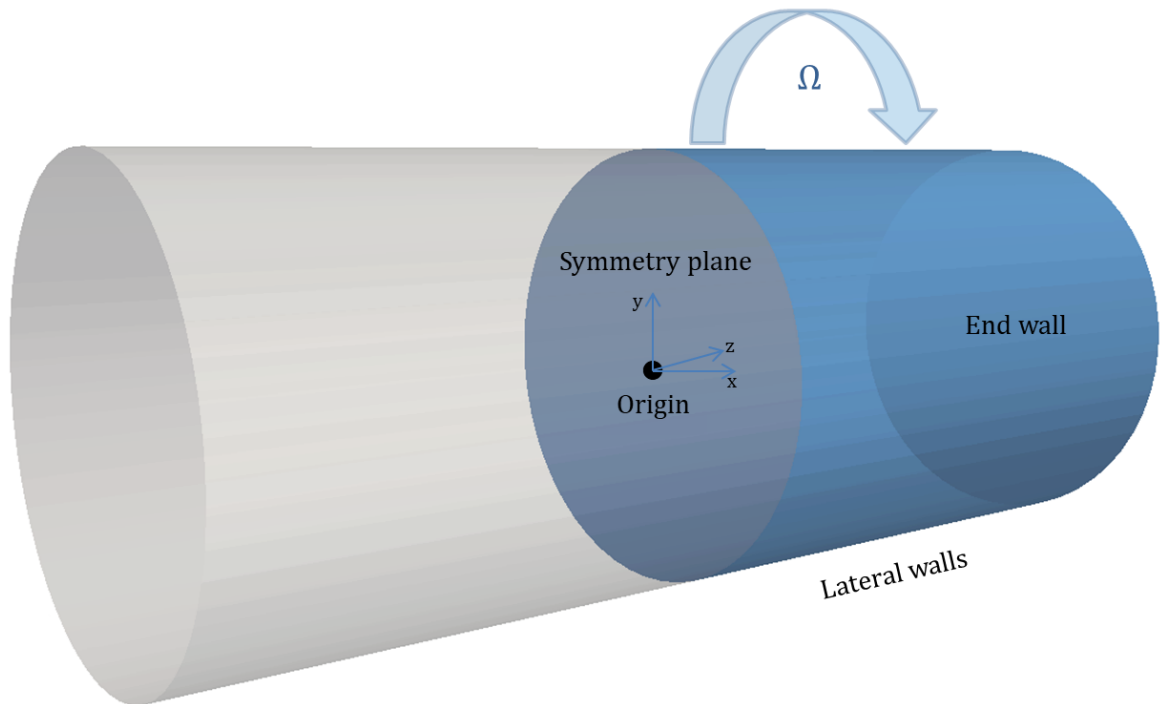


Fig. 2.17 Sketch of the problem geometry. Only one half of the cylinder has been simulated (blue coloured part).

where $\boldsymbol{\Omega}$ is the angular velocity vector and \boldsymbol{r} is radial position vector.

The boundary condition for α at walls is a zero gradient condition:

$$\nabla\alpha \cdot \boldsymbol{n}_w = 0 \quad (2.21)$$

where \boldsymbol{n}_w is the normal to the walls.

This is a standard α boundary condition of the solver that we have used to solve the equations above. We discuss the boundary conditions more in detail in the next section.

2.3 Numerical method

We use the *interFoam* solver of the open-source finite-volume software *OpenFOAM 2.1.1* [118] to solve the three-dimensional dynamical equations, implementing the JFP model in a homemade standalone routine. InterFoam solves the equations of motion for a two phases incompressible fluid with a specific version of the VoF model [17], and implements the PIMPLE algorithm to solve the transient problem. PIMPLE blends PISO [72] and the SIMPLE [125] algorithms, and includes one or more PISO loops inside one or more outer SIMPLE loops at each time step. These methods belong to the category of the “pressure-correction” methods, which derive a pressure equation from the continuity and momentum equations enforcing the mass conservation [50]. The presence of a pressure equation leads to the need of boundary conditions for the pressure itself. This is, in our opinion, one of the major downside of pressure-correction methods.

We imposed a symmetry condition on the symmetry plane:

$$\nabla p \cdot \mathbf{n}_z = 0 \quad (2.22)$$

and a pressure gradient at the walls called *buoyantPressure* in OpenFOAM, that means a pressure gradient equal to the hydrostatic one:

$$\mathbf{n}_z \cdot \nabla p = -(\mathbf{n}_z \cdot \nabla \rho)(\mathbf{g} \cdot \mathbf{h}) \quad (2.23)$$

where \mathbf{h} is the position vector.

Regarding mass conservation, it should be remarked that high-curvature or poorly resolved regions of the flow and advection errors may lead to mass loss [36]. Deshpande et al. [36] carried out a series of tests on the *interFoam* solver comparing its performance with those of different VoF formulations [45, 163]. They reported excellent mass

conservation features and acceptable advection errors for the interFoam solver, much smaller than those attained with other techniques.

In this thesis we adhere to the idea of compressive pressure of Jop et al. [79], and put to zero any negative pressure contribution inside the viscosity equation.

We modified interFoam solver to implement the JFP model. The JFP model predicts a divergent viscosity for the granular phase when the shear rate goes to zero. The divergence of the viscosity calls for a regularization, and we choose to set a viscosity cut-off, as suggested by Lagrée et al. [88], of $1550 \text{ Pa}\cdot\text{s}$ for the granular phase. We have tested that a different choice of the cut-off in the range 1000-150000 Pa s does not affect the results.

Dense granular materials commonly exhibit partial slip rather than a no-slip condition at the walls. Artoni et al. [7] reported an approximate expression for the slip length, which scales with particle diameter. In our simulations, no-slip boundary condition for velocity is instead imposed on all the drum internal walls, since in the corresponding experiments [146, 38] the inner walls were coated with a layer of rough material to avoid slipping. In the VoF method, however, the velocity field is evaluated at the cell centres, and this implies that, although with the no-slip condition the velocity at the drum walls should be ΩR , the method stores this velocity value in the cell centres adjacent to the wall, resulting in an effective (numerical) slip boundary condition [116]. For a mesh size Δx in a cell adjacent to the wall, the numerical slip length is $1/2\Delta x$ [75].

Notice that the slip length value obtained using the Artoni et al. expression for a granular material like the one we are considering is of the order of 10^{-3} m , which is the typical size of our mesh. Thus, even in presence of a no-slip condition at the wall, a motion of the contact line is guaranteed by the numerical slip. In this respect, Renardy et al. [136] showed that the contact line motion is indeed mesh dependent, but the

overall flow is only slightly affected by such a numerical slip. Our findings support this conclusion. We tested this by comparing results obtained with two different mesh resolutions at the walls (by just dividing each element of the mesh at the boundary in three identical cells), and keeping the rest of the elements at the same size. Free-surface shape, velocity, and thickness of the flowing layer are essentially unaltered by the (slight) change of the slip length due to the mesh size.

The condition (2.21) results in a contact angle of 90° between the wall and the interface [118]. We found that a change of the contact angle ($30^\circ - 150^\circ$) does not affect the overall dynamics.

The adopted geometry meshing is different for a different drum filling. In the case of large filling levels (to compare with Santos et al. experiments, see below), a hexahedral mesh is generated with two mesh generation utilities supplied with OpenFOAM, *blockMesh* and *snappyHexMesh* [118]. The former generates a background mesh of hexahedral cells that fills the entire region within the external domain boundary, while the latter adapts the mesh approximately to the surface by iteratively refining the starting mesh. In the case of low filling (to compare with Ding et al. experiments), in order to reduce the computational costs, a refinement of the mesh is performed only in the zone of the cylinder where the granular material is expected to be present. All our simulations are carried out on half domain by exploiting drum symmetry.

We performed convergence tests for every case performed in this work, refining the starting mesh.

Regarding the time step, it is adapted throughout the calculation in order to match a local stability criteria based on the *Courant number*, Co [17]. To achieve temporal accuracy and numerical stability, a Courant number of less than a maximum value is required.

The Courant number is defined for one cell as:

$$Co = \frac{\delta t |\mathbf{U}|}{\delta x} \quad (2.24)$$

where δt is the time step, $|\mathbf{U}|$ is the magnitude of the velocity through that cell and δx is the cell size in the direction of the velocity. The flow velocity varies across the domain and we must ensure $Co < Co_{max}$ everywhere. If anywhere in the mesh the local Co exceeds the critic value, the time step is decreased to have a new local Co below the limit.

In each subsection of the section *Results* we discuss more in detail the adopted procedure for choosing the element number of the mesh. We have chosen a maximum Co of 0.8 for all the simulations, decreasing this value our results have not changed. A maximum time step size of 0.01 s has also been used for all the simulations.

2.4 Results

We have compared our predictions with some experimental results available in the literature for several flow conditions, which differ in terms of cylinder angular velocity Ω , filling degree f , particle diameter d_p , particle density ρ_p , cylinder diameter D , and cylinder length W . All the parameters used in our simulations are reported in table 2.1. We first report results reproducing the entire succession of flow regimes identified by Mellmann, i.e. rolling, cascading, cataracting, and centrifuging, and compare our simulations with Santos et al. [146] experiments. By aid of the very recent results by Balmforth and McElwaine [11] we also show the ability of the model to capture the so-called slumping regime at very low rotation rates. Then, we report a comparison between our simulations and the experiments by Ding et al. [38] on some detailed features of granular flow, as shape of free-surface, superficial velocity, and velocity

Table 2.1 Parameters used in our simulations and experiments of comparison for the mono-disperse case

	<i>Exp</i>	$\Omega[\frac{rad}{s}]$	$f[\%]$	$d_p[\text{mm}]$	$\rho_p[\frac{g}{m^3}]$	$D[\text{cm}]$	$W[\text{cm}]$	μ_s	μ_2
A	[146]	1.45, 4.08, 8.91, 16.4	31.4	1.09	2.46	19.5	50	0.39	0.55
B	[146]	12	18.81	1.09	2.46	19.5	50	0.39	0.55
C	[11]	0.4 and 0.8	50	10	2.9	28.7	11	0.59	0.67
D	[38]	0.18	10	1.5	2.9	40	100	0.4	0.46
E	[129]	4.08	18.81	1.09	2.46	19.5	20.1	0.39	0.55
F	[129]	4.08	18.81	1.09	2.46	19.5	5.07	0.39	0.55

inside the bed. Finally, we conclude with the analysis of axial flow comparing our simulations with Pohlman et al. [129] experiments.

Comparison with experimental results of Santos et al. [146]

In this section we report the analysis of the flow in a 3D rotating cylinder using the parameters in row “A” of the table 2.1. The experiments refer to steady state situations, so we carried out our simulations until the attainment of steady regime conditions.

The parameter values to be chosen for the JFP equation are derived as follows: i) I_0 is fixed to 0.279 as suggested by Jop et al. [79]; ii) μ_s and μ_2 for the glass particle of 1.09 mm are obtained by linear interpolation from Pouliquen [132] data for glass beads with diameters of 0.5 mm and 1.3 mm, and their value are reported in table 2.1. We remark again that those parameter values are fixed once and for all, as they only depend on the nature and size of the grains (glass beads, in this case).

The mesh adopted is shown in fig. 2.18. Mesh convergence of the results is attained with 310388 elements.

Figure 2.19 shows the distribution of the granular and the gas phase of our simulation results for “A” flow conditions (second row) and the corresponding experiments from Santos et al. (first row). The third row compares our simulation results of the interface

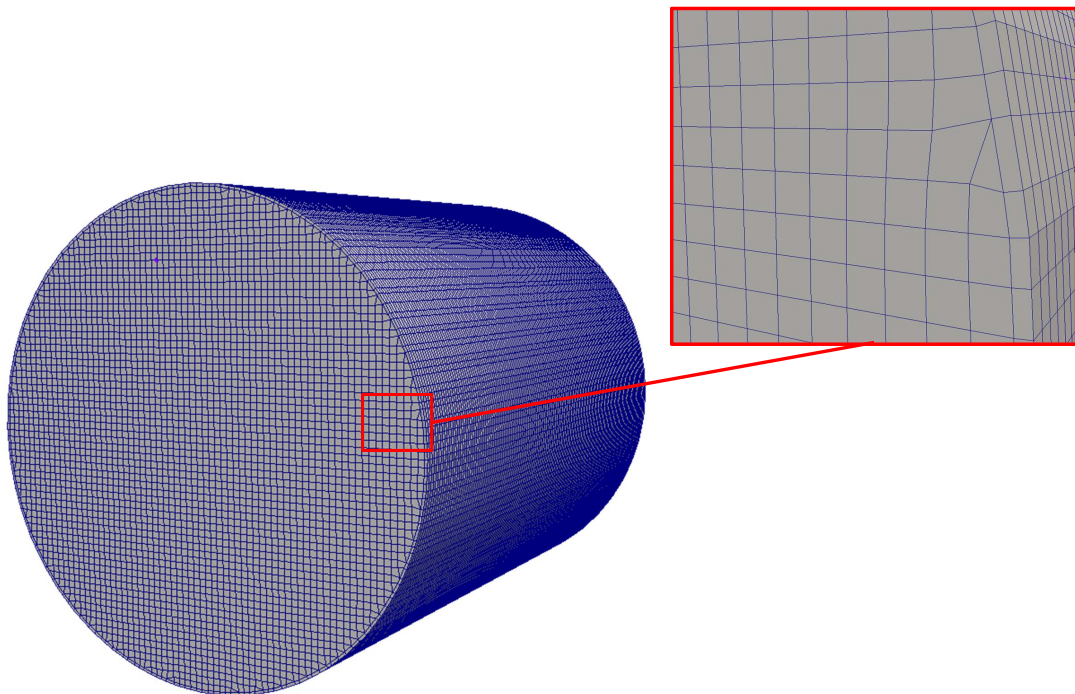


Fig. 2.18 Adopted mesh (“A”).

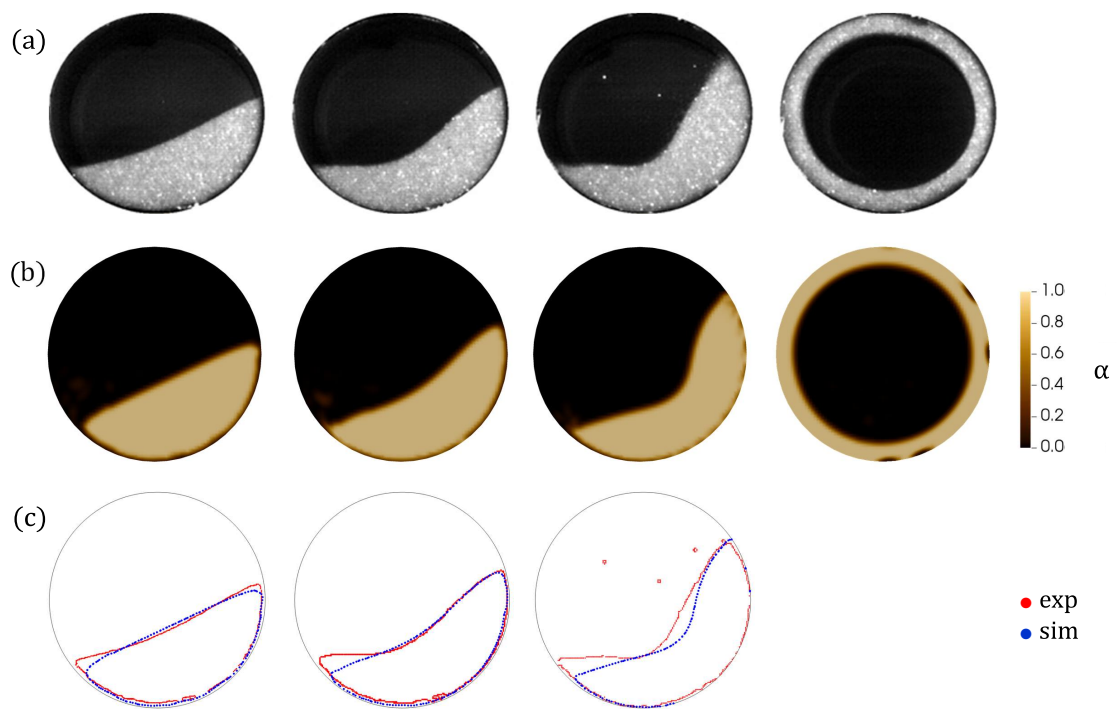


Fig. 2.19 Different flow regimes (see at table 2.1 for corresponding velocities) filling degree 31.40%. **(a)** Experimental results of Santos et al. [146] **(b)** Our simulation results. **(c)** Comparison between interfaces from experiments and simulations.

($\alpha = 0.5$) with the experimental interface obtained through image analysis. In the figure, the colour scale represents the volume fraction α , ranging between 0 for the air (black) and 1 for granular phase (ochre). Notice that our results are taken on the symmetry plane of the drum, i.e. at the cylinder half length, whereas the experiments report the situation on the transparent glass wall. As remarked by Santos et al., however, the observed velocities at end of the drum are very close to those at the middle of the drum.

The succession of flow configurations identified by Mellmann with increasing drum rotational velocity, and reproduced in Santos experiments, i.e., rolling, cascading, and centrifuging, is correctly captured by our simulations. At the lowest angular velocity (1.45 rad/s) rolling motion takes place, where a uniform particle layer (flowing layer) continuously flows in the upper part of the bed, while the beads in the bulk essentially follow the rigid rotation of the cylinder (plug region). The shape of the free surface in this rolling regime is nearly flat. As the rotational speed increases (4.08 and 8.91 rad/s), the bed surface begins to arch, and assumes an S-shape that defines the cascading regime. In fact, the main difference between rolling and cascading regimes in Mellman’s categorization is the shape of the free surface. Our simulations demonstrate an excellent quantitative agreement between the predictions based on the JFP constitutive equation and the experimental results in these regimes. As illustrated in figure 2.19c, the predicted and observed free-surfaces essentially coincide. A small discrepancy is observed in the “tail” of the bed (leftmost part near to the drum wall), where our interface is systematically, though slightly, below the actual one. We believe that such discrepancy is due to a local variation of the packing factor in the experiments. Indeed, in the experiments one can notice a reduction of intensity in the tail of the granular bed, corresponding to a kind of “rarefaction” of the bed; this scenario is obviously out of reach in our simulations, as we assume that the packing

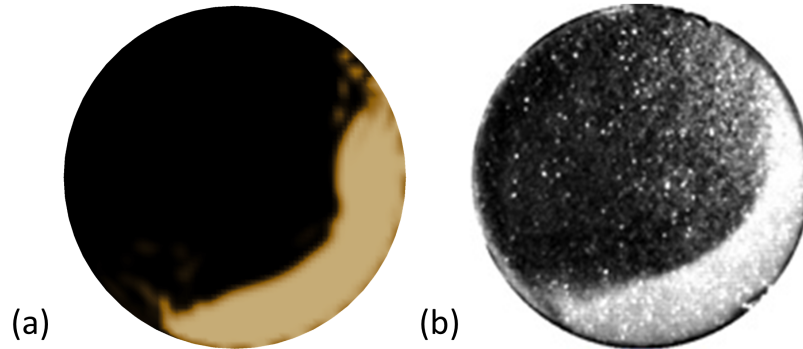


Fig. 2.20 Cataracting regime at filling degree 18.81%. **(a)** Our simulation at 12 rad/s, **(b)** experimental results at 16.4 rad/s, (see main text).

factor is strictly constant. It remains true, however, that simulations reproduce the experiments both in the sequence of regimes and in their range of occurrence in terms of rotational velocity. Such predictive capability is worth stressing, since rolling and cascading regimes are thought to ensure the best degree of mixing and heat transfer, and for this reason such flow configurations are the most frequently encountered in industrial applications [111]. Simulation results, of course, are very rich in details, and give the possibility of quantifying fields of interest like, e.g., the pressure field and velocity fields both at the interface and in the bulk of the bed (see subsection 2.4). Thus, simulations would ensure proper design solutions in terms of mixing capability in the rotating drum. Finally, at the largest rotational speed, a uniform layer of grains covers the internal walls, in a centrifuging motion, (see figure 2.19a-4, at 16.4 rad/s), both in experiments and in simulations.

Figure 2.20 shows the comparison between our simulations (at 12 rad/s) and the experimental results of Santos et al. in the case of 18.81% filling degree, and at 16.4 rad/s (“*B*” in table 2.1). In experiments, cataracting motion is observed (figure 2.20.b), a regime characterized by particles massively thrown into the drum free space occupied by the gas. At variance with experiments, our calculations (not shown) predict, in the same operating conditions, a centrifuging regime. At a slightly lower rotational speed

(12 rad/s), simulations show a cascading regime (figure 2.20.a), where distinguishable “drops” of granular phase detach from the top of the bed and are thrown inside the cylinder free space. This condition is very similar to the cataracting regime. A similar discrepancy between experimental and simulations results is also reported by Santos et al., and is attributed by those authors to possibly inaccurate no-slip boundary conditions. In the experiments, the inner walls were coated with a layer of rough material to avoid slipping, but at such a low filling degree and at such high rotational velocity some slippage might indeed arise. We believe that another possible clue for the discrepancy might again be the variable density of the granular phase, which is not accounted for in the JFP model we use. It should be remarked, in closing this section, that also in this cataracting regime the predicted shape of the bed is astonishingly close to the measured one, even in fine details like the bed tail in the leftmost part of the drum.

Slumping regime

At lower rotational speeds with respect to those examined in the previous section, Mellmann [111] reports the existence of a slumping regime. The very recent work by Balmforth and McElwaine [11] reports a rich experimental data set in such slumping regime. They point out how cascades in the top of the bed periodically occur. Such cascades contribute to decreasing the free-surface angle from θ_{start} to θ_{stop} (the angle is measured as the surface slope at the central position with respect to the horizontal); afterward, a rigid rotation of the bed restores the higher angle, and the cycle repeats.

Hence, in the slumping regime, the almost flat free surface periodically oscillates between two limiting angles. To reproduce the slumping regime with our approach, we have first of all selected operating conditions such that the limiting angle range is rather wide. This choice is motivated by the advantage of obtaining a clear manifestation of

the oscillations in this regime. Following the indications by Balmforth and McElwaine [11], we fix the parameters as in “C” in table 2.1. Indeed, Balmforth & McElwaine find that, with such a drum geometry, the slumping-to-rolling transition occurs in a velocity range of $10^{-3} - 10^{-1}$ rad/s for glass beads in the range $1.5 - 5mm$; they also remark that, by increasing the particle diameter, the velocity at which such transition occurs increases. This is the reason why we have chosen rather large particles ($10mm$), so as to attain slumping at a rather large angular velocity, and thus allowing simulations to be run in reasonable computational times. Values for μ_s and μ_2 were fixed as follows: 1) in Balmforth & McElwaine, it is indicated that, for 10mm particles, $\theta_{start} = 34^\circ$ and $\theta_{stop} = 28^\circ$; 2) they also observe that, within the slumping regime, these angles stay essentially unaltered as the rotation rate is varied; 3) from the given values for θ_{start} and θ_{stop} , we compute the values for μ_s and μ_2 reported in table 2.1 from the well-known relations for flow on an incline [53].

The mesh adopted is qualitatively very similar to the one in fig. 2.18. In this case, the chosen mesh has 209720 elements.

Figure 2.21.a shows the time series of the predicted surface angle dynamics for an imposed rotation rate of 0.8 rad/s. It can be noted that, after a long transient, the oscillation damps out, and the surface eventually reaches an angle around 35° . The attainment of a stable stationary free-surface angle is typical of the rolling regime [111]. Then, to capture slumping by simulations, we reduced the velocity by 50%. Figure 2.21b shows a sustained oscillation regime, reached after an initial transient. Qualitatively, the regime oscillation is characterized by a quasi-periodic signature very similar to those experimentally found in Balmforth & McElwaine. On average, $\theta_{start} \approx 35^\circ$ and $\theta_{stop} \approx 32.5^\circ$. A fair qualitative agreement is found with the data by Balmforth & McElwaine, though the oscillation amplitude is lower in the simulations. Averaging the time lags between two peaks, that means the time elapsed between the

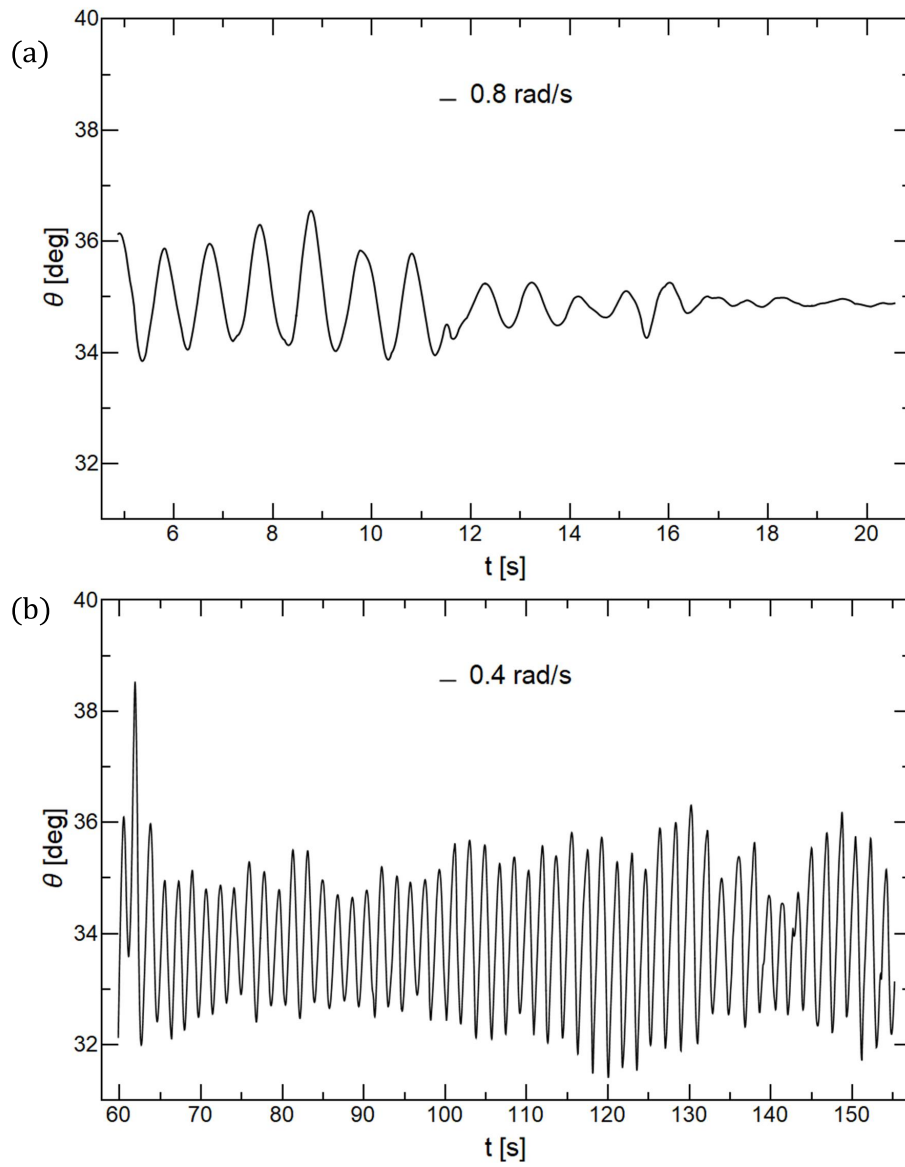


Fig. 2.21 Time series of surface angle. **(a)** $\Omega = 0.8$ rad/s (reaching a steady state). **(b)** $\Omega = 0.4$ rad/s (periodic oscillations).

beginnings of two cascades, we can obtain the characteristic time of rigid rotation that restore the maximum angle: $1.8s$. Within such a time span, the cascade time almost equals the “rising” time, a feature expected close to the slumping to rolling transition.

This is the first time that the slumping regime has been observed through continuum modelling; this result show the great capabilities of our numerical approach to capture fine details, e.g., transitions between different flow regimes, which are quite difficult to be accessed through experiments, and which are not predictable through DEM simulation for large cylinders with billion of particles.

Comparison with experimental results of Ding et al. [38]

Ding et al. [38], through adoption of refined imaging techniques (PEPT, Positron Emission Particle Tracking), measure surface and bulk velocities, together with surface shapes, at the symmetry cross-section of a rotating drum. We now report on our simulation results on such subtle features of the flow field, and compare predictions with experiments. For the parameters adopted in our simulations, see line “ D ” in table 2.1. We will consider the free-surface shape, the granular velocity on the free surface, and the velocity within the granular bed.

The mesh adopted is showed in fig. 2.22. Mesh convergence of the results is attained with 442750 elements.

Figure 2.23a shows the shape of the free surface from simulations and experiments. Our results give the steady state surface shape attained after about 10s from start-up: the surface reaches a constant angle of 23° . The agreement with experiments is quantitative.

At variance with the free surface shape, the calculated velocities do not attain a steady state. Consequently, we plot those data by reporting averages and standard deviations, to account for the persistent oscillations predicted by the numeric. Figure

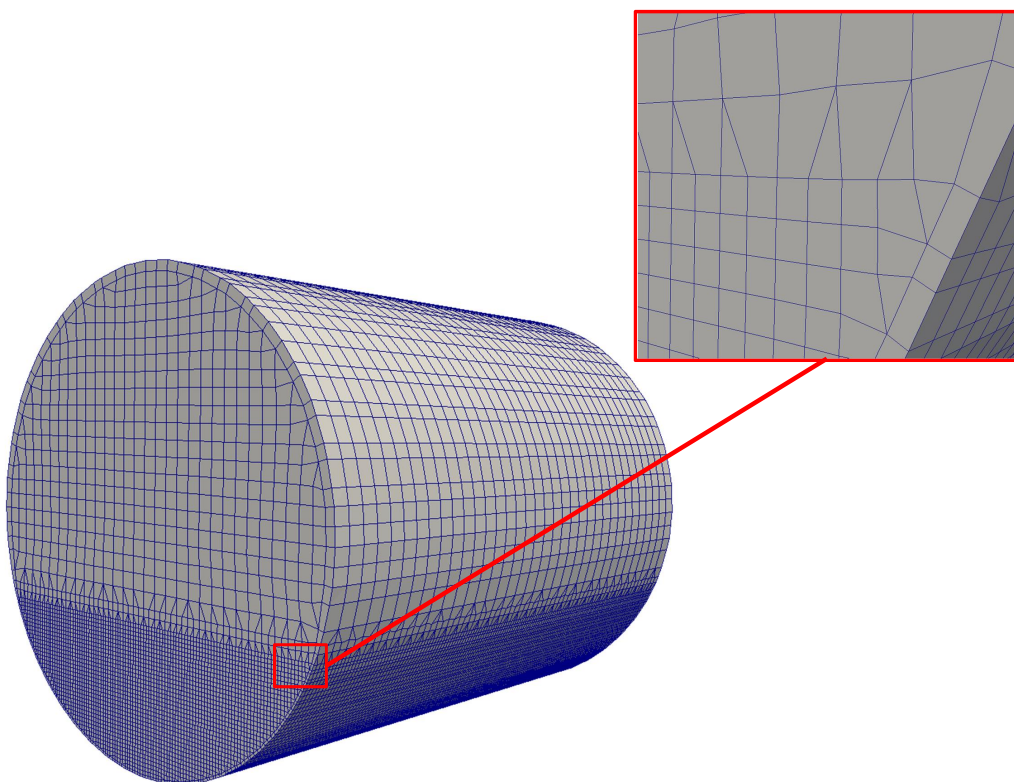


Fig. 2.22 Adopted mesh (“C”).

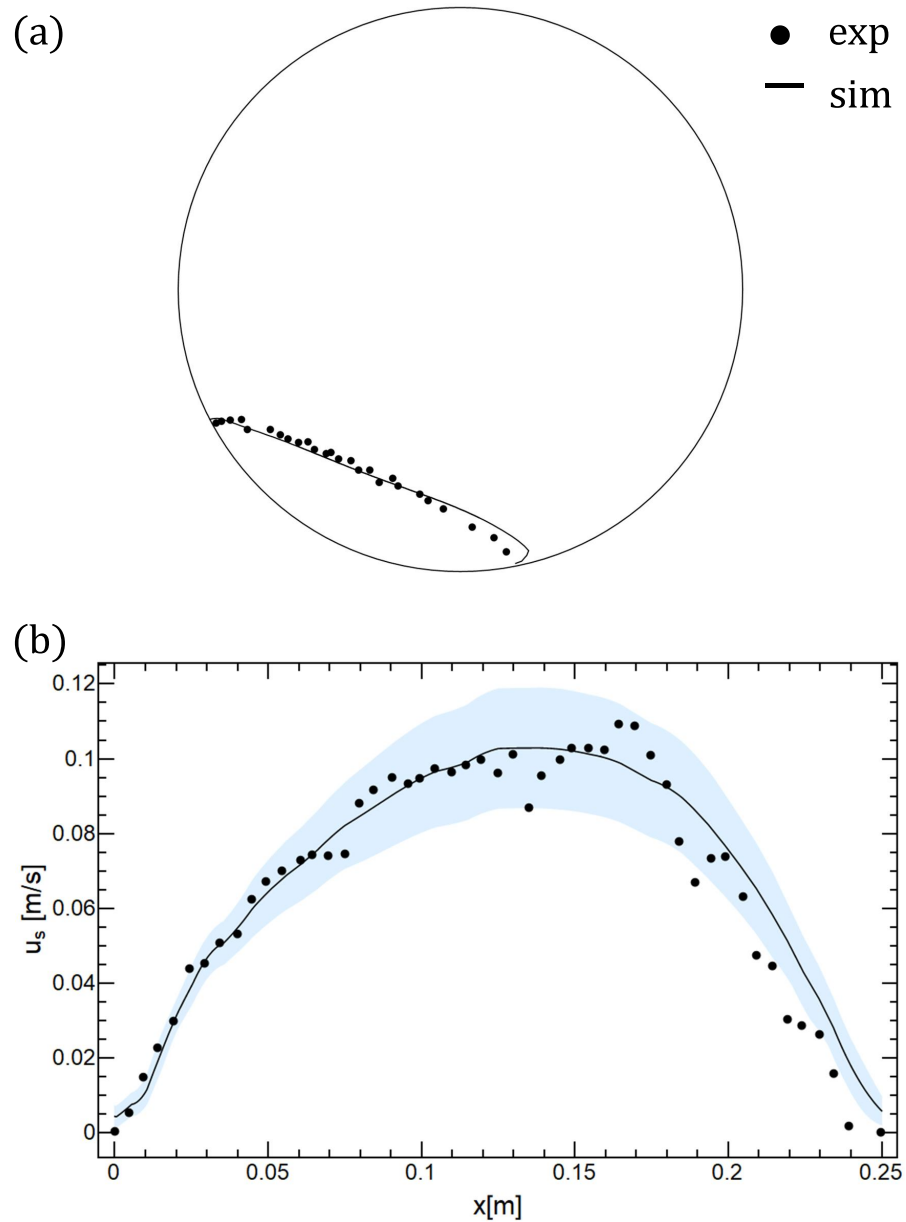


Fig. 2.23 Comparison between our simulation results (line and shaded area) with Ding et al. experiments (points). **(a)** Shape of the free surface typical of the rolling motion. **(b)** Bed surface velocity profile, u_s , versus the x -direction. **(c)** x -direction velocity throughout the depth of the granular bed, for two different dimensionless x -coordinates (see main text).

2.23.b shows the bed surface velocity profile, u_s , plotted as a function of a coordinate x on an axis going from the top to the bottom of the free-surface, as in “figure 1” in Ding et al. [38]. Agreement is excellent throughout the surface, with the slopes close to cylinder walls and the velocity maximum value being quantitatively predicted with the JFP constitutive equation. The largest value of the superficial velocity occurs around the mid-chord position; hence particles moving at the surface accelerate until they reach the mid-chord, and then decelerate. The standard deviation measured in the numerical simulation (showed with shaded area) encloses very well the spread of the experimental data.

Figure 2.24 shows x -component of the velocity within the granular bed, at two different x -coordinates (x is made nondimensional through the chord length $2L$). The y coordinate measures the depth within the bed, and it is $y = 0$ at the free surface. Agreement between experiments and predictions is quite good. As expected, and as shown in the experiments, the largest x -component velocity in the active region is at the free surface, and makes the flow field similar to a chute flow [148]. As Ding et al. reported, by increasing y/R , i.e., moving towards the cylinder wall, the x -component of velocity eventually attains the wall velocity, which theoretical value in case of no-slip is $|\Omega R| = 0.036\text{m/s}$, very close to the effective value, thus indicating that the slippage between the inner wall and the granular bed is indeed small.

Finally, we have analysed the average velocity profile in the bed depth at the mid-chord position ($x/2L = 0.25$), as predicted by our simulations. It so appears that, moving from the free-surface along the y -direction (fig. 2.25), the average velocity in the flowing layer is well fitted with a Bagnold-like profile [10], with the velocity given by $u = u_{TOP}(1 - a \left(\frac{y}{R}\right)^{3/2})$, where a is a fitting parameter and u_{TOP} corresponds to the velocity at the free surface. (Notice that, in fig. 2.25, we subtracted the rigid rotation velocity.) In the “jammed region”, close to the wall, an exponential-like tail

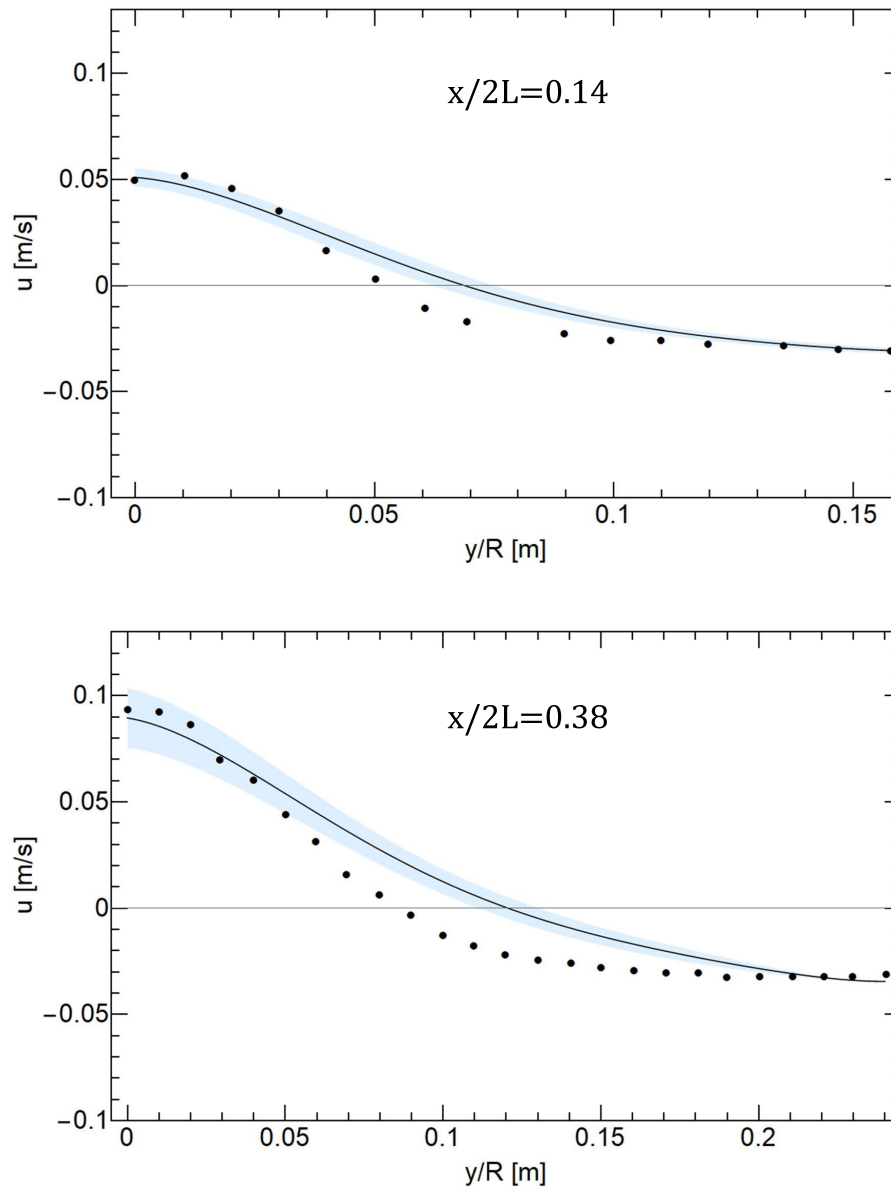


Fig. 2.24 x -direction velocity throughout the depth of the granular bed, for two different dimensionless x -coordinates (see main text).

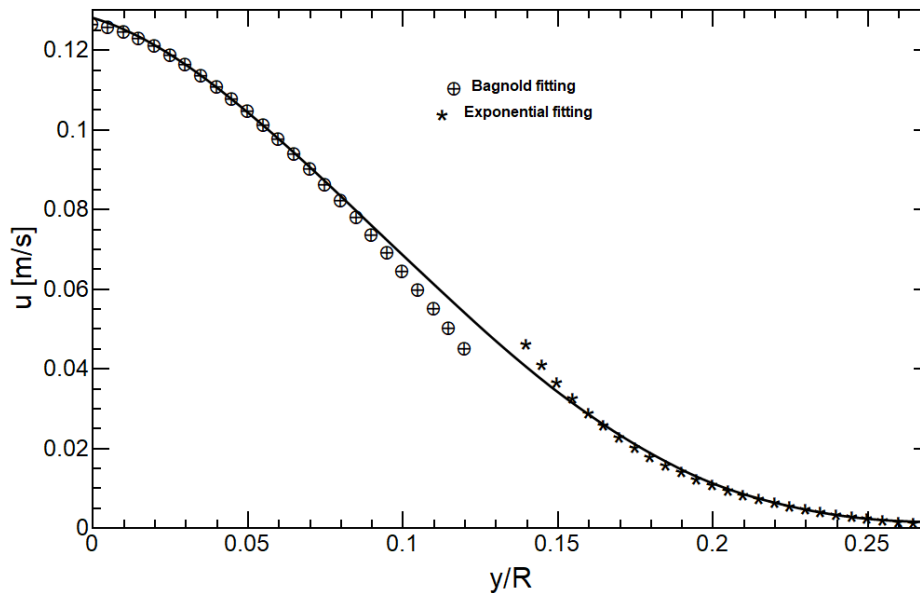


Fig. 2.25 Our simulation results (line) for x -direction average velocity (scaled of the rigid rotation) throughout the bed depth, at the mid-chord position. Fittings by Bagnold profile in the flowing layer (\oplus symbols) and by an exponential curve in the rigidly rotating part ($*$ symbols).

gives a reasonable fit. The two fitting in figure 2.25 are $u_b = 0.127 - 1.96(\frac{y}{R})^{3/2}$ and $u_e = -1.46 \cdot 10^{-3} + 1.07 \cdot e^{-22.2\frac{y}{R}}$ are respectively the Bagnold and the exponential fitting.

Comparison with experimental results of Pohlman et al. [129]

Pohlman et al. [129] measured the velocities of particles at the free surface of the rotating tumbler using *Particle Tracking Velocimetry* (PTV). For the parameters adopted in our simulations, see lines “F” and “G” in table 2.1.

In the following simulations we have adopted a mesh of 310388 for AR=1.03 and 132080 for AR=0.26, as results of spatial convergence.

As mentioned before in section 2.1.1, Pohlman et al. [129] investigated the free surface velocity of 3D cylinders changing the drum width hence, to reproduce qualitatively their experimental results we have changed the width of the cylinder in case “A” (tab.

2.1), in order to have the same aspect ratio (AR) used by the authors. They reported the stream-wise velocity, normalized with the velocity value on the symmetry plane at the mid-chord position, as a function of the axial position and observed a velocity close to the wall 20% higher than that at the centre when $W/D > 1$, even though the particles on the wall were slower due to friction, in fig. 2.26 the comparison with our simulative results is showed. The agreement is very satisfying.

Chen et al. [28] conducted a similar numerical study using the discrete element method for the granular flow inside 2D and 3D drums. They found a good agreement with prior measurements at the surface by Pohlman et al. [129]; they found a region of high speed flow with axial components of velocity occurs near each end-wall in long tumblers. The increase of the velocity near the end-wall is lighter than that reported by the experimental measurements of Pohlman et al. [129]. Chen et al. [28] found a velocity close to the wall 10% higher than that at the centre for $W/D = 1.43$, while Pohlman et al. [129] reported a value of 20% for $W/D > 1$, consistently with our simulations.

So, we can conclude that although DEM simulation can capture several features of granular flows, our continuum approach seems more accurate in describing granular flows in 3D long cylinders with many particles.

In fig. 2.27 are showed our simulative results for contour and density plot of the axial component of the free-surface velocity for $AR = 0.26$ and $AR = 1.03$. The axial velocity is normalized by the speed value on the symmetry plane at the mid-chord position. The velocity vector map is represented by arrows. The free-surface velocity in both cases is directed toward the centre in the upper part of the free surface and toward the end walls in its lower part, in fact the magnitude of the axial velocity is bigger in the cylinder corners. The two areas are not symmetric: the zone near the top of the free surface is bigger in size, but weaker than the bottom area. Our results in

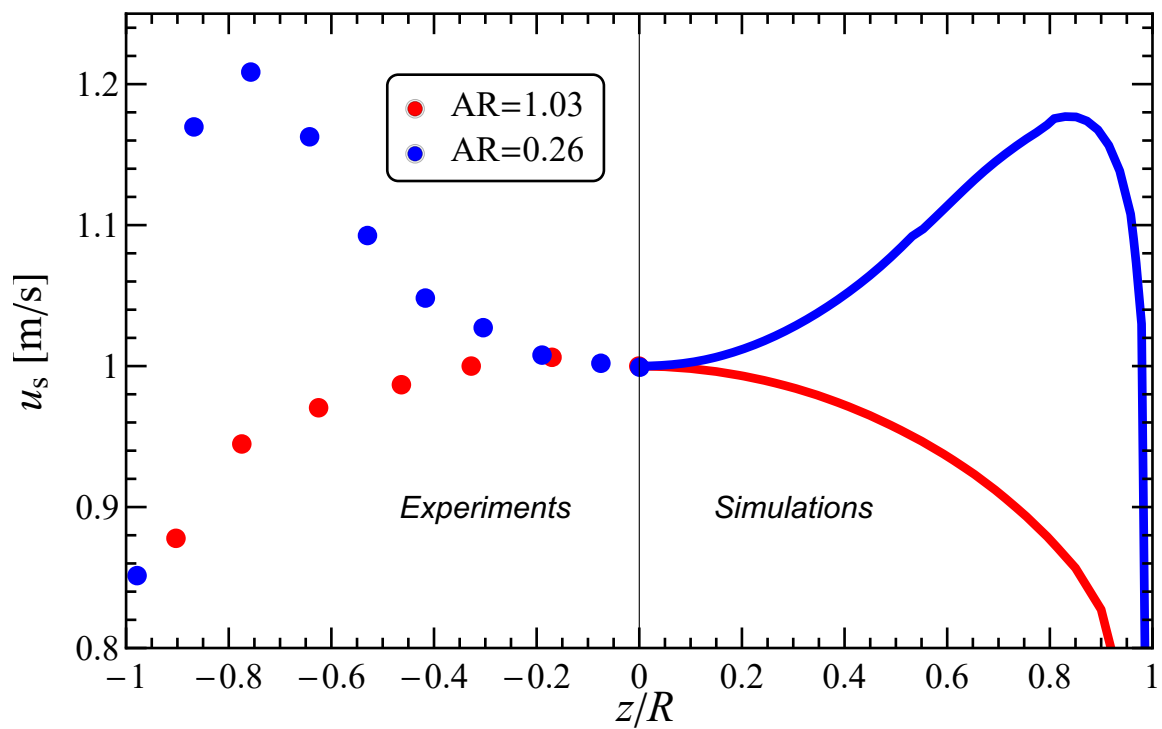


Fig. 2.26 Predicted and experimental stream-wise velocity profile along the axial direction varying the aspect ratio. Our simulation results (lines on the right) for stream-wise velocity along the z -direction, at the mid-chord position of the free-surface. On the left experiments by Pohlman et al. [129]. Blue is used for $AR = 1.03$, red for $AR = 0.26$.

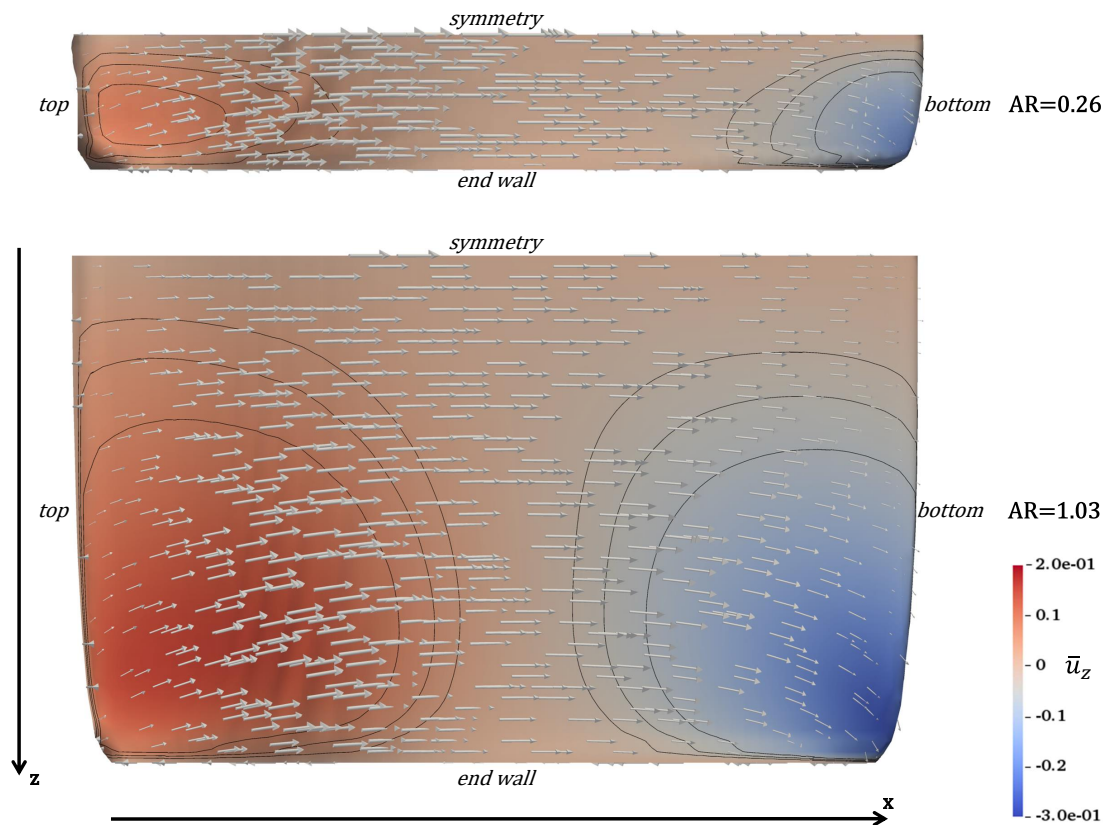


Fig. 2.27 Density plot of the axial velocity on the free surface and velocity vector map represented by arrows, parametric in the aspect ratio. On the left experiments by Pohlman et al. [129]. On the top of the figure: $AR = 0.26$, on the bottom: $AR = 1.03$. Contours at ± 0.03 m/s, ± 0.046 m/s and ± 0.07 m/s. The cylinder end wall, the cylinder symmetry plane, the top and the bottom of the avalanche are specified for clarity.

fig. 2.27 are consistent with the observation made by Pohlman et al. [129] showed in fig. 2.6.

Chapter 3

Mixing of bi-disperse granular material

3.1 Literature review

Granular mixing in three-dimensional systems is a complex operation, since a difference in particle size, shape or density can lead to segregation. These differences between two or more granular phases can lead to very complex and different segregation patterns depending on all operating conditions. Segregation is the major issue in granular processes [110]. Unlike the mixing of liquids, the flow and mixing of granular materials is poorly understood and a general framework is still lacking [122]. In fact, segregation has been discussed by a great number of authors in literature but results are discordant.

For this reason, this chapter begins with a short review of the literature regarding those aspects of mixing where some agreement has been reached.

Then, we will present the comparison between our simulation results and experiments on mixing of bi-disperse granular media different only in colour or different only in density. Our aim is to evaluate if the continuum approach with JFP model allows to simulate the dynamic behaviour of two different granular materials in a 2D tumbler.

The ultimate goal is to predict some aspects of axial segregation observed in the experiments of Taberlet et al. [157] and Taberlet et al. [158] and reported in the results of [70] by means of 3D CFD simulations.

3.1.1 Experimental literature

Nityanand et al. [117] described the radial segregation obtained in their work stating that, at low rotational velocity, percolation dominates on inertia, hence smaller particles sink to lower levels in the flowing layer following the inner streamlines, and this leads to the formation of a smaller particles core. On the other hand, at high drum speeds, inertia dominates, and the segregation pattern reverses, with the smaller particles on the drum walls instead that inside the core.

The just mentioned experimental result at low rotation rate was confirmed by Pollard and Henein [130], who focused on radial segregation due to size differences of irregularly shaped particulate solids in horizontal rotating cylinders. Moreover, they reported that the rate of segregation is faster if difference in particle size is larger.

Wightman and Muzzio [164], on the other hand, observed the reverse phenomenon, namely, that large particles concentrate in the core, at least for the examined rotation rate.

Core segregation was reported too by Alonso et al. [4], who found that, at a given rotation rate, smaller or heavier particles concentrate in the core of the bed, but size and density can somehow compensate with each other, contrasting segregation. They performed experiments in a quasi 2D-cylinder.

Ottino and Khakhar [120] also reported on the effect of density and size of particles on segregation patterns in a quasi 2D-cylinder in their review. In the experiments, they used glass and steel beads with various diameters.

Cantelaube [25] studied the dynamics of a large diameter particle intruded in a bed of small particles. They found a migration of the intruder bead to the centre of the bed, see fig. 3.1 for the experimental result.

Clément et al. [30] investigated the mixing of steel particles in the slumping regime, with particles only differing in size. They reported that largest particles tend to stay in the cylinder outer region more than small particles (see fig. 3.2). The same authors stated that the centre of the cylinder and the outer zone near the walls “attracted” the trajectory distributions. So, the size segregation mechanism can be seen as the predominance of one attractor compared to the other. The authors talks about a bi-stability transition controlled by the size ratio.

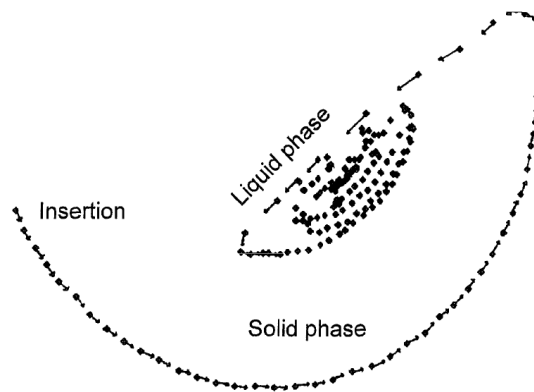


Fig. 3.1 Dynamic of a bead intruder greater than the bulk particles [25].

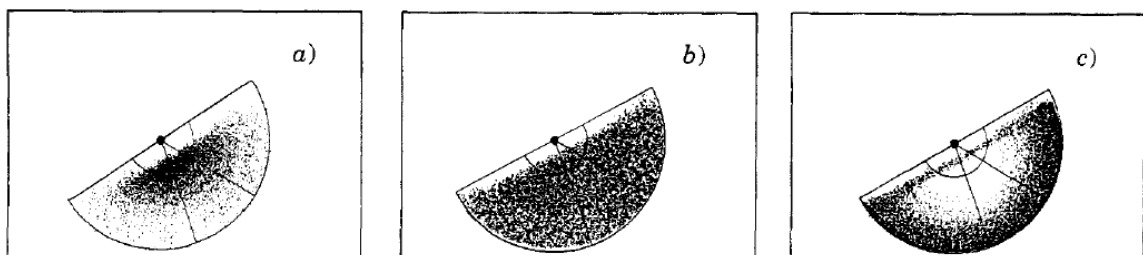


Fig. 3.2 Segregation patterns when 1.5 mm steel beads (white) are mixed with 1 mm (a), 1.5 mm (b), 2 mm (c) steel beads [30].

Khakhar et al. [86, 85] focused their attention on the radial segregation and the core formation due to density difference of two types of particles equal in size, comparing experimental, DEM, Monte Carlo, and continuum theory results. The analysis is restricted to low speeds of rotation, when the free surface of the granular solids is nearly flat. They reported a formation of a central segregated core of the denser particles.

McCarthy et al. [108], too, studied density- induced segregation, comparing experimental results with Particle Dynamics and Lagrangian Simulation results. The heaviest particles form a bulk core.

Jain et al. [73] presented an experimental investigation of size, density, rotational velocity, and filling effect on mixing. They used a half filled quasi-2D drum filled with a bi-disperse mixture of equal volumes of different sizes of steel and glass beads. They observed “radial streaks” or a “classical core” (see fig. 3.3 and fig. 3.5). When percolation and buoyancy act in the same direction, that means when the smaller particles are also the heavier, a core of smaller denser particles takes place; the formation of streaks depends on the size ratio of the two type beads: the larger is the diameter ratio the more uniform is the core boundary, see fig. 3.3. For diameter-density couplings where percolation and buoyancy oppose to one another, there is a transition from a core composed of denser beads to a core composed of smaller beads (see fig. 3.4). They observed that mixing can be achieved if the denser beads are also bigger and if the ratio of particle size is larger than the ratio of particle density. The pattern depends on the interplay size-density, and on drum speed (see fig. 3.5).

Xu et al. [166] studied mixing behaviours of equal-sized (but differently coloured) glass beads in a rotating drum by both 2D DEM simulations and experiments. They experimentally observed the mixing process in various flow regimes and concluded that experiments indicated that higher rotation speed can enhance mixing.

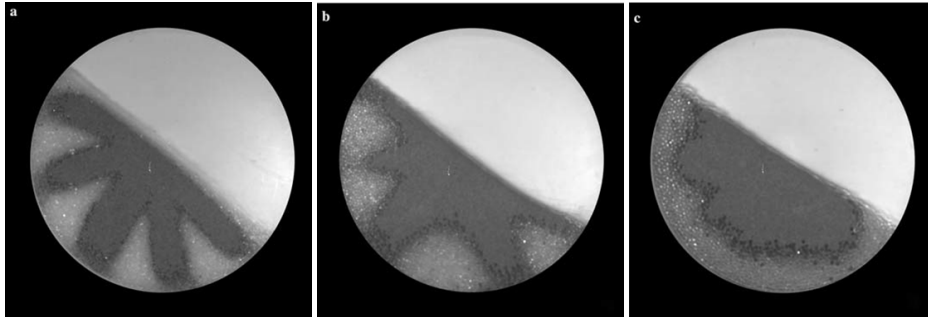


Fig. 3.3 Segregation patterns when buoyancy and percolation mechanisms act in the same direction after 2 revolutions. 1mm steel beads with 2mm (a), 3mm (b), 4mm (c) glass beads [73].

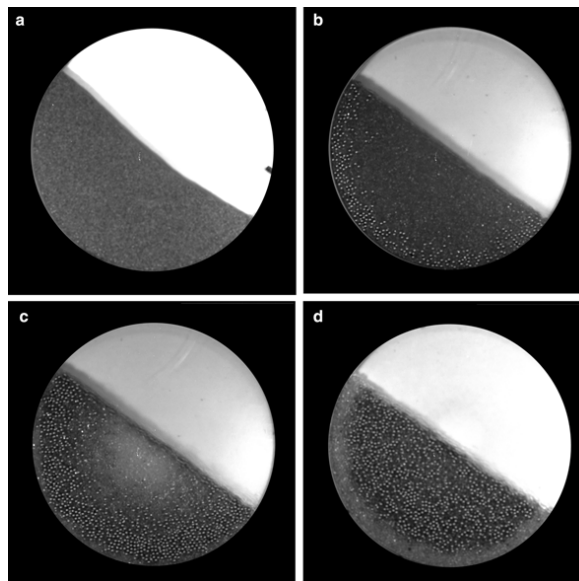


Fig. 3.4 Segregation patterns when buoyancy and percolation oppose each other after 20 revolutions. 4mm steel beads with 0.2mm glass beads (a): no segregation, 1mm glass beads (b): bands of steel beads near walls, 2mm glass beads (c): small core of glass beads, a band of glass beads near walls, and a band of steel beads between them, 3mm glass beads (d): glass beads on the periphery [73].

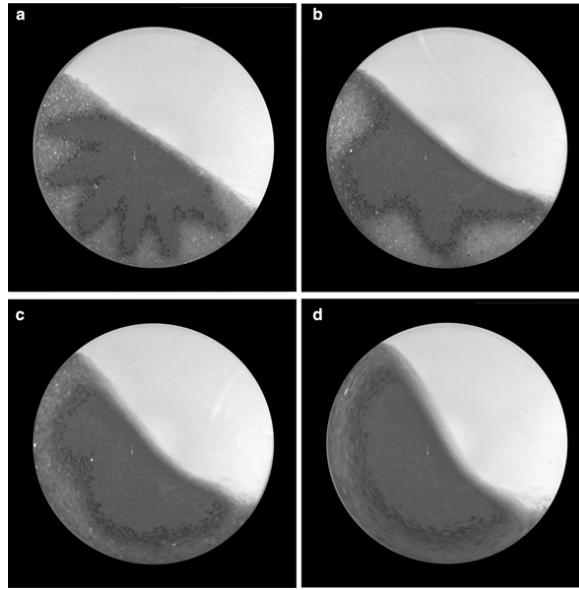


Fig. 3.5 Segregation patterns depending on drum speed after 20 revolutions. 1mm steel beads and 3mm glass beads at 1rpm (a), 4rpm (b), 8rpm (c), and 16rpm (d) [73].

Metcalfe et al. [113] focused their attention on the segregation pattern for salt grains coloured in two different ways for the avalanching regime. The same authors performed simulations using a “random map model”. They reported that the mixing is hampered by filling greater than 50% (fig. 3.6).

McCarthy et al. [109] confirmed the results of Metcalfe et al. [113] and extended the study of segregation patterns to different geometries (2D and 3D) by means of experiments and simulations. They merged molecular dynamics simulation and geometrical considerations to reduce the computational time. They found the optimal filling for mixing in each geometry studied, by defining a “mixing efficiency” that also accounts for the amount of interface reached during mixing. In fig. 3.7, the dependence of such efficiency on filling is reported, showing that the best fill correspond to 0.25 for a circular section of the drum. In this case, they also show that a core occurs when the drum is more than half-filled.

Metcalfe et al. [112] studied the effect of the aspect ratio in rotating drum using MRI technique and focusing the attention on core size and patterns. They found that

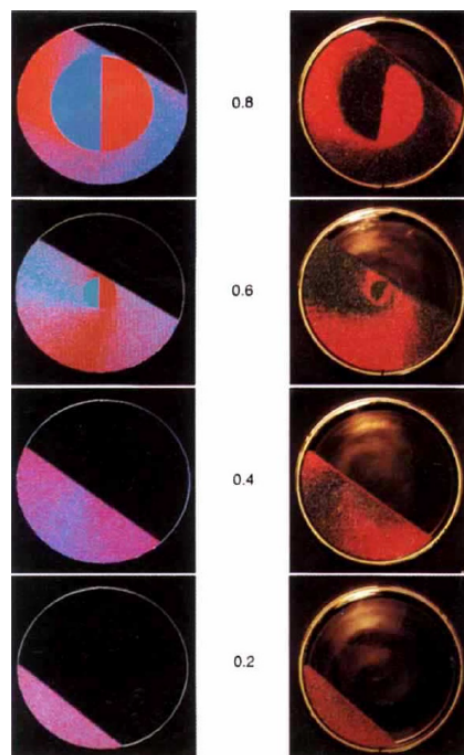


Fig. 3.6 Segregation patterns for avalanching regime at different filling degrees after 2 revolutions. Simulation results on the left, experimental ones on the right [113].

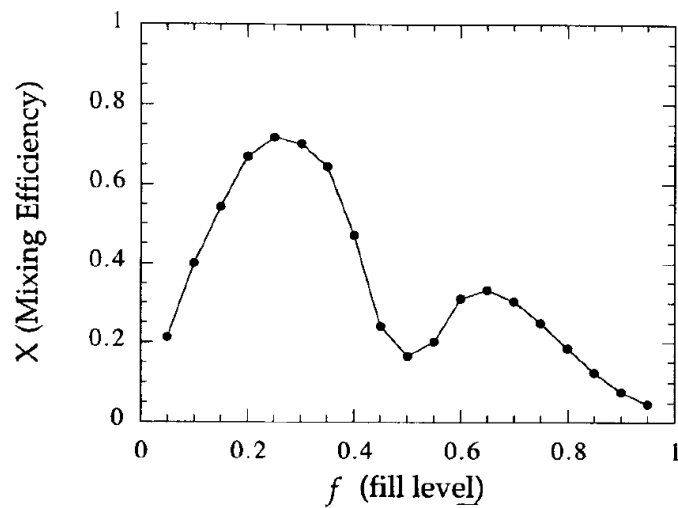


Fig. 3.7 Dependence of the mixing efficiency on the filling degree for simulations [109].

the core radius decreases by increasing the aspect ratio and by decreasing the filling degree and the wall roughness.

Although this thesis will essentially deal only with the above described phenomenology, i.e., radial/mixing segregation in rotating drums, it should be clarified that the migration problem in this geometric configuration is in fact much more complex. Indeed, axial mixing/segregation in rotating drums is an important and ample issue, much studied in the literature; we will however only give here a few examples on this problem.

Santomaso et al. [143] experimentally studied mixing in two cross-section regimes, rolling and cataracting, with two powders of different colours initially axially segregated, to understand how drum speed influences mixing efficiency. They observed that the cataracting regime improves the homogenization and the mixing rate over the rolling regime. They proved that cataracting prevents the formation of segregation patterns, and that this regime destroys axial convective fluxes responsible for the formation of a bulk core. A diffusive mechanism is demonstrated to fit properly the mixing during cataracting flow.

Santomaso et al. [145] experimentally studied radial segregation driven by axial convection. They found a core of heavy particles also in the axial direction, with light particles occupying the zones of the granular bed near the two end-walls.

Taberlet et al. [157] and Taberlet et al. [158] compared experimental and DEM simulation results on the combination between axial and radial segregation in a rotating drum partially filled with a ternary mixture of beads of three sizes. In experiments, surface particle velocities are measured by particle tracking. In fig. 3.8 the experimental results for axial segregation patterns over time are showed; initially the large particles form an outer surface band, the medium ones constitute an internal band, and the smallest particles form a core (1-1.5 min, **a-b**). Subsequently, axial segregation occurs,

with transverse layers throughout the granular bed (2-2.5 min, **c-d**). Furthermore, while no significant jump was found in velocity and velocity gradient at interfaces in the radial direction, large jumps occur in the axial direction of the drum.

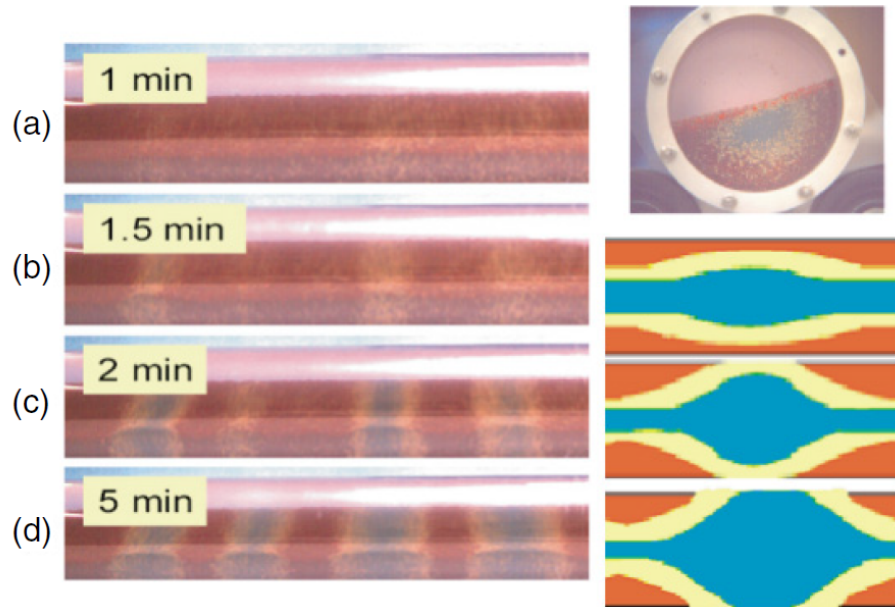


Fig. 3.8 On the left: Image sequence of ternary mixture of 0.6mm (blue), 1mm (yellow), and 2mm (red) particles. On the upper right: radial core on the end wall of the cylinder after 1 min of rotation; the smallest particles (blue) form a core in the centre with the medium sized (yellow) next out and the largest farthest out (red). On the lower right: schematic of an axial band evolving with time [158].

Finally, we mention that radial segregation is always faster than axial one; radial process is observed within several drum revolutions, while axial segregation evolves very slowly and usually takes several hundreds or even 10'000 cylinder revolutions [130, 164].

3.1.2 Numerical literature

DEM literature

Dury and Ristow [42] investigated with 3D discrete element method the dynamics of the size segregation process of binary mixtures differing in size in rotating drums,

operated in the continuous flow regime. They found that segregation is favoured by more than half-filled cylinder, as experimentally reported by Metcalfe et al. [113]. The authors reported that radial segregation occurs for any arbitrary small particle size difference. Interestingly, they found that, starting with initially separated granular phases, the light particles always maintain a geometrically connected shape, confirming experimental results by Pollard and Henein [130], Alonso et al. [4], Clément et al. [30], Cantelaube [25], Ristow and Nakagawa [138], Taberlet et al. [157].

In a second work the same authors, Dury and Ristow [43], studied again the radial segregation dynamics of a binary particle mixture in a three-dimensional cylinder using DEM. The size ratio of the two types of particles was fixed, while the density of the smaller particles was varied in order to see the interplay of size and density radial segregation. The initial configuration was set with an equal amount of smaller and large particle occupying the two cylinder halves divided by the cylinder symmetry plane. They found that if the smaller particles also have the higher density, the radial segregation process is enhanced. Instead, if the smaller particles have the lower density, the radial segregation is counterbalanced, supporting the experimental results by Jain et al. [73].

Yamane [167] also investigated radial size segregation in a rotating cylinder using DEM. After only few revolutions of the cylinder he found a central core of smaller particles surrounded by larger particles, confirming the results of [42]. Moreover, he found particle migration in axial direction.

Pereira et al. [126] used DEM and experiments to study the segregation of a binary mixture equal in size but of differing density granular material in an axially rotating cylinder. The agreement between simulation and experimental results was very good. The final asymptotic state is found to be independent of the initial segregation state of

the particles: a segregation core of heavy particles is formed, as in the experimental results of Alonso et al. [4], Khakhar et al. [86, 85], and McCarthy et al. [108].

Xu et al. [166] studied mixing in a rotating drum by both 2D DEM simulations and experiments. They explored the dependence on both physical properties, i.e. density or friction, and geometrical properties on mixing process. The authors highlighted that particle density and size are the dominating factors in the segregation dynamic, while the effect of frictional coefficient is little influencing. In fig. 3.9 are showed simulative results for size segregation; the authors found that greater particles form an inside core. These results significantly different from the experiment of Pollard and Henein [130], Alonso et al. [4], Clément et al. [30], Cantelaube [25], Ristow and Nakagawa [138], Taberlet et al. [157] and the DEM simulations of Dury and Ristow [42] and Yamane [167], but consistent with the results of Wightman and Muzzio [164]. The authors do not understand the reason of this disagreement, but an explanation could perhaps be found trough to observed dependence on angular velocity reported by Nityanand et al. [117].

Fig. 3.10 show the radial segregation for particles differing in density, with a core of denser particles (blue), in agreement with the results of Alonso et al. [4], Khakhar et al. [86, 85], Pereira et al. [126], and McCarthy et al. [108]. DEM radial segregation results for particles differing in size and density shows a segregated core of smaller particles, if these ones have the greater density and instead, a better homogenization if the bigger beads are denser (see. fig. 3.11), in agreement with the experimental results of Jain et al. [73].

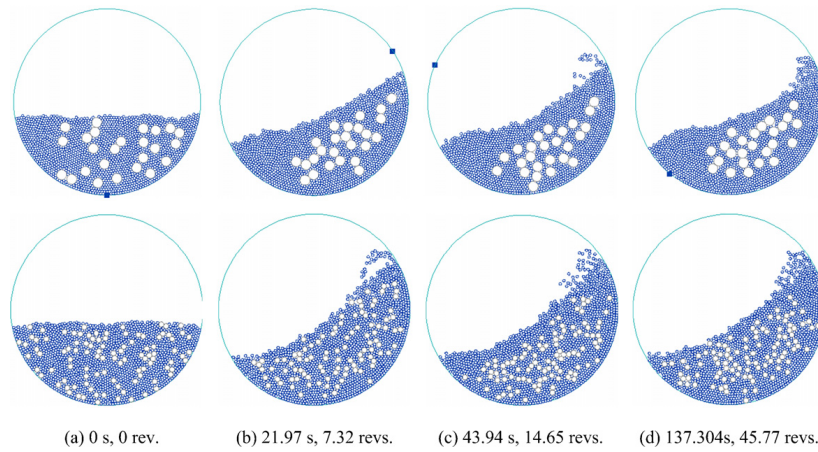


Fig. 3.9 Simulated mixing patterns at different time instants: 1st row, size ratio 4:1; 2nd row, size ratio 2:1 [166].

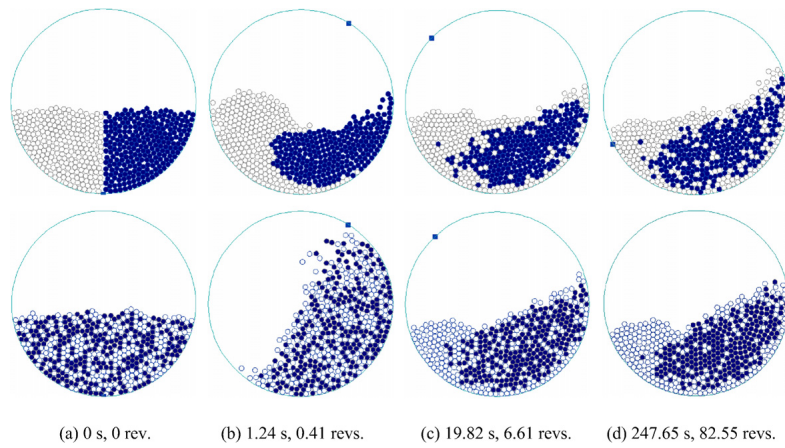


Fig. 3.10 DEM radial density segregation [166]. Blue particles are the denser and form an inside core.

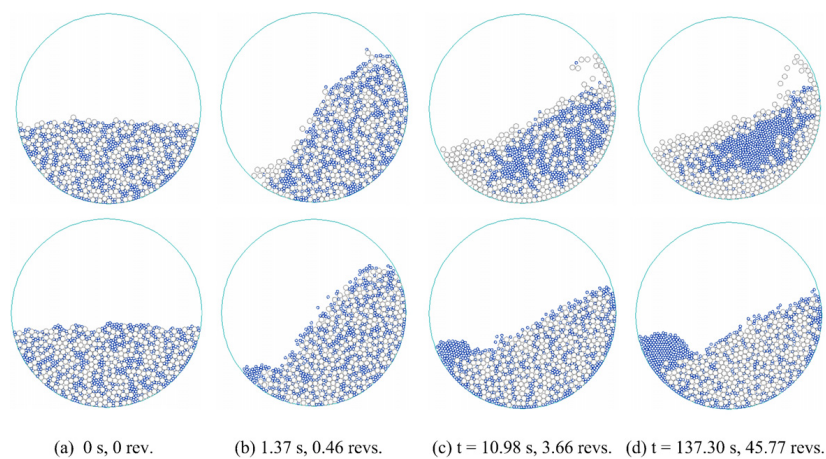


Fig. 3.11 DEM radial segregation results for particles differing in size and density, smaller/bigger particles have the higher density in the first/second row [166].

CFD literature

While many numerical studies based on DEM have been made for the study of segregation in rotating drum cylinder, the continuum approach has been used in few studies.

Gray [63] compared experiments and theory for the quasi two-dimensional steady continuous motion of mono-disperse granular material in a rotating drum. In the theory the fluid-like avalanche is treated as a shallow incompressible Mohr-Coulomb or inviscid material sliding on a moving bed at which there is erosion and deposition. The solid is treated as a rigid rotating body, and the two regions are coupled together using a mass jump condition. For their results see fig. 3.12; comparison between theory and experiments is very good for high filling degree, to slightly deteriorate for low filling degree.

Huang et al. [69] and Huang and Kuo [70] used Eulerian continuum approach using the constitutive equation from kinetic theory of granular matter. They found a core of small particles and two side “wings” not far from the end walls of the cylinder (fig. 3.13). The formation of radial segregation core and axial segregation bands qualitatively agree with the experimental observations. They used three kinetic models: Syamlal–O’Brien model [104], Gidaspow model Gidaspow [58], and DARF model Huang et al. [69]. Their results are very dependent from the adopted model.

He et al. [65] simulated segregation of binary mixtures in a rotating drum using the Eulerian based continuum model. The authors reported that small particles tend to concentrate in the core region, while large particles tend to occupy the outer region, consistent with experimental observations [130, 4, 30, 25, 138, 157]. Starting with a homogenous mixture the authors reported a radial segregation fully developed within 2.56 drum revolutions, which is consistent with experimental observations [130, 164].

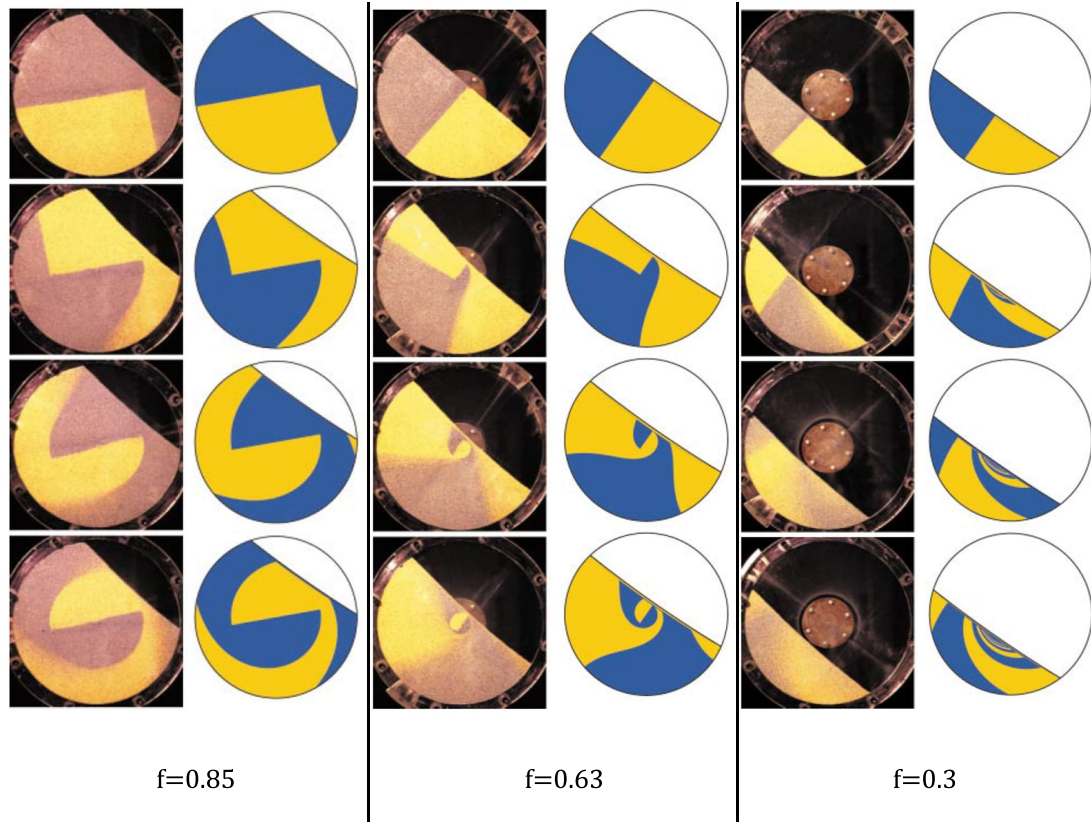


Fig. 3.12 Experimental and simulative results for different filling degree over time [63].

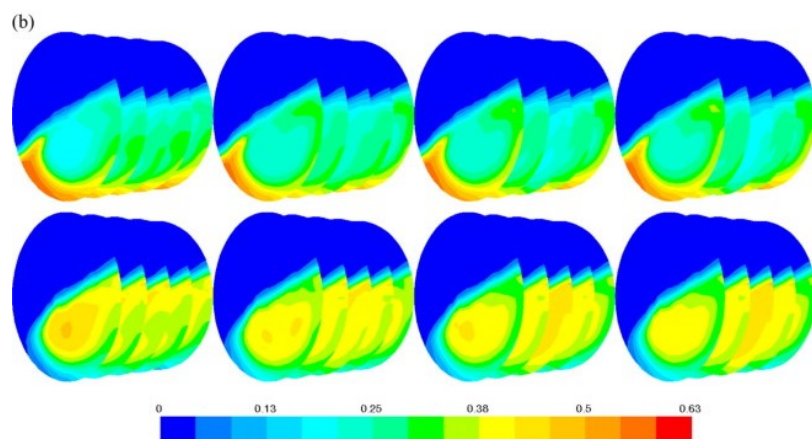


Fig. 3.13 Axial and radial segregation by Eulerian continuum approach. Volume fraction of the particulate phase of the greater particles (top row) the smaller particles (bottom row) at $t = 3, 5, 10, 20$ s (from left to right) [70].

Ding et al. [37] used PEPT and a two-dimensional mathematical model based on the Eulerian approach and the thin layer approximation to capture solid motion and concentration distribution of grains differing in diameter. Small particles are reported to concentrate in the core region, whereas large particles tend to occupy the shell region, in good agreement with their model predictions and the other experiments in literature. The axial particle mobility increases with drum rotational speed, the mutual diffusivity of small particles is higher than that of large particles.

3.2 Governing equations

We solved numerically granular flow of bi-disperse, cohesionless and dry grains inside a rotating cylinder, the remaining space, not occupied by the grains, is filled by air.

For our first goal, we focused on simulations of two granular phases differing only in colour as in Metcalfe et al. [113], whose experimental results are going to be compared with our predictions.

The following simulations will deal with density segregation experimentally observed by Alonso et al. [4], Khakhar et al. [86, 85], and McCarthy et al. [108]. Finally, we investigate some features of axial segregation.

Equations for the mass balance and the momentum balance with the adoption of the JFP constitutive equation are solved with the Volume of Fluid (VoF) approach as for the mono-disperse case. In this case we have two volume fractions α_{g1} and α_{g2} , representing the fractions occupied in each control volume by the granular phase “1” or “2” respectively. Hence, the governing equations for the mixture are very similar to the mono-disperse ones:

$$\nabla \cdot \mathbf{u} = 0 \tag{3.1}$$

$$\frac{\partial \rho \mathbf{u}}{\partial t} + \nabla \cdot (\rho \mathbf{u} \mathbf{u}) = -\nabla p + \nabla \cdot \boldsymbol{\tau} + \rho \mathbf{g} \tag{3.2}$$

3.2 Governing equations

where ρ, p, \mathbf{u} , and $\boldsymbol{\tau}$ are the density, pressure, velocity, and the shear stress of the single whole fluid, \mathbf{g} is the gravity, and t is the time.

$$\frac{\partial \alpha_{g1}}{\partial t} + \nabla \cdot (\alpha_{g1} \mathbf{u}) = 0 \quad (3.3)$$

$$\frac{\partial \alpha_{g2}}{\partial t} + \nabla \cdot (\alpha_{g2} \mathbf{u}) = 0 \quad (3.4)$$

The volume fraction α_{gi} ranges from 0 to 1 (granular phase “ i ” only). The interface between any two phases is postulated to be at $\alpha_{gi} = 0.5$.

The density and the viscosity of the overall fluid are:

$$\rho = \alpha_{g1} \rho_{g1} + \alpha_{g2} \rho_{g2} + (1 - \alpha_{g1} - \alpha_{g2}) \rho_{air} \quad (3.5)$$

$$\eta = \alpha_{g1} \eta_{g1}(II_{\mathbf{D}}, p) + \alpha_{g2} \eta_{g2}(II_{\mathbf{D}}, p) + (1 - \alpha_{g1} - \alpha_{g2}) \eta_{air} \quad (3.6)$$

All the phases are assumed to be incompressible. Thus, the packing factor of the grains ($\phi_i = \rho_{gi}/\rho$) is constant, fixed to 0.6 in all our calculations as in Jop et al. [78, 79].

In eq. 3.2 $\boldsymbol{\tau}$ is:

$$\boldsymbol{\tau} = 2\eta \mathbf{D} \quad (3.7)$$

In eq. 3.6.b η_{gi} are given by JFP model:

$$\eta_{g1} = \left(\mu_{s1} + \frac{\mu_{21} - \mu_{s2}}{1 + I_0/I} \right) \frac{p}{II_{\mathbf{D}}} = \mu_1(I) \frac{p}{II_{\mathbf{D}}} \quad (3.8)$$

$$\eta_{g2} = \left(\mu_{s2} + \frac{\mu_{22} - \mu_{s2}}{1 + I_0/I} \right) \frac{p}{II_{\mathbf{D}}} = \mu_2(I) \frac{p}{II_{\mathbf{D}}} \quad (3.9)$$

When the particles differ only in colour, in the simulation will be $\mu_s = \mu_{s1} = \mu_{s2}$ and $\mu_2 = \mu_{21} = \mu_{22}$, and so $\mu(I) = \mu_1(I) = \mu_2(I)$ and $\eta_g = \eta_{g1} = \eta_{g2}$.

Boundary conditions

Unlike the mono-disperse case, for which we have studied a fully three-dimensional problem, while for the bi-disperse granular media, different only in colour or different only in density, we perform 2D-simulations. The other boundary conditions are the same used in the 3D-case.

For boundary conditions used in the study of axial segregation, a 3D problem, we refer to the section 2.2.

On walls we choose a no-slip boundary condition that means:

$$\mathbf{u} = \boldsymbol{\Omega} \times \mathbf{r} \quad (3.10)$$

where $\boldsymbol{\Omega}$ is the angular velocity vector and \mathbf{r} is radial position vector.

The boundary condition for α_{gi} at walls is a zero gradient condition:

$$\nabla \alpha_{g1} \cdot \mathbf{n}_w = 0 \quad (3.11)$$

$$\nabla \alpha_{g2} \cdot \mathbf{n}_w = 0 \quad (3.12)$$

where \mathbf{n}_w is the normal to the walls.

This is a standard α_{gi} boundary condition of the solver that we have used to solve the equations above.

For the numerical method see section 2.3.

Table 3.1 Parameters used in our simulations for the bi-disperse case

	Ω [rad/s]	f [%]	d_p [mm]	$\rho_{p1} - \rho_{p2}[\frac{g}{m^3}]$	D [cm]	W [cm]	μ_s	μ_2
A	1.5	20, 40, 80	0.6	2.46	14.4	-	0.4	0.64
B	1.5, 7.5	60	0.6	2.46-1.23	14.4	-	0.4	0.64
C	1.5, 7.5	60	0.6	2.46-1.23	14.4	14.4	0.4	0.64

3.3 Results

3.3.1 Mixing of particles of two different colour

Our first aim was to study the segregation patterns of a bi-disperse mixture where the particles differ only in colour as the experiments of Metcalfe et al. [113].

The parameters used in our simulation are reported in row “A” of tab. 3.1.

The authors did not report the rotational velocity of their experiments, so we performed our simulation at different drum speed and we are going to show predictions for the rotational velocity that best matched experiments. This choice is in agreement with the velocity value used by Liu et al. [98] in a DEM similar study.

For μ_s and μ_2 we used parameters of Jop et al. [78, 79], since such material parameters are not available for the salt cubes used by Metcalfe et al. [113].

The experiments are shown until two revolutions, while we study the mixing process until 6 rev.

In the following simulations we have adopted a mesh of 17153 elements and a Co number equal to 0.06, as results of spatial and temporal convergences respectively.

In fig. 3.14 there is the initial setting in our simulation for 0.2 filling degree, for the other fills the setup is the same. The initial configuration starts from two completely segregated granular phases.

When the filling degree is low, already after 2 revolutions, we can see a complete homogenization in our simulation as in the experiment, see fig. 3.15.a. When the filling

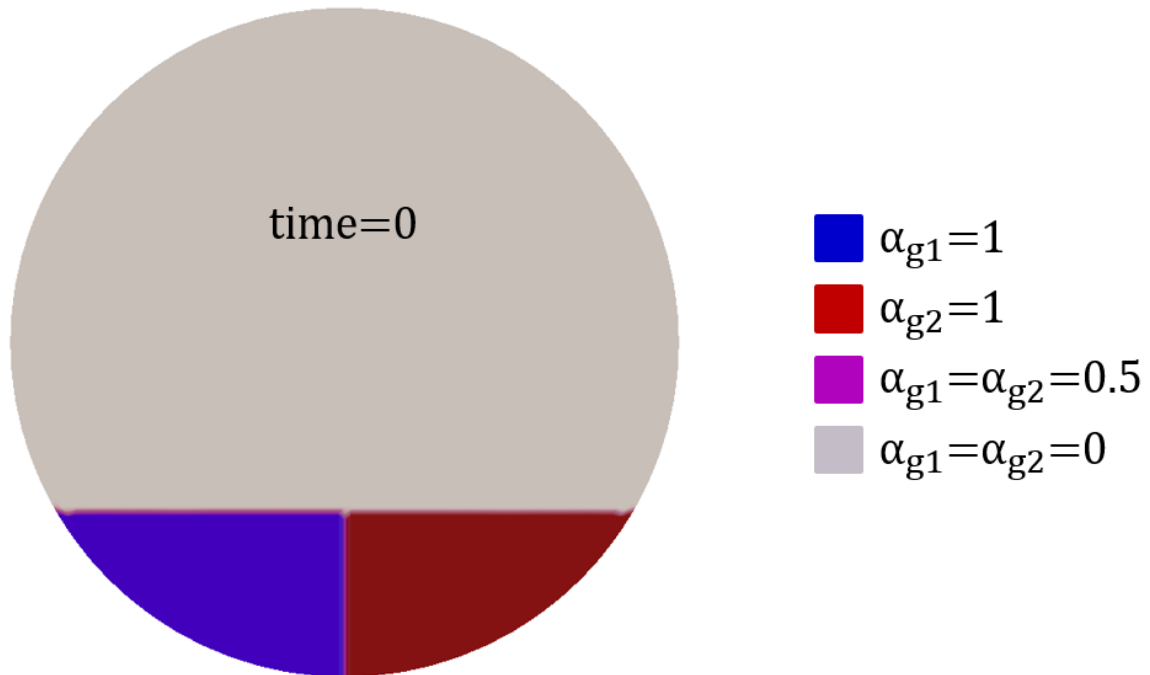


Fig. 3.14 Initial configuration for mixing simulations (0.2 filling degree). Blue colour stands for granular phase “1”, red for “2”, the violet is used when α_{g1} and/or α_{g2} are equal to 0.5.

is increased to 40%, the formation of a core appears, which becomes very pronounced when the fill is further increased to 80% (fig. 3.15.b and .c). Our results are in qualitative agreement with the experimental ones and are very promising.

The misalignment of the inclination of the free surface was to be expected, it is due to the inadequate μ_s and μ_2 adopted in our simulations; these values are measured for glass beads and not for salt used in the experiment of Metcalfe et al. [113]. In fact, we remember that μ_s and μ_2 are the physical parameters linked to the inclination of the free-surface.

We have prolonged the simulation until 6 revolutions to see the patterns evolutions and to study the time influence on mixing, the results are shown in fig. 3.16; for 40% the formation of a “red” core (phase 2) is clear, while for 80% the two phases are still highly segregated and a homogenization is far to be seen.

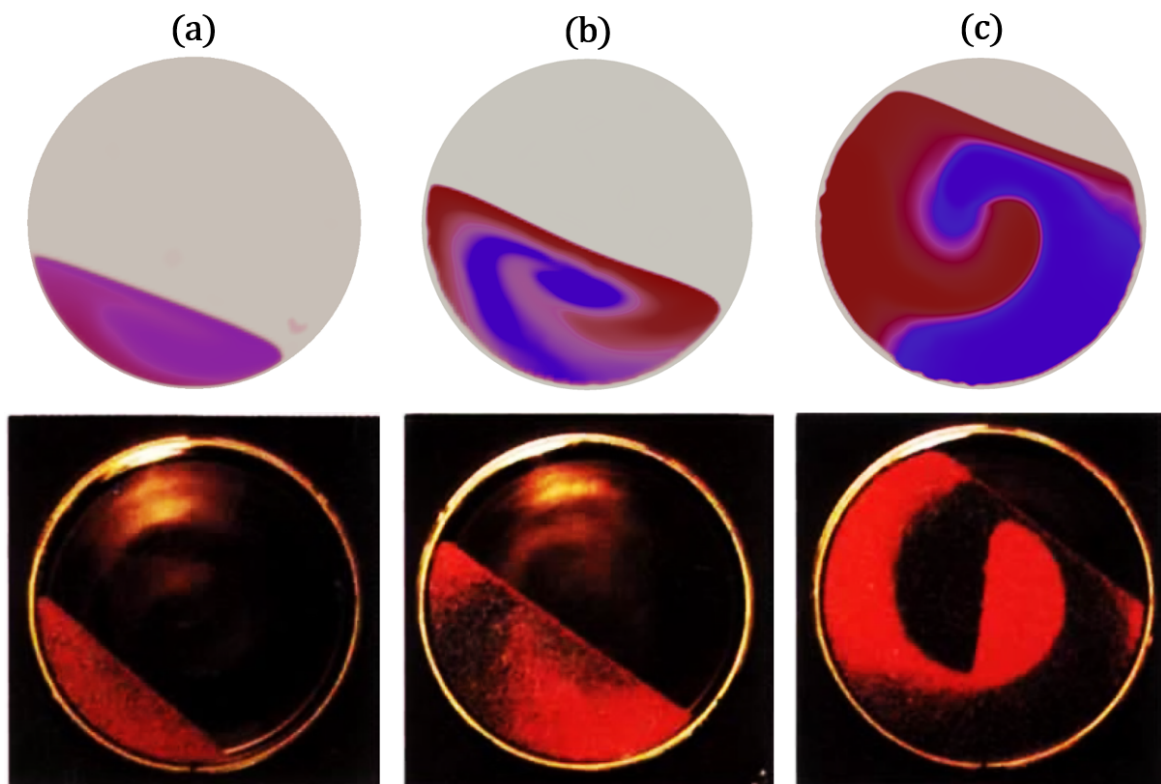


Fig. 3.15 Comparison between our predictions and experiments about segregation patterns after 2 rev. **a**: 20%, **a**: 40% and **c**: 80%.

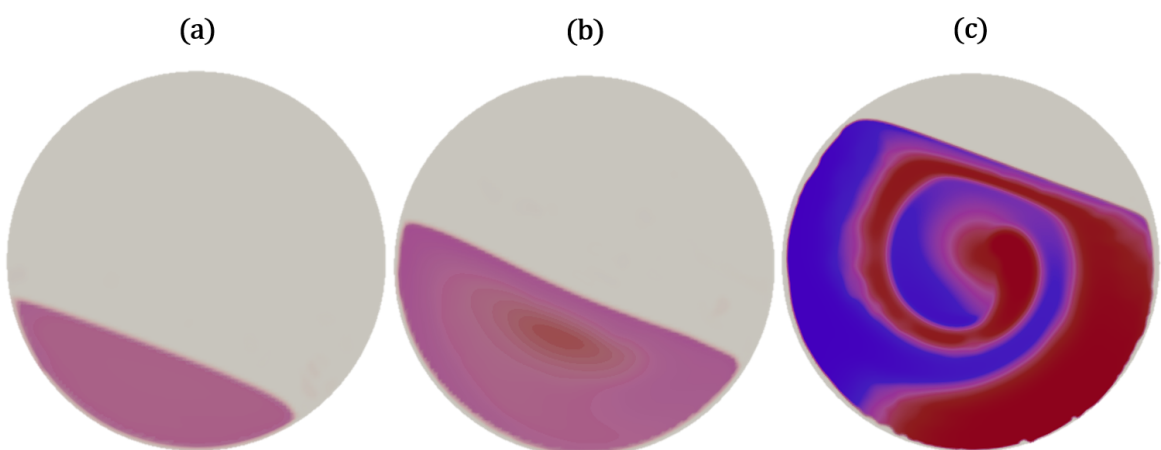


Fig. 3.16 Segregation patterns after 6 revolutions for our simulations. **a**: 20%, **a**: 40% and **c**: 80%.

The differences between simulations and experiments can be addressed also to the different predicted regime; adopting parameters for glass beads and such rotational velocity, we capture a rolling regime, while Metcalfe et al. [113] observed a slumping one. In fact, as we can see from fig. 3.15 the predicted flowing layer is greater than the experimental one and this lead to a smaller core.

The effect of cubic particles, instead of round ones taken into account in the model, should not be forgotten; round grains tend to roll easier than irregular particles which make a stronger structure, able to limit the relative movement among particles. So in our simulations we have studied a material “weaker” than that used in experiments of Metcalfe et al. [113].

However, as done by Metcalfe et al. [113], we can conclude that fillings up to 50% hinder mixing and lead to segregation and core formation.

3.3.2 2D Density segregation

In this section our aim is to predict the experimental observations of Alonso et al. [4], Khakhar et al. [86, 85], and McCarthy et al. [108], where heavier particles form a core surrounded by lighter ones.

In order to obtain this result we have halved the density of the granular phase “2” from the previous case. The parameters used in our simulations for the bi-disperse case with density difference are reported in row “B” of tab. 3.1.

The parameters μ_s and μ_2 are the same used in the previous case.

Also the mesh, with 17153 elements, and the Co number, equal to 0.06, are the same.

Since we want to observe the formation of an inside core, and low filling degree ensures the mixing, while high filling requires several revolutions for the mixing process, as shown above, we choose to study intermediate filling level (0.6).

The simulations are conducted until six revolutions as before.

We study the problem for the same velocity of the previous case, 1.5 rad/s, and for an additional rotational velocity five times bigger (7.5 rad/s).

In fig. 3.17 there is the initial setting in our simulation for 0.6 filling degree. As it can be seen by the figure the heavy particles are on the left (blue phase) and the light ones on the right (red phase). The initial configuration starts from two completely segregated granular phases.

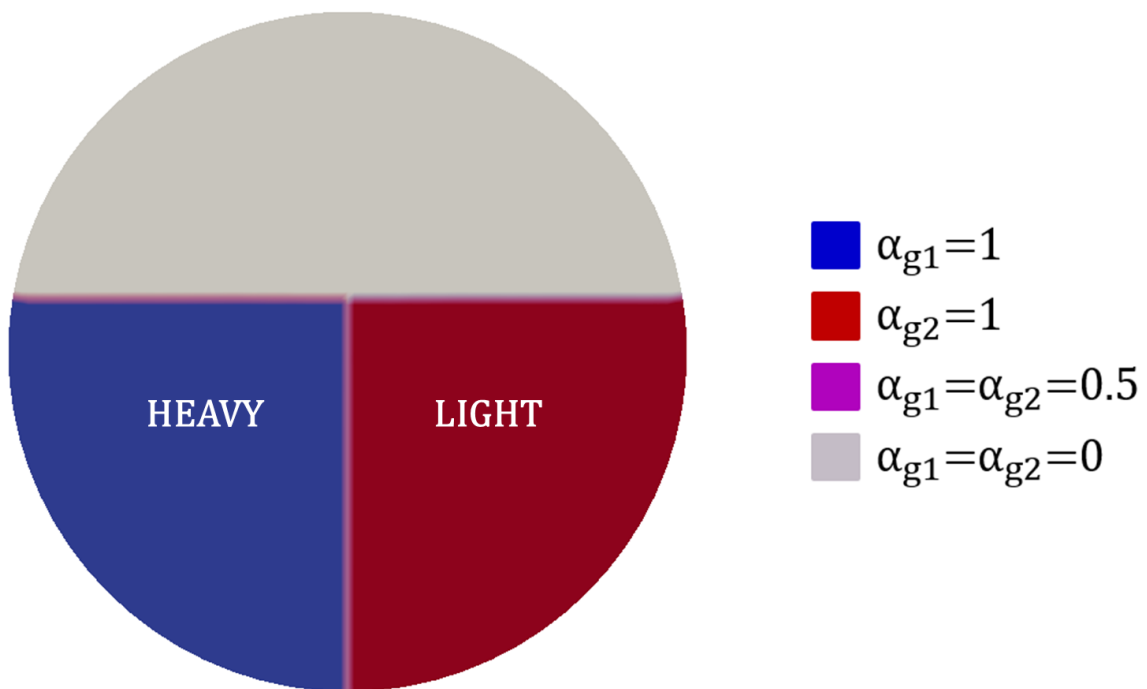


Fig. 3.17 Initial configuration for mixing simulations (0.6 filling degree). Blue colour stands for the heavy granular phase “1”, red for the light phase “2”, the violet is used when α_{g1} and/or α_{g2} are equal to 0.5.

In fig. 3.18 the configuration after six revolutions is shown. We can observe the formation of an inside core made of denser particles confirming the experimental results of Alonso et al. [4], Khakhar et al. [86, 85], and McCarthy et al. [108] and the DEM results by Xu et al. [166]. The formation of a core is already visible (if barely) after

two revolutions only. After 6 revolutions, on the other hand, the formation of a large segregated inside core is apparent.

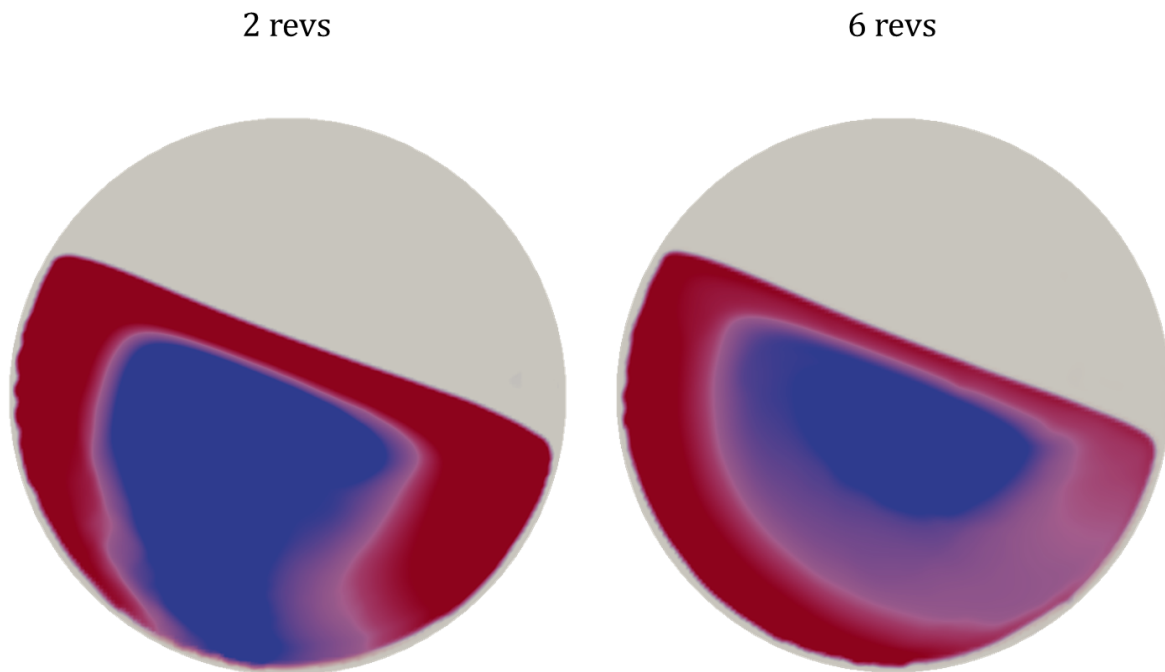


Fig. 3.18 Configuration for 1.5 rad/s after 2 and 6 revolutions. Heavy granular phase in blue.

A second simulation is also run to identify the possible influence of the rotational velocity.

Simulations at the velocity of 7.5 rad/s predict the cascading regimes instead of the rolling one showed in all the earlier cases, see fig. 3.19. The segregation process is now much faster, as it can be seen by comparing the fig. 3.18 and 3.19 after 2 revolutions only. Conversely, after 6 revolution the homogenization for the faster rotation is much better than for the rolling regime. This evidence, in fact, confirms the experimental results about the velocity effects by Xu et al. [166] and Santomaso et al. [143].

The reason of this better homogenization at higher speed can be explained considering the bigger thickness of the flowing layer at higher angular velocity [48].

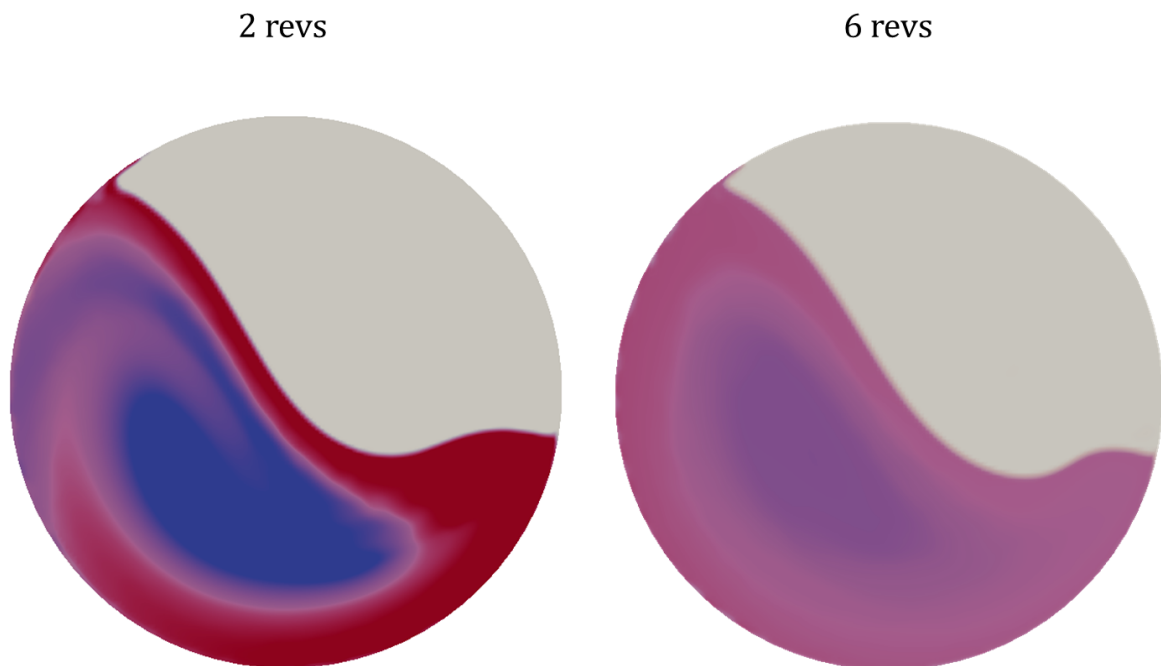


Fig. 3.19 Configuration for 7.5 rad/s after 2 and 6 revolutions. Heavy granular phase in blue.

3.3.3 3D Density segregation

The ultimate goal is to predict the axial segregation due to density difference.

In this case we performed 3D simulations.

The parameters adopted are reported in row “C” of tab. 3.1, the values are the same of row “B”, except the addition of cylinder width equal to diameter.

For the initial setting of our simulation see fig. 3.17.

The simulations are conducted until three revolutions in this case.

The fig. 3.20 shows the evolution patterns for 1.5 rad/s at different axial coordinates. As we can see, our simulations show a core of heavy granular material which decreases getting closer to the end-wall. After 2 revolutions this core disappears near the end-wall, the light particles enclose completely the denser core.

Our simulation results confirm the experimental evidence of Santomaso et al. [145], who reported the formation of a core made of denser particles for a bi-disperse case of equal-sized beads.

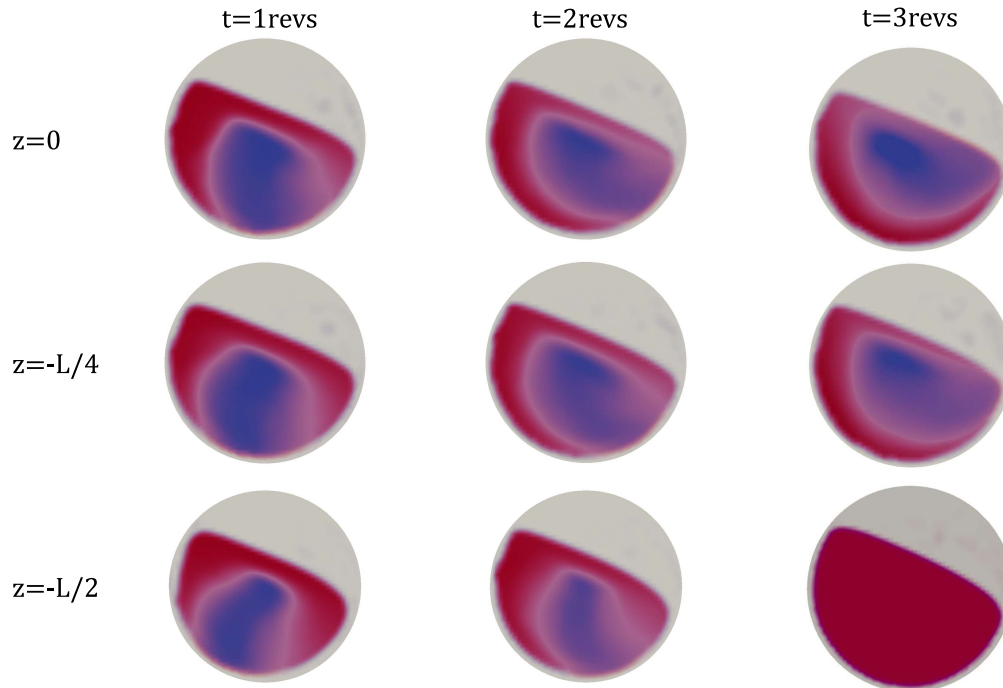


Fig. 3.20 Configuration for 1.5 rad/s at $z=0$ (on the symmetry plane), $z=-W/4$, $z=W/2$ (on the end-wall) after 1, 2 and 3 revolutions. Heavy granular phase in blue.

We have also studied the influence of the rotational velocity on axial segregation patterns; in fig. 3.21 the segregation pattern over time at different axial positions for 7.5 rad/s is reported.

The first evidence is that axial components of the velocity enhance mixing as we can see from the comparison of the fig. 3.21 for $z=0$, $t=2\text{revs}$ and the fig. 3.19; the homogenization is better for the 3D case.

As we can see from the fig. 3.21 the evolution patterns are very complex at high rotational velocity; the blue core of heavy particles is bigger in size and in volume

fraction value at an intermediate position between the symmetry plane and the end-wall ($z=-0.035\text{m}$) at any time. The core has almost vanished at the symmetry plane and at the end-wall for $t=2\text{revs}$, while it is still distinguishable for $z=-0.035\text{m}$.

This very particular segregation pattern can be observed in fig. 3.22, which represents a 3D contour for $\alpha_{heavy} = 0.7$. There are two cores, one very small near the symmetry plane and another at an intermediate position between the symmetry plane and the end-wall, in the proximity of the end wall there are only light particles.

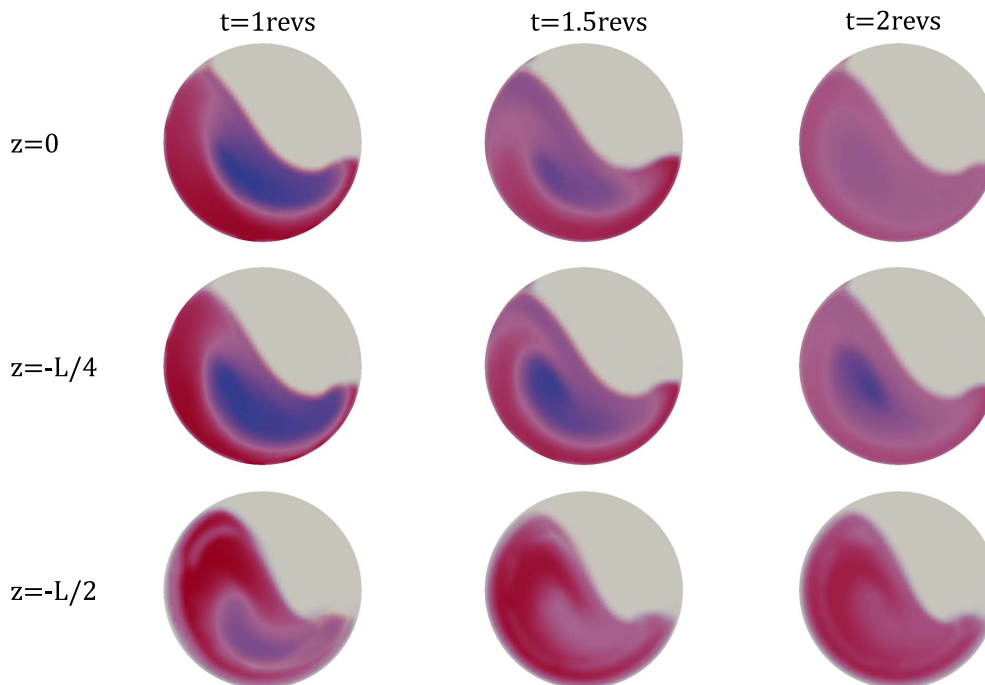


Fig. 3.21 Configuration for 7.5 rad/s at $z=0$ (on the symmetry plane), $z=-W/4$, $z=W/2$ (on the end-wall) after 1, 1.5 and 2 revolutions. Heavy granular phase in blue.

To the best of our knowledge, these complex segregation patterns have not been observed for particles differing in density, in fact reconstructing particle positions and trajectories inside the entire granular bed over time, for long cylinder, is very difficult by means of experiments.

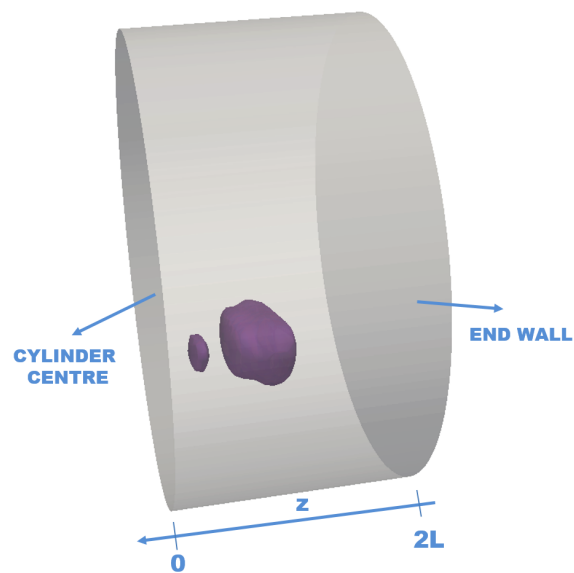


Fig. 3.22 Cores formation of heavy particles for 7.5 rad/s after 2 revolutions. It represents a 3D contour for $\alpha_{heavy} = 0.7$

Chapter 4

Conclusions and future perspectives

In this work we have studied, by means of 3D CFD numerical simulations, the flow of dry, mono-disperse granular materials in rotating cylinders, at various angular velocities, with different filling levels and glass bead sizes, and the bi-disperse granular flow of grains different only in colour or different only in density.

The granular material is modelled as a continuum fluid by adopting the visco-plastic Jop-Forsterre-Pouliquen constitutive model [79]. All the constitutive parameters in JFP equation have been identified from independent data, also derived in geometries different from that of drums. The $\mu(I)$ -rheology is then introduced without resorting to adjustable parameters.

As we have reviewed in sections 2.1 and 3.1, most published research works proposed numerical models which require adjustable parameters, and/or studied 2D problems, despite the proven influence of side-walls [78, 129].

The importance of the third dimension is confirmed by our simulations, which give the first quantitative agreement with stream-wise velocity measurements reported in literature Pohlman et al. [129]. Moreover, our 3D simulations have shown very

complex three dimensional patterns for bi-disperse systems with particles differing only in density. It would be quite important to compare this prediction with actual experimental result.

Overall, our simulation results provide a substantial validation of JFP model in complex 3D geometry, and capture the succession of flow regimes categorized by Mellmann [111], i.e., slumping, rolling, cascading, cataracting, and centrifuging.

Most studies reported in literature focused mainly on rolling regime because it is characterized by a stable and flat surface of flowing layer, this feature makes experiments much more simple [143, 20, 2, 141]. Also some models reported in literature require this simplification [19, 86, 38, 121, 141]. This thesis overcomes this limit.

In this work the first prediction of slumping regime through continuum modelling is reported, and complex segregation patterns, never before observed by means of experiments or simulations, are showed.

The results for mono-disperse case are compared with experimental data by Santos et al. [146], Balmforth and McElwaine [11], Ding et al. [38] and Pohlman et al. [129].

We refer to the observations of Alonso et al. [4], Khakhar et al. [86, 85], McCarthy et al. [108], Santomaso et al. [143, 145] and Xu et al. [166] for the bi-disperse one.

The agreement is quantitative in most cases, and thus supports the use of continuum mechanics to describe granular dense flows.

In particular, the adoption of JFP constitutive model proves to be very effective in a wide range of parameter values. Indeed, free-surface shape, superficial velocity and velocity within the granular bed are predicted in amazing detail.

These results show the great capabilities of our numerical approach to capture fine details, e.g., transitions between different flow regimes, which are quite difficult to be accessed through experiments, and which are not predictable through DEM simulation for large cylinders with billion of particles.

Our next purpose is to study the influence of μ_s and μ_2 on the segregation patterns, matching quantitatively the experimental results of Metcalfe et al. [113].

Moreover, we want to study the mixing process of a mixture constituted of two or more kind of grains differing in size or density or their interplay, comparing our results with experiments reported in literature [139, 130, 4, 30, 138, 157, 37, 164, 86, 85, 108, 120, 73].

It is a question of future research investigate the third dimension more in detail. A closer look to experimental and numerical literature on axial mixing, reveals a number of contradictory evidence and little known aspects [151, 138, 43, 135, 167, 157, 142, 143, 145, 51, 158, 126, 1, 144, 3, 70].

A point which needs further investigations is the study of wall boundary conditions [7, 6]. Here, a simple no-slip condition has been adopted, while a wide variety of behaviours has been reported for granular materials near walls [131, 23, 56].

Another important improvement could be the implementation of a variable packing factor [14], which would allow to study regimes where the gas behaviour is experienced, e.g. like in the cataracting regime.

References

- [1] Aissa, A. A., Duchesne, C., and Rodrigue, D. (2011). Effect of friction coefficient and density on mixing particles in the rolling regime. *Powder Technology*, 212(2):340–347.
- [2] Alexander, A., Shinbrot, T., and Muzzio, F. J. (2002). Scaling surface velocities in rotating cylinders as a function of vessel radius, rotation rate, and particle size. *Powder Technology*, 126(2):174–190.
- [3] Alizadeh, E., Bertrand, F., and Chaouki, J. (2013). Comparison of DEM results and lagrangian experimental data for the flow and mixing of granules in a rotating drum. *AIChE Journal*, 60(1):60–75.
- [4] Alonso, M., Satoh, M., and Miyanami, K. (1991). Optimum combination of size ratio, density ratio and concentration to minimize free surface segregation. *Powder Technology*, 68(2):145–152.
- [5] Andreotti, B., Forterre, Y., and Pouliquen, O. (2013). *Granular media: between fluid and solid*. Cambridge University Press.
- [6] Artoni, R., Andrea, C. S., Go', M., and Canu, P. (2012). Scaling laws for the slip velocity in dense granular flows. *Physical Review Letters*, 108(23).
- [7] Artoni, R., Santomaso, A., and Canu, P. (2009a). Effective boundary conditions for dense granular flows. *Physical Review E*, 79(3).
- [8] Artoni, R., Santomaso, A., and Canu, P. (2009b). Simulation of dense granular flows: Dynamics of wall stress in silos. *Chemical Engineering Science*, 64(18):4040–4050.
- [9] Artoni, R., Zugliano, A., Primavera, A., Canu, P., and Santomaso, A. (2011). Simulation of dense granular flows: Comparison with experiments. *Chemical Engineering Science*, 66(3):548–557.
- [10] Bagnold, R. A. (1954). Experiments on a gravity-free dispersion of large solid spheres in a Newtonian fluid under shear. *Proceedings of the Royal Society of London A*, 225(1160):49–63.
- [11] Balmforth, N. J. and McElwaine, J. N. (2018). From episodic avalanching to continuous flow in a granular drum. *Granular Matter*, 20(3).
- [12] Baran, O., Ertas, D., Halsey, T. C., Grest, G. S., and Lechman, J. B. (2006). Velocity correlations in dense gravity-driven granular chute flow. *Physical Review E*, 74(5).

-
- [13] Bardenhagen, S., Brackbill, J., and Sulsky, D. (2000). The material-point method for granular materials. *Computer Methods in Applied Mechanics and Engineering*, 187(3-4):529–541.
- [14] Barker, T., Schaeffer, D. G., Shearer, M., and Gray, J. M. N. T. (2017). Well-posed continuum equations for granular flow with compressibility and (i)-rheology. *Proceedings of the Royal Society A: Mathematical, Physical and Engineering Sciences*, 473(2201):20160846.
- [15] Baumgarten, A. S. and Kamrin, K. (2018). A general fluid–sediment mixture model and constitutive theory validated in many flow regimes. *Journal of Fluid Mechanics*, 861:721–764.
- [16] Bennani, L., Neau, H., Baudry, C., Laviéville, J., Fede, P., and Simonin, O. (2017). Numerical simulation of unsteady dense granular flows with rotating geometries. *Chemical Engineering Research and Design*, 120:333–347.
- [17] Berberović, E., van Hinsberg, N. P., Jakirlić, S., Roisman, I. V., and Tropea, C. (2009). Drop impact onto a liquid layer of finite thickness: Dynamics of the cavity evolution. *Physical Review E*, 79(3):036306.
- [18] Berzi, D. (2014). Extended kinetic theory applied to dense, granular, simple shear flows. *Acta Mechanica*, 225(8):2191–2198.
- [19] Boateng, A. and Barr, P. (1996). Modelling of particle mixing and segregation in the transverse plane of a rotary kiln. *Chemical Engineering Science*, 51(17):4167–4181.
- [20] Boateng, A. A. and Barr, P. V. (1997). Granular flow behaviour in the transverse plane of a partially filled rotating cylinder. *Journal of Fluid Mechanics*, 330:233–249.
- [21] Bocquet, L., Colin, A., and Ajdari, A. (2009). Kinetic theory of plastic flow in soft glassy materials. *Physical Review Letters*, 103(3).
- [22] Bouzid, M., Trulsson, M., Claudin, P., Clément, E., and Andreotti, B. (2013). Nonlocal rheology of granular flows across yield conditions. *Physical Review Letters*, 111(23).
- [23] Buchholtz, V., Pöschel, T., and Tillemans, H. J. (1995). Simulation of rotating drum experiments using non-circular particles. *Physica A: Statistical Mechanics and its Applications*, 216(3):199–212.
- [24] Campbell, C. S. (1990). Rapid granular flows. *Annual Review of Fluid Mechanics*, 22(1):57–90.
- [25] Cantelaube, F. (1995). *Ph.D. Thesis*. PhD thesis, University of Rennes I, France.
- [26] Capecelatro, J. and Desjardins, O. (2013). An Euler–Lagrange strategy for simulating particle-laden flows. *Journal of Computational Physics*, 238(2):1–31.
- [27] Chambon, G., Bouvarel, R., Laigle, D., and Naaim, M. (2011). Numerical simulations of granular free–surface flows using smoothed particle hydrodynamics. *Journal of Non–Newtonian Fluid Mechanics*, 166(12-13):698–712.

-
- [28] Chen, P., Ottino, J. M., and Lueptow, R. M. (2008). Subsurface granular flow in rotating tumblers: A detailed computational study. *Physical Review E*, 78(2).
- [29] Chen, Z.-P., Zhang, X., Qiu, X.-M., and Liu, Y. (2017). A frictional contact algorithm for implicit material point method. *Computer Methods in Applied Mechanics and Engineering*, 321:124–144.
- [30] Clément, E., Rajchenbach, J., and Duran, J. (1995). Mixing of a granular material in a bidimensional rotating drum. *Europhysics Letters (EPL)*, 30(1):7–12.
- [31] Coetzee, C. J. (2014). Discrete and continuum modelling of soil cutting. *Computational Particle Mechanics*, 1(4):409–423.
- [32] Cummins, S. and Brackbill, J. (2002). An implicit particle-in-cell method for granular materials. *Journal of Computational Physics*, 180(2):506–548.
- [33] da Cruz, F., Emam, S., Prochnow, M., Roux, J. N., and Chevoir, F. (2005). Rheophysics of dense granular materials: Discrete simulation of plane shear flows. *Physical Review E*, 72(2):021309.
- [34] Delele, M. A., Weigler, F., Franke, G., and Mellmann, J. (2016). Studying the solids and fluid flow behavior in rotary drums based on a multiphase CFD model. *Powder Technology*, 292:260–271.
- [35] Demagh, Y., Ben Moussa, H., Lachi, M., Noui, S., and Bordja, L. (2012). Surface particle motions in rotating cylinders: Validation and similarity for an industrial scale kiln. *Powder Technology*, 224(4):260–272.
- [36] Deshpande, S. S., Anumolu, L., and Trujillo, M. F. (2012). Evaluating the performance of the two-phase flow solver interFoam. *Computational Science & Discovery*, 5(1):014016.
- [37] Ding, Y., Forster, R., Seville, J., and Parker, D. (2002). Granular motion in rotating drums: bed turnover time and slumping–rolling transition. *Powder Technology*, 124(1-2):18–27.
- [38] Ding, Y. L., Seville, J. P. K., Forster, R., and Parker, D. J. (2001). Solids motion in rolling mode rotating drums operated at low to medium rotational speeds. *Chemical Engineering Science*, 56(5):1769–1780.
- [39] Dissanayake, S., Karunarathne, S., Lundberg, J., and Tokheim, L. A. (2017). CFD study of particle flow patterns in a rotating cylinder applying OpenFOAM and Fluent.
- [40] Drucker, D. C. and Prager, W. (1952). Soil mechanics and plastic analysis or limit design. *Quarterly of applied mathematics*, 10(2):157–165.
- [41] Dunatunga, S. and Kamrin, K. (2015). Continuum modelling and simulation of granular flows through their many phases. *Journal of Fluid Mechanics*, 779:483–513.
- [42] Dury, C. M. and Ristow, G. H. (1999a). Competition of mixing and segregation in rotating cylinders. *Physics of Fluids*, 11(6):1387–1394.

-
- [43] Dury, C. M. and Ristow, G. H. (1999b). Radial segregation through axial migration. *Europhysics Letters (EPL)*, 48(1):60–65.
- [44] Dury, C. M., Ristow, G. H., Moss, J. L., and Nakagawa, M. (1998). Boundary effects on the angle of repose in rotating cylinders. *Physical Review E*, 57(4):4491–4497.
- [45] Enright, D., Fedkiw, R., Ferziger, J., and Mitchell, I. (2002). A hybrid particle level set method for improved interface capturing. *Journal of Computational Physics*, 183(1):83–116.
- [46] Eslamian, A. and Khayat, M. (2017). A novel hybrid solid-like fluid-like (SLFL) method for the simulation of dry granular flows. *Particuology*, 31:200–219.
- [47] Fei, M., Sun, Q., Xu, X., Jin, F., and Zhou, G. G. (2016). Simulations of multi-states properties of granular materials based on non-linear granular elasticity and the MiDi rheological relation. *Powder Technology*, 301:1092–1102.
- [48] Félix, G., Falk, V., and D'Ortona, U. (2007). Granular flows in a rotating drum: the scaling law between velocity and thickness of the flow. *The European Physical Journal E*, 22(1):25–31.
- [49] Fern, E. J. and Soga, K. (2016). The role of constitutive models in MPM simulations of granular column collapses. *Acta Geotechnica*, 11(3):659–678.
- [50] Ferziger, J. H. and Perić, M. (2002). *Computational Methods for Fluid Dynamics*. Springer Berlin Heidelberg.
- [51] Finnie, G., Kruyt, N., Ye, M., Zeilstra, C., and Kuipers, J. (2005). Longitudinal and transverse mixing in rotary kilns: A discrete element method approach. *Chemical Engineering Science*, 60(15):4083–4091.
- [52] Forterre, Y. (2006). Kapiza waves as a test for three-dimensional granular flow rheology. *Journal of Fluid Mechanics*, 563:123.
- [53] Forterre, Y. and Pouliquen, O. (2003). Long-surface-wave instability in dense granular flows. *Journal of Fluid Mechanics*, 486:21–50.
- [54] Forterre, Y. and Pouliquen, O. (2008). Flows of dense granular media. *Annual Review of Fluid Mechanics*, 40(1):1–24.
- [55] Forterre, Y. and Pouliquen, O. (2018). Physics of particulate flows: From sand avalanche to active suspensions in plants. *Comptes Rendus Physique*, 19(5):271–284.
- [56] Fried, E., Shen, A. Q., and Thoroddsen, S. T. (1998). Wave patterns in a thin layer of sand within a rotating horizontal cylinder. *Physics of Fluids*, 10(1):10–12.
- [57] GDR MiDi (2004). On dense granular flows. *The European Physical Journal E*, 14(4):341–365.
- [58] Gidaspow, D. (1994). *Multiphase Flow and Fluidization: Continuum and Kinetic Theory Descriptions*. Academic Press.

-
- [59] Gingold, R. A. and Monaghan, J. J. (1977). Smoothed particle hydrodynamics: theory and application to non-spherical stars. *Monthly Notices of the Royal Astronomical Society*, 181(3):375–389.
- [60] Goddard, J. D. (2014). Continuum modeling of granular media. *Applied Mechanics Reviews*, 66(5).
- [61] Goldhirsch, I. (2003). Rapid granular flows. *Annual Review of Fluid Mechanics*, 35(1):267–293.
- [62] Govender, I. (2016). Granular flows in rotating drums: A rheological perspective. *Minerals Engineering*, 92:168–175.
- [63] Gray, J. M. N. T. (2001). Granular flow in partially filled slowly rotating drums. *Journal of Fluid Mechanics*, 441:1–29.
- [64] Haff, P. K. (1983). Grain flow as a fluid–mechanical phenomenon. *Journal of Fluid Mechanics*, 134:401.
- [65] He, Y., Chen, H., Ding, Y., and Lickiss, B. (2007). Solids motion and segregation of binary mixtures in a rotating drum mixer. *Chemical Engineering Research and Design*, 85(7):963–973.
- [66] Henann, D. L. and Kamrin, K. (2013). A predictive, size-dependent continuum model for dense granular flows. *Proceedings of the National Academy of Sciences*, 110(17):6730–6735.
- [67] Henann, D. L. and Kamrin, K. (2014). Continuum modeling of secondary rheology in dense granular materials. *Physical Review Letters*, 113(17).
- [68] Henann, D. L. and Kamrin, K. (2016). A finite element implementation of the nonlocal granular rheology. *International Journal for Numerical Methods in Engineering*, 108(4):273–302.
- [69] Huang, A.-N., Kao, W.-C., and Kuo, H.-P. (2013). Numerical studies of particle segregation in a rotating drum based on eulerian continuum approach. *Advanced Powder Technology*, 24(1):364–372.
- [70] Huang, A. N. and Kuo, H. P. (2017). CFD simulation of particle segregation in a rotating drum. Part I: eulerian solid phase kinetic viscosity. *Advanced Powder Technology*, 28(9):2094–2101.
- [71] Ionescu, L. R., Mangeney, A., Bouchut, F., and Roche, O. (2015). Viscoplastic modeling of granular column collapse with pressure-dependent rheology. *Journal of Non-Newtonian Fluid Mechanics*, 219:1–18.
- [72] Issa, R. I., Gosman, A. D., and Watkins, A. P. (1986). The computation of compressible and incompressible recirculating flows by a non-iterative implicit scheme. *Journal of Computational Physics*, 62(1):66–82.
- [73] Jain, N., Ottino, J. M., and Lueptow, R. M. (2005). Regimes of segregation and mixing in combined size and density granular systems: an experimental study. *Granular Matter*, 7(2-3):69–81.

-
- [74] Jenkins, J. T. and Berzi, D. (2010). Dense inclined flows of inelastic spheres: tests of an extension of kinetic theory. *Granular Matter*, 12(2):151–158.
- [75] Jian, Z., Josserand, C., Popinet, S., Ray, P., and Zaleski, S. (2018). Two mechanisms of droplet splashing on a solid substrate. *Journal of Fluid Mechanics*, 835:1065–1086.
- [76] Jiang, Y. and Liu, M. (2003). Granular elasticity without the coulomb condition. *Physical Review Letters*, 91(14).
- [77] Jiang, Y., Yang, T., and Chang, J. (2016). Solid deformation by material point method. *Communications in Information and Systems*, 16(3):127–146.
- [78] Jop, P., Forterre, Y., and Pouliquen, O. (2005). Crucial role of sidewalls in granular surface flows: consequences for the rheology. *Journal of Fluid Mechanics*, 541:167–192.
- [79] Jop, P., Forterre, Y., and Pouliquen, O. (2006). A constitutive law for dense granular flows. *Nature*, 441(7094):727–730.
- [80] Kamrin, K. (2010). Nonlinear elasto-plastic model for dense granular flow. *International Journal of Plasticity*, 26(2):167–188.
- [81] Kamrin, K. (2019). Non-locality in granular flow: Phenomenology and modeling approaches. *Frontiers in Physics*, 7.
- [82] Kamrin, K. and Henann, D. L. (2015). Nonlocal modeling of granular flows down inclines. *Soft Matter*, 11(1):179–185.
- [83] Kamrin, K. and Koval, G. (2012). Nonlocal constitutive relation for steady granular flow. *Physical Review Letters*, 108(17).
- [84] Karunaratne, S., Jayarathna, C., and Tokheim, L. (2016). Impact of particle diameter, particle density and degree of filling on the flow behavior of solid particle mixtures in a rotating drum. In *The 9th Eurosim Congress on Modelling and Simulation*, pages 955–960.
- [85] Khakhar, D. V., McCarthy, J. J., and Ottino, J. M. (1997a). Radial segregation of granular mixtures in rotating cylinders. *Physics of Fluids*, 9(12):3600–3614.
- [86] Khakhar, D. V., McCarthy, J. J., Shinbrot, T., and Ottino, J. M. (1997b). Transverse flow and mixing of granular materials in a rotating cylinder. *Physics of Fluids*, 9(1):31.
- [87] Komatsu, T. S., Inagaki, S., Nakagawa, N., and Nasuno, S. (2001). Creep motion in a granular pile exhibiting steady surface flow. *Physical Review Letters*, 86(9):1757–1760.
- [88] Lagrée, P. Y., Staron, L., and Popinet, S. (2011). The granular column collapse as a continuum: Validity of a two-dimensional Navier–Stokes model with a $\mu(i)$ -rheology. *Journal of Fluid Mechanics*, 686:378–408.

-
- [89] Lee, C. H. and Huang, C. J. (2012). Kinetic-theory-based model of dense granular flows down inclined planes. *Physics of Fluids*, 24(5):073303.
- [90] Lemieux, P.-A. and Durian, D. J. (2000). From avalanches to fluid flow: A continuous picture of grain dynamics down a heap. *Physical Review Letters*, 85(20):4273.
- [91] Li, J., Hamamoto, Y., Liu, Y., and Zhang, X. (2014). Sloshing impact simulation with material point method and its experimental validations. *Computers & Fluids*, 103:86–99.
- [92] Li, S., Yao, Q., Chen, B., Zhang, X., and Ding, Y. L. (2007). Molecular dynamics simulation and continuum modelling of granular surface flow in rotating drums. *Chinese Science Bulletin*, 52(5):692–700.
- [93] Li, X., Xie, Y., and Gutierrez, M. (2018). A soft–rigid contact model of MPM for granular flow impact on retaining structures. *Computational Particle Mechanics*, 5(4):529–537.
- [94] Li, X., Yan, Q., Zhao, S., Luo, Y., Wu, Y., and Wang, D. (2020). Investigation of influence of baffles on landslide debris mobility by 3d material point method. *Landslides*.
- [95] Liu, C., Sun, Q., Jin, F., and Zhou, G. G. (2017a). A fully coupled hydro-mechanical material point method for saturated dense granular materials. *Powder Technology*, 314:110–120.
- [96] Liu, C., Sun, Q., and Yang, Y. (2017b). Multi-scale modelling of granular pile collapse by using material point method and discrete element method. *Procedia Engineering*, 175:29–35.
- [97] Liu, C., Sun, Q., and Zhou, G. G. (2018). Coupling of material point method and discrete element method for granular flows impacting simulations. *International Journal for Numerical Methods in Engineering*, 115(2):172–188.
- [98] Liu, P., Yang, R., and Yu, A. (2013). DEM study of the transverse mixing of wet particles in rotating drums. *Chemical Engineering Science*, 86:99–107.
- [99] Llano-Serna, M. A., Farias, M. M., and Pedroso, D. M. (2015). An assessment of the material point method for modelling large scale run-out processes in landslides. *Landslides*, 13(5):1057–1066.
- [100] Lois, G., Lemaître, A., and Carlson, J. M. (2005). Numerical tests of constitutive laws for dense granular flows. *Physical Review E*, 72(5).
- [101] Louge, M., Valance, A., Taberlet, N., Richard, P., and Delannay, R. (2005). Volume fraction profile in channeled granular flows down an erodible incline. *Proc. Powders and Grains*.
- [102] Lucy, L. B. (1977). A numerical approach to the testing of the fission hypothesis. *The Astronomical Journal*, 82:1013.

-
- [103] Lun, C. K. K. (1991). Kinetic theory for granular flow of dense, slightly inelastic, slightly rough spheres. *Journal of Fluid Mechanics*, 233(-1):539.
- [104] M. Syamlal, W. Rogers, T. O. (1993). *Mfix documentation: Theory Guide*, National Technical Information Service. Springfield, USA.
- [105] Machado, M. V. C., Nascimento, S. M., Duarte, C. R., and Barrozo, M. A. S. (2017). Boundary conditions effects on the particle dynamic flow in a rotary drum with a single flight. *Powder Technology*, 311:341–349.
- [106] Maneval, J. E., Hill, K. M., Smith, B. E., Caprihan, A., and Fukushima, E. (2005). Effects of end wall friction in rotating cylinder granular flow experiments. *Granular Matter*, 7(4):199–202.
- [107] Mast, C. M., Arduino, P., Miller, G. R., and Mackenzie-Helnwein, P. (2014). Avalanche and landslide simulation using the material point method: flow dynamics and force interaction with structures. *Computational Geosciences*, 18(5):817–830.
- [108] McCarthy, J. J., Khakhar, D. V., and Ottino, J. M. (2000). Computational studies of granular mixing. *Powder Technology*, 109(1-3):72–82.
- [109] McCarthy, J. J., Shinbrot, T., Metcalfe, G., Wolf, J. E., and Ottino, J. M. (1996). Mixing of granular materials in slowly rotated containers. *AIChE Journal*, 42(12):3351–3363.
- [110] Meier, S. W., Lueptow, R. M., and Ottino, J. M. (2007). A dynamical systems approach to mixing and segregation of granular materials in tumblers. *Advances in Physics*, 56(5):757–827.
- [111] Mellmann, J. (2001). The transverse motion of solids in rotating cylinders—forms of motion and transition behavior. *Powder Technology*, 118(1):251–270.
- [112] Metcalfe, G., Graham, L., Zhou, J., and Liffman, K. (1999). Measurement of particle motions within tumbling granular flows. *Chaos: An Interdisciplinary Journal of Nonlinear Science*, 9(3):581–593.
- [113] Metcalfe, G., Shinbrot, T., McCarthy, J. J., and Ottino, J. M. (1995). Avalanche mixing of granular solids. *Nature*, 374(6517):39–41.
- [114] Minatti, L. and Paris, E. (2015). A sph model for the simulation of free surface granular flows in a dense regime. *Applied Mathematical Modelling*, 39(1):363–382.
- [115] Moukalled, F., Mangani, L., and Darwish, M. (2016). The finite volume method in computational fluid dynamics.
- [116] Navier, C. L. M. H. (1823). Mémoire sur les lois du mouvement des fluids. *Mémoires de l’Académie des sciences de l’Institut de France*, 6:389–416.
- [117] Nityanand, N., Manley, B., and Henein, H. (1986). An analysis of radial segregation for different sized spherical solids in rotary cylinders. *Metallurgical Transactions B*, 17(2):247–257.

-
- [118] OpenFOAM Foundation, editor (2012). *OpenFOAM 2.1.1 User Guide*.
- [119] Orpe, A. V. and Khakhar, D. V. (2007). Rheology of surface granular flows. *Journal of Fluid Mechanics*, 571:1.
- [120] Ottino, J. M. and Khakhar, D. V. (2000). Mixing and segregation of granular materials. *Annual Review of Fluid Mechanics*, 32(1):55–91.
- [121] Ottino, J. M. and Khakhar, D. V. (2002). Scaling of granular flow processes: From surface flows to design rules. *AIChE Journal*, 48(10):2157–2166.
- [122] Ottino, J. M. and Shinbrot, T. (1999). Comparing extremes: Mixing of fluids, mixing of solids. In *Mixing*, pages 163–186. Springer US.
- [123] Parker, D., Dijkstra, A., Martin, T., and Seville, J. (1997). Positron emission particle tracking studies of spherical particle motion in rotating drums. *Chemical Engineering Science*, 52(13):2011–2022.
- [124] Parker, D. J., Fan, X., Forster, R. N. G., Fowles, P., Ding, Y., and Seville, J. P. K. (2008). Positron imaging studies of rotating drums. *The Canadian Journal of Chemical Engineering*, 83(1):83–87.
- [125] Patankar, S. (1980). Numerical heat transfer and fluid flow. *Numerical Heat Transfer and Fluid Flow*.
- [126] Pereira, G. G., Sinnott, M. D., Cleary, P. W., Liffman, K., Metcalfe, G., and Šutalo, I. D. (2010). Insights from simulations into mechanisms for density segregation of granular mixtures in rotating cylinders. *Granular Matter*, 13(1):53–74.
- [127] Pignatelli, F., Asselin, C., Krieger, L., Christov, I. C., Ottino, J. M., and Lueptow, R. M. (2012). Parameters and scalings for dry and immersed granular flowing layers in rotating tumblers. *Physical review. E, Statistical, nonlinear, and soft matter physics*, 86:011304.
- [128] Pizette, P., Govender, N., Wilke, D. N., and Abriak, N. E. (2017). DEM GPU studies of industrial scale particle simulations for granular flow civil engineering applications. *EPJ Web of Conferences*, 140(3):03071.
- [129] Pohlman, N. A., Ottino, J. M., and Lueptow, R. M. (2006). End-wall effects in granular tumblers: From quasi-two-dimensional flow to three-dimensional flow. *Physical Review E*, 74(3).
- [130] Pollard, B. L. and Henein, H. (1989). Kinetics of radial segregation of different sized irregular particles in rotary cylinders. *Canadian Metallurgical Quarterly*, 28(1):29–40.
- [131] Pöschel, T. and Buchholtz, V. (1995). Complex flow of granular material in a rotating cylinder. *Chaos, Solitons & Fractals*, 5(10):1901–1912.
- [132] Pouliquen, O. (1999). Scaling laws in granular flows down rough inclined planes. *Physics of Fluids*, 11(3):542–548.

-
- [133] Pouliquen, O., Cassar, C., Jop, P., Forterre, Y., and Nicolas, M. (2006). Flow of dense granular material: towards simple constitutive laws. *Journal of Statistical Mechanics: Theory and Experiment*, 2006(07):P07020.
- [134] Pouliquen, O. and Forterre, Y. (2009). A non-local rheology for dense granular flows. *Philosophical Transactions of the Royal Society A: Mathematical, Physical and Engineering Sciences*, 367(1909):5091–5107.
- [135] Rapaport, D. C. (2002). Simulational studies of axial granular segregation in a rotating cylinder. *Physical Review E*, 65(6).
- [136] Renardy, M., Renardy, Y., and Li, J. (2001). Numerical simulation of moving contact line problems using a Volume-of-Fluid method. *Journal of Computational Physics*, 171(1):243–263.
- [137] Renouf, M., Bonamy, D., Dubois, F., and Alart, P. (2005). Numerical simulation of two-dimensional steady granular flows in rotating drum: On surface flow rheology. *Physics of Fluids*, 17(10):103303.
- [138] Ristow, G. H. and Nakagawa, M. (1999). Shape dynamics of interfacial front in rotating cylinders. *Physical Review E*, 59(2):2044–2048.
- [139] Rogers, A. and Clements, J. (1972). The examination of segregation of granular materials in a tumbling mixer. *Powder Technology*, 5(3):167–178.
- [140] Roux, J.-N. and Combe, G. (2002). Quasistatic rheology and the origins of strain. *Comptes Rendus Physique*, 3(2):131–140.
- [141] Sanfratello, L., Caprihan, A., and Fukushima, E. (2006). Velocity depth profile of granular matter in a horizontal rotating drum. *Granular Matter*, 9(1-2):1–6.
- [142] Santomaso, A., Olivi, M., and Canu, P. (2004). Mechanisms of mixing of granular materials in drum mixers under rolling regime. *Chemical Engineering Science*, 59(16):3269–3280.
- [143] Santomaso, A., Olivi, M., and Canu, P. (2005). Mixing kinetics of granular materials in drums operated in rolling and cataracting regime. *Powder Technology*, 152(1-3):41–51.
- [144] Santomaso, A. C., Artoni, R., and Canu, P. (2013). Controlling axial segregation in drum mixers through wall friction: Cellular automata simulations and experiments. *Chemical Engineering Science*, 90:151–160.
- [145] Santomaso, A. C., Petenò, L., and Canu, P. (2006). Radial segregation driven by axial convection. *Europhysics Letters (EPL)*, 75(4):576–582.
- [146] Santos, D. A., Petri, I. J., Duarte, C. R., and Barrozo, M. A. S. (2013). Experimental and CFD study of the hydrodynamic behavior in a rotating drum. *Powder Technology*, 250:52–62.
- [147] Savage, S. B. (1984). The mechanics of rapid granular flows. In *Advances in Applied Mechanics*, pages 289–366. Elsevier.

-
- [148] Savage, S. B. and Hutter, K. (1989). The motion of a finite mass of granular material down a rough incline. *Journal of Fluid Mechanics*, 199(-1):177.
- [149] Seiden, G. and Thomas, P. J. (2011). Complexity, segregation, and pattern formation in rotating-drum flows. *Reviews of Modern Physics*, 83(4):1323–1365.
- [150] Shi, B., Zhang, Y., and Zhang, W. (2017). Run-out of the 2015 shenzhen landslide using the material point method with the softening model. *Bulletin of Engineering Geology and the Environment*, 78(2):1225–1236.
- [151] Shoichi, S. (1998). Molecular-dynamics simulations of granular axial segregation in a rotating cylinder. *Modern Physics Letters B*, 12(04):115–122.
- [152] Silbert, L. E., Ertas, D., Grest, G. S., Halsey, T. C., Levine, D., and Plimpton, S. J. (2001). Granular flow down an inclined plane: Bagnold scaling and rheology. *Physical Review E*, 64(5).
- [153] Staron, L., Lagrée, P. Y., and Popinet, S. (2012). The granular silo as a continuum plastic flow: The hour-glass vs the clepsydra. *Physics of Fluids*, 24(10):103301.
- [154] Sulsky, D., Chen, Z., and Schreyer, H. (1994). A particle method for history-dependent materials. *Computer Methods in Applied Mechanics and Engineering*, 118(1-2):179–196.
- [155] Sulsky, D., Zhou, S.-J., and Schreyer, H. L. (1995). Application of a particle-in-cell method to solid mechanics. *Computer Physics Communications*, 87(1-2):236–252.
- [156] Sun, J. and Sundaresan, S. (2011). A constitutive model with microstructure evolution for flow of rate-independent granular materials. *Journal of Fluid Mechanics*, 682:590–616.
- [157] Taberlet, N., Losert, W., and Richard, P. (2004). Understanding the dynamics of segregation bands of simulated granular material in a rotating drum. *Europhysics Letters (EPL)*, 68(4):522–528.
- [158] Taberlet, N., Newey, M., Richard, P., and Losert, W. (2006). On axial segregation in a tumbler: an experimental and numerical study. *Journal of Statistical Mechanics: Theory and Experiment*, 2006(07):P07013–P07013.
- [159] Taberlet, N., Richard, P., Valance, A., Losert, W., Pasini, J. M., Jenkins, J. T., and Delannay, R. (2003). Superstable granular heap in a thin channel. *Physical Review Letters*, 91(26).
- [160] Volpato, S., Artoni, R., and Santomaso, A. C. (2014). Numerical study on the behavior of funnel flow silos with and without inserts through a continuum hydrodynamic approach. *Chemical Engineering Research and Design*, 92(2):256–263.
- [161] Volpato, S., Canu, P., and Santomaso, A. C. (2017). Simulation of free surface granular flows in tumblers. *Advanced Powder Technology*, 28(3):1028–1037.
- [162] Vun, S., Naser, J., and Witt, P. (2010). Extension of the kinetic theory of granular flow to include dense quasi-static stresses. *Powder Technology*, 204(6):11–20.

-
- [163] Wang, Z., Yang, J., Koo, B., and Stern, F. (2009). A coupled level set and volume-of-fluid method for sharp interface simulation of plunging breaking waves. *International Journal of Multiphase Flow*, 35(3):227–246.
- [164] Wightman, C. and Muzzio, F. J. (1998). Mixing of granular material in a drum mixer undergoing rotational and rocking motions II. segregating particles. *Powder Technology*, 98(2):125–134.
- [165] Xu, X., Jin, F., Sun, Q., Soga, K., and Zhou, G. G. (2019). Three-dimensional material point method modeling of runout behavior of the hongshiyuan landslide. *Canadian Geotechnical Journal*, 56(9):1318–1337.
- [166] Xu, Y., Xu, C., Zhou, Z., Du, J., and Hu, D. (2010). 2d DEM simulation of particle mixing in rotating drum: A parametric study. *Particuology*, 8(2):141–149.
- [167] Yamane, K. (2004). Discrete-element method application to mixing and segregation model in industrial blending system. *Journal of Materials Research*, 19(2):623–627.
- [168] Yamane, K., Nakagawa, M., Altobelli, S. A., Tanaka, T., and Tsuji, Y. (1998). Steady particulate flows in a horizontal rotating cylinder. *Physics of Fluids*, 10(6):1419–1427.
- [169] Zhang, Q. and Kamrin, K. (2017). Microscopic description of the granular fluidity field in nonlocal flow modeling. *Physical Review Letters*, 118(5).
- [170] Zheng, Q. J. and Yu, A. B. (2015). Modelling the granular flow in a rotating drum by the Eulerian finite element method. *Powder Technology*, 286:361–370.